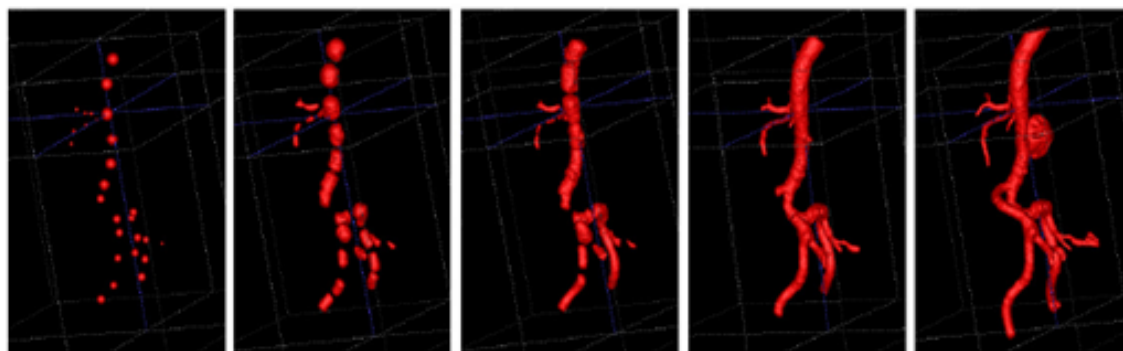
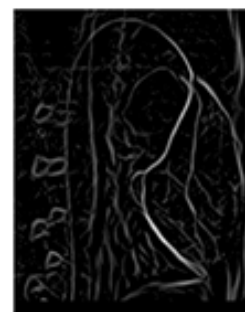
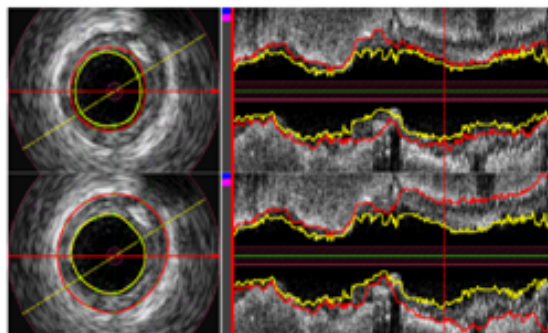
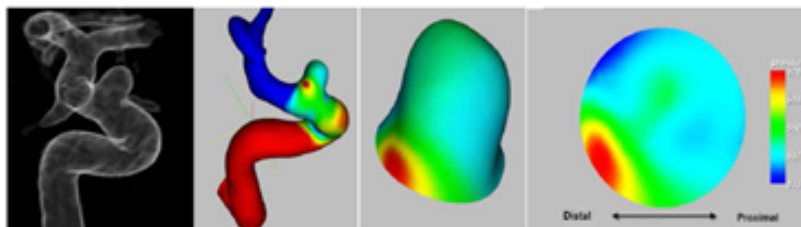
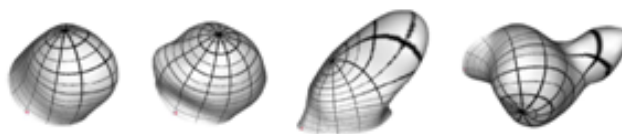
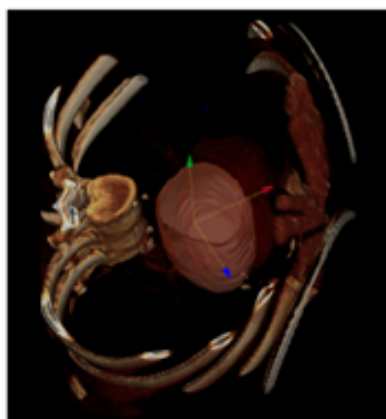


CVII '08

Computer Vision in Intracardiac
and Intravascular Imaging



Proceedings



The Second International Workshop on Computer Vision for Intravascular and Intracardiac Imaging (CVII) was held in New York, USA on September 10, 2008 and in conjunction with the 11th MICCAI Conference. This was the second workshop dedicated to the subject of intravascular and intracardiac imaging, and the workshop aimed to bring together researchers in the field and present state-of-the-art techniques in computer vision and image processing of intravascular and intracardiac images. Technological advances in intravascular and intracardiac imaging offer increasingly useful information regarding vascular anatomy and function and are poised to have dramatic impact on the diagnosis, analysis, modeling, and treatment of vascular diseases. Computer vision techniques designed to analyze intravascular images for anatomic modeling, simulation, visualization, tissue classification, and the assessment of interventional procedures are therefore playing a role of increased clinical importance.

There was much interest in the workshop, with 20 papers submitted. Based on the reviews of program committee members, 9 papers were accepted for oral presentation and 6 for short oral presentation. The papers cover many aspects of recent advances in intravascular and intracardiac imaging, including, but not limited to, segmentation, registration, plaque image analysis, tissue modeling, and classification. In addition to oral presentations, the workshop included two invited talks by speakers Dr. Johannes Rieber on trends and future applications of invasive and non-invasive coronary imaging, and Dr. Stephane Carlier on the evolution of intravascular imaging from ultrasound to optical coherence tomography. Dr. Robert Bard also presented the last results of a patient study on Elastographic Sonography of carotid artery plaque disease. We hope the oral and short oral sessions and invited talks will inspire new research in the field.

We thank our sponsors Siemens Corporate Research and Siemens AG for their support.

Gozde Unal, Ioannis A. Kakadiaris, Nassir Navab, Milan Sonka

Sponsored by
SIEMENS

Workshop Organizers

Gozde Unal, PhD, Sabanci University

Ioannis A. Kakadiaris, PhD, University of Houston

Nassir Navab, PhD, Technical University of Munich

Milan Sonka, PhD, University of Iowa

Invited Speakers

Stéphane Carlier, MD, PhD, Cordis, Johnson & Johnson, Belgium

Johannes Rieber, MD, Poliklinik Ludwig-Maximilian University, Siemens, Germany

Program Committee

Jolanda Wentzel, PhD, Erasmus MC, Netherlands

Andreas Wahle, PhD University of Iowa, USA

Guy Cloutier, PhD, University of Montreal, Canada

Petia Radeva, PhD, Universitat Autnoma de Barcelona, Spain

J.H.C. Reiber, PhD, Leiden University, Netherlands

Jouke Dijkstra, PhD, Leiden University, Netherlands

Aytul Ercil, PhD, Sabanci University, Turkey

Coordination Assistant

Olivier Pauly, PhD student, Technical University of Munich, Germany

Reviewing Committee

Roch Listz Maurice, PhD, University of Montreal , Canada

Christine Lorenz, PhD, Siemens Corporate Research , USA

Tom O'Donnell, PhD, Siemens Corporate Research, USA

Maximillian Baust, TUM, Germany

Ben Glocker, TUM, Germany

Christian Wachinger, TUM, Germany

Gerardo Mendizabal Ruiz, University of Houston, USA

Contents

- 1 Quantification of Vessel Wall Motion in IVUS Pull-backs With Dense Optical Flow, *M. G. Danilouchkine, F. Mastik, A. F. W. van der Steen* 6
- 2 Harmonic Mapping for Flattening of Aneurysm Surfaces, *Ashraf Mohamed, Liang-Der Jou, Chenyang Xu, Michel E. Mawad* 14
- 3 Efficient Semi-automatic Segmentation for Creating Patient Specific Models for Virtual Environments, *Y. Song, A. J. Bulpitt, K. Brodlie* 22
- 4 Automatic Stent Implant Follow-up in Intravascular Optical Coherence Tomography Images, *Serhan Gurmeric, Gozde Unal, Stéphane Carlier, Yan Yang, Greg Slabaugh* 35
- 5 Detection of Coronary Calcifications Using Supervised Hierarchical Classification, *U. Kurkure, D.R. Chittajallu, G. Brunner, R.P. Yalamanchili, I.A. Kakadiaris* 45
- 6 An Alternative Approach to Spectrum-Based Atherosclerotic Plaque Characterization Techniques Using Intravascular Ultrasound (IVUS) Backscattered Signals, *Amin Katouzian, Babak Baseri, Elisa E. Konofagou, Andrew F. Laine* 53
- 7 Growth Pattern of Atherosclerotic Calcifications, *Lene Lillemark Larsen, Melanie Ganz, Erik B. Dam, Naga P. K. R. Dandu, Mads Nielsen* 63
- 8 Segmentation of Intravascular Ultrasound Images using Graph Search and a Novel Cost Function, *Richard W. Downe, Andreas Wahle, Tomáš Kovárník, Hana Skalická, John J. Lopez, Jan Horák, Milan Sonka* 71
- 9 3-D Symbolic Reconstruction of Coronary Artery Tree from Multiple Views of Rotational X-Ray Angiography, *Rui Liao, Yiyong Sun, Luc Duong* 80
- 10 IVUS elastography of complex human coronary plaques treated by directional atherectomy: Technical issues and preliminary clinical results, *Jérémie Fromageau, Yoshifumi Saijo, Roch Listz Maurice, Marie-Hélène Roy Cardinal, Guy Cloutier* 88
- 11 Multiscale Optimization for the Fast-Marching Segmentation of Three-Dimensional Intravascular Ultrasound Images, *Marie-Hélène Roy Cardinal, Gilles Soulez, Jean-Claude Tardif, Jean Meunier, Guy Cloutier* 96
- 12 One-Class Acoustic Characterization Applied to Contrast Agent

- Detection in IVUS, *E. Gerardo Mendizabal-Ruiz, I.A. Kakadiaris* 104
- 13 A Heart-Centered Coordinate System for the Detection of Coronary Artery Zones in Non-Contrast Computed Tomography Data, *G. Brunner, D.R. Chittajallu, U. Kurkure, I.A. Kakadiaris* 112
- 14 Removal of bone information in dual energy CT, *Lei Zheng, Dmitry Maksimov, Tobias Stutzmann, Susanne Jochum, Carolin Brockmann, Steffen Diehl, Jürgen Hesser* 120
- 15 Improved Rigid Registration of Vessel Structures using the Fast Radial Symmetry Transform, *Carlo Gatta, Oriol Pujol, Oriol Rodriguez Leor, Josepa Mauri Ferre, Petia Radeva* 128

Quantification of Vessel Wall Motion in IVUS Pull-backs With Dense Optical Flow

M. G. Danilouchkine¹*, F. Mastik¹, and A. F. W. van der Steen^{1,2}

¹ Dept. Biomedical Engineering, Erasmus MC Rotterdam, the Netherlands

² Interuniversity Cardiology Institute of the Netherlands, Utrecht, the Netherlands
{m.danilouchkine,f.mastik,a.vandersteen}@ErasmusMC.nl

Abstract. In this paper we propose a novel method for the assessment of (apparent) vessel wall motion in intravascular ultrasound (IVUS) pullbacks. It is based on the Lukas-Kanade algorithm for optical flow (OF) and aligns consecutive frames in IVUS acquisitions. From the theoretical standpoint there are two fundamental improvements. Firstly, using a simplified representation of the vessel wall as a medium with randomly distributed scatterers, it was proven that the OF equation satisfies the integral brightness conversation constraint, alternatively known as dense OF. Secondly, a scale-space embedding for the OF equation was derived under the assumption of the spatial consistency in IVUS acquisitions. The spatial coherence is equivalent to a locally affine motion model. The hypothesis about the dense character of the flow was validated on the simulated IVUS images of thin-cap fibroatheroma (TCFA) subjected to varying pressurizing conditions and controlled amount of rotational deviation. The experimental results showed that proposed dense OF outperforms the classical LK method. The robust and reliable tracking was observed for angular deviations within the range between $1^\circ - 5^\circ$ of rotation. Subsequently, the algorithm was used to analyze 5 IVUS pullbacks from 4 patients. The results of the *in-vivo* experiments demonstrated that motion of the coronary arteries is primarily determined by the cardiac contraction.

1 Introduction

A number of imaging modalities are capable of assessing the vascular plaque burden. The most common modalities include Magnetic Resonance (MR) [1] and Computer Tomography (CT) [2] Angiography as well as Intravascular Ultrasound (IVUS) [3]. The primary challenge for all angiographic techniques is to suppress the motion-related artifacts in order to produce images of a good diagnostic quality. As results of the dedicated efforts along these directions [4, 5], CT and MR angiographic modalities are finding a wider clinical acceptance.

In spite of the non-invasive character of MR and CT, IVUS remains the gold standard in coronary imaging, owing to the inherently high spatial and temporal resolutions. The recently emerged IVUS-derived techniques, i.e. elastography [6, 7] and modulography [8], rely on the information, obtained from the same cross-section of the coronary artery at different levels of the intraluminal pressure. Subsequently, the information in two frames is compared to deduced the amount of vessel wall deformation and to compute its mechanical properties. Thus, the analyzed IVUS images should spatially match each other. However, the probe displacement causes interframe misalignment and

* This work is funded by the Dutch Foundation for Technical Sciences (STW) and Volcano Corporation (Rancho Cordova, CA, USA).

partially invalidates the information coming out of elastography and modu-
lography. Hence, further clinical acceptance of the aforementioned techniques
depends on their ability to cope with the motion-related artifacts.

This paper pursues two main goals. First, an automated registration method
is developed to align the consecutive frames in IVUS pullbacks. We are primar-
ily interested in rotational tissue motion, which can be used to spatially realign
the IVUS frame prior to elastographic computation. Second, this paper is also
an attempt to identify the major physiological factors, contributing to vessel
wall motion. The physiological background of in-plane vessel wall motion in
IVUS acquisitions has not been studied until now.

2 Methods

The aim of this section is to demonstrate that the amplitude of the reflected
ultrasonic signal is related to the density of the biological scatterers. A simple
geometric model of a healthy coronary artery was adopted for these purposes.
The vessel wall can be represented as an infinitely long cylindrical structure
with the inner and outer surfaces with the radii R_l and R_m , respectively. The
whole space between these two surfaces is filled with the randomly distributed
biological scatterers. An average radius of the scattering particle is \bar{a} . We are
interested in finding how much of the emitted intensity I_0 is being scattered in
a small volume V inside the vessel wall. The volume contains $\bar{n} \cdot V$ scattering
particles, where \bar{n} the average number of scattering particles per unit volume.
As the volume of interest is located with the vessel wall, it is reasonable to adopt
plane-wave incidence and far-field observation model. For weakly scattering in
continuous, isotropic, random medium, the intensity $\langle I \rangle$ of the acoustic wave
reflected from an agglomeration of scatterers at R with respect to the intensity
 I_0 of the emitted wave is given by the following expression [9]:

$$\frac{\langle I \rangle}{I_0} = \frac{k^4 \bar{a}^4 \bar{n} \gamma_0^2}{12\sqrt{2\pi} R^2} e^{-k^2 \bar{a}^2 / 2} \quad (1)$$

where k is the wavenumber; \bar{a} - the average size of the scatterer; γ_0^2 - mean-
square variation in acoustic impedance per scatterer.

In order to derive the variation in the intensity of the reflected echo waves,
it is worth considering the following physical argument. The coronary artery is
modeled as an infinitely long cylinder. Any cross-section of the cylinder, as a
result of the compression in the radial direction, wants to push outwards in the
longitudinal direction as a consequence of Poisson effect. However, the neigh-
boring cross sections in the longitudinal direction are the subject to exactly
same behavior. The cumulative results from the infinity of interactions is that
neither of the cross-sections actually squish. Thus, it is reasonable to assume
that the total number of scatters, contained in the imaged cross-section, re-
mains the same. However, the scatter density changes in response to the radial
deformation of the vessel wall:

$$\Delta n = \bar{n}^{pre} \frac{2 \cdot \Delta P (1 + \nu) (1 - 2\nu) R_l^2}{E (R_m^2 - R_l^2)} \quad (2)$$

where \bar{n}^{pre} - the scatterer density in the pre-compressed state; ΔP - the in-
traluminal pressure difference; E and ν are the Young's modulus and Poisson
ratio of the vessel wall.

Provided that the parameters of the imaging system as well as the physical
properties of the scatterers remain the same, the redistribution of scatterers

within the vessel wall (Eq. 2) is the primary cause for intensity variation (Eq. 1). This variation can alternatively be formulated via the conservational laws of continuum mechanics:

$$\frac{\partial}{\partial t} \int_{\Omega} \langle I \rangle(\mathbf{r}, t) d^2\mathbf{r} + \oint_{\partial\Omega} \langle I \rangle(\mathbf{r}, t) \mathbf{v} \cdot d\boldsymbol{\tau} = 0 \quad (3)$$

where Ω - imaged region of interest; $\boldsymbol{\tau}$ - differential normal element on $\partial\Omega$; \mathbf{v} - vector velocity field, characterizing the scatterer redistribution or motion. The temporal change in the backscattered intensity should match its flux through the vessel wall boundaries $\partial\Omega$. After applying the divergence theorem to the second integral and taking into account the fact that the conservation equation must hold for any arbitrary region within the vessel wall, one may obtain the following equation:

$$\frac{\partial \langle I \rangle(\mathbf{r}, t)}{\partial t} + \nabla \langle I \rangle(\mathbf{r}, t) \mathbf{v} + \langle I \rangle(\mathbf{r}, t) \nabla \cdot \mathbf{v} = 0 \quad (4)$$

The derived equation ties up the spatiotemporal changes in the average backscattered intensity with the vector velocity field and its divergence. The direct physical interpretation of Eq. 4 suggests that variation in the intensity may occur due to spatial displacement of the region and the possible changes in the scatterer density inside its boundaries. In the other words, the scattering particles are susceptible to the divergence of the vector velocity field. Eq. 4 is frequently referred to as the generalized motion constraint equation of dense optical flow (OF) [10], with \mathbf{v} denoting the optical flow vector field.

The OF equation uniquely defines a single component of the vector velocity field. To resolve this ambiguity, Lucas and Kanade [11] (LK) assumed a certain consistency in the local motion pattern and proposed to solve the OF equation as a least-square minimization problem:

$$\arg \min_{\mathbf{v}} \sum_{\mathbf{r} \in \Omega} w^2(\mathbf{r}, t) [\langle I \rangle_t(\mathbf{r}, t) + \nabla \langle I \rangle(\mathbf{r}, t) \mathbf{v} + \langle I \rangle(\mathbf{r}, t) \nabla \cdot \mathbf{v}]^2 \quad (5)$$

where $w(\mathbf{r}, t)$ is a binary weighting function, assigning value 1 to all pixel in the neighborhood, and 0 otherwise.

The evident advantage of the OF algorithm is that it can be readily adjusted to incorporate more complex motion model and to suppress the negative influence of a high noise level. Indeed, one of the error sources in speckle tracking with the OF algorithm is attributed to an inherently low signal-to-noise ratio, causing spurious responses of the employed differential operators. To amend the situation, a scale-space embedding of the OF equation was derived. It provides a well-founded framework for robust computation of the image derivatives via the convolution of the image with the precalculated multidimensional Gaussian derivatives. The OF vector field in Eq. 5 describes a pure translational motion of the small window. However, such a model is too restrictive to adequately represent complex deformation of the vessel wall. Instead, the affine motion model was considered. These two extensions yield the following minimization problem:

$$\arg \min_{\mathbf{v}} \sum_{\mathbf{r} \in \Omega} w^2(\mathbf{r}) [L_x(\mathbf{r})u - (\sigma^2 L_{xx}(\mathbf{r}) + L(\mathbf{r}))u_x - \sigma^2 L_{xy}(\mathbf{r})u_y + L_y(\mathbf{r})v - \sigma^2 L_{xy}(\mathbf{r})v_x - (\sigma^2 L_{yy}(\mathbf{r}) + L(\mathbf{r}))v_y + L_t(\mathbf{r})]^2 \quad (6)$$

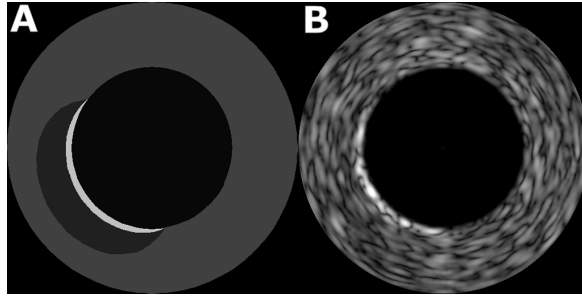


Fig. 1. The thin-cap fibroatheroma model (A) and a simulated ultrasound image (B), corresponding to the diseased cross-section.

where $L_{(\cdot)} = I * G_{(\cdot)}$ designates a convolution of the original image with a Gaussian kernel G or its spatial derivatives $G_x, G_y, G_{xx}, G_{xy}, G_{yy}$ with the variance parameter σ , while L_t designates the difference between the post- and pre-compressed frames for the convenience of the notations; $\mathbf{v} = (u, v, u_x, u_y, v_x, v_y)$ are the components of the OF vector velocity field up to the first order with (u, v) components describing the translation of the patch and (u_x, u_y, v_x, v_y) - its eventual deformation.

3 Experiments and Results

3.1 Simulation Experiments

As it is mentioned above the intensity variation in ultrasound images can be attributed to the redistribution of the scattering particles. The analytical expression for scatterer density changes (Eq. 2) was derived for a healthy cross-section of the coronary artery with the homogeneous structure. However, a moderately diseased artery has a fairly heterogeneous morphology. Unfortunately, there exists no analytical solution to compute the scatterer redistribution in diseased cross-sections of the coronary artery.

Nevertheless, the main principle of elastography [12] offers an intuitive explanation why the concept of dense OF is suitable to characterize vessel wall motion in general *in-vivo* applications. A higher rate of deformation for the compliant (softer, lipid) tissue due to variation in the intraluminal pressure is expected. Consequently, those regions of the atherosclerotic plaque would exhibit a higher rate of intensity divergence and the integral brightness constancy constraint holds. Contrarily, the stiffer (calcified) tissue would hardly change its shape upon application of a quasi-static compression load and, therefore, the classical pixel brightness constancy constraint is more appropriate. Thus, the dense OF concept is generic enough to handle the heterogeneous atherosclerotic plaques.

To validate this hypothesis we resorted to the numerical methods. A simple model of thin-cap fibroatheroma was utilized (Fig. 1A) for these purposes. The diseased cross-section was modeled as a cylindrical structure without compensational remodeling. The radii of the luminal (internal) and medial (external) vessel surfaces were equal to 1.4 mm and 2.5 mm, respectively. A plaque with the lipid-rich content spanned angle between 6 and 10 o'clock as shown in Fig. 1A. It was shielded from the luminal cavity by a thin fibrous cap with the approximate thickness $70 \mu\text{m}$. Recent pathological findings have shown that

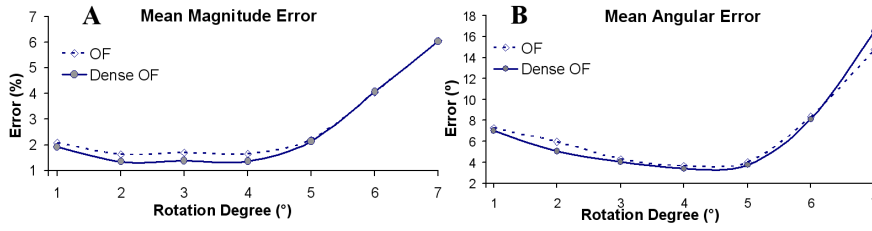


Fig. 2. A comparative plots between the classical Lucas-Kanade and proposed dense OF for the mean magnitude (%) and angular (°) errors in speckle tracking for different degrees of vessel wall rotation (horizontal axis).

this type of the atherosclerotic plaques is most vulnerable and a precursor for the acute cardiac events in 60-75% of the cases [13].

The COMSOL Multiphysics finite element package (Burlington, MA, USA) was utilized to compute the vessel wall deformation. The cross-sectional constitutive behavior was modeled as linear elastic, isotropic, nearly incompressible, plane-stress material. The assigned Young's modulus values were equal to 16.8 kPa, 4.2 kPa and 4 MPa for the wall region, lipid pool area and fibrous cap, respectively [14]. The pressure differential of 130Pa, which is typically observed in the IVUS acquisitions with 30 frames per second acquisition rate, was exerted in the luminal surface in the radial direction. To assure a unique finite element solution the modeled cross-section was embedded into a soft cylinder (Young's modulus 0.01 Pa) with the internal and external radii of 2.5 mm and 3 mm, respectively. The outer boundary was fixed.

The IVUS images of the vascular cross-section were created using FIELD II [15] package for simulation of the linear acoustic fields. The scatterers of equal echogenicity were randomly positioned within the vessel. The density of scattering particle depended on the region and amounted to 8000, 800 and 100 particles/mm³ for the fibrous cap, vessel wall and lipid, respectively. The synthetic phased array with the imaging parameters of an industrially produced IVUS catheter operated at the center frequency 20MHz with the sampling frequency of 100 MHz [?]. The 64 transducer elements were evenly spaced (0.56λ kerf) along the circumferential length of the probe (3F diameter). The IVUS image was reconstructed along 256 evenly distributed beams. For each beam the active aperture consisted of the nearest transducer element as well as 7 transducers located in the clockwise and counter-clockwise directions. Dynamic focusing and Hanning apodization were applied to the active aperture during transmission and reception. The simulated radio-frequency tracers were further converted into the B-mode images in the Cartesian coordinate system (5 mm x 5 mm; 512² matrix).

In order to estimate accuracy of speckle tracking with dense OF two types of images were utilized. A reference IVUS image was simulated in the pre-compressed state of the vessel wall, while all moved images - in the post-compressed state. The scatterers were displaced from their reference positions in a realistic manner representative for vessel wall deformation, computed with the COMSOL software package. Additionally the scatterers were rotated around the catheter center. The degree of angular deviation ranged from 1° to 7° with a 1° increment. The discrepancy between the reference and moved images was eliminated with the classical LK and proposed dense OF algorithm.

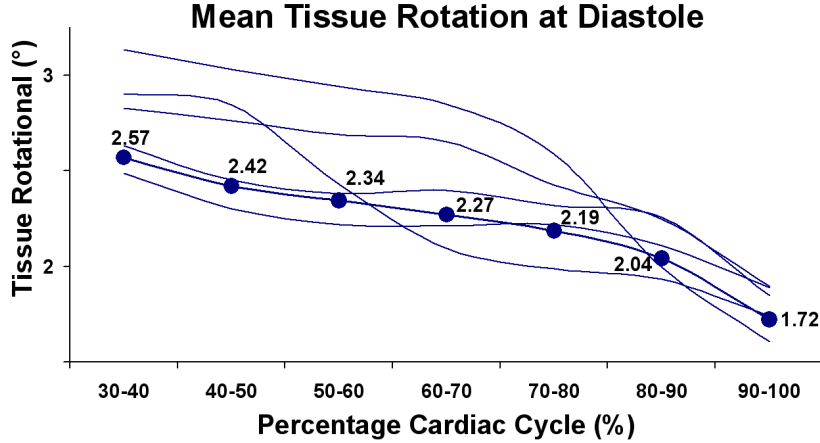


Fig. 3. The estimated amount of tissue rotation, predicted with the proposed OF algorithm at the diastole. The thick line represents the mean tissue rotation, averaged over 5 pullbacks.

Two different error measures, namely the absolute angular and relative magnitude errors [16], have been employed for the validation purposes. The first error is given by $\text{abs}(\arccos(\mathbf{d}_t, \mathbf{d}_e))$, where \mathbf{d}_t and \mathbf{d}_e are the true and estimated tissue displacements. It reflects the orientational discrepancy between the OF and true vector fields. The second error equals to $|\mathbf{d}_t - \mathbf{d}_e|/|\mathbf{d}_e| * 100\%$ and represents displacement magnitude deviation. All quantitative results are summarized in terms of the mean error values, averaged over the vessel wall and shown in Fig. 2.

3.2 *In-vivo* Experiments

The data set for the *in-vivo* experiments comprises of five pullback acquisitions from 4 patients. Each pullback contained approximately 3500 frames and corresponded to a coronary length of roughly 58 mm. The ECG signal was simultaneously recorded during IVUS acquisition. The number of images per cycle varied between 25 and 30.

The acquired images were processed off-line. After automatic delineation of the vessel boundaries, the computation of the OF field was performed over the detected region. The OF displacement vectors were converted into the rotational angles for each pixel of the vessel wall. Subsequently, the mean angular deviation of the tissue was computed by averaging the estimated rotational angles over the vessel wall.

To identify the contribution of the physiological factors to coronary artery motion, the images were synchronized with the ECG recordings. The pullback acquisition was regrouped into smaller parts, with each part representing only a one cardiac phase. Consequently, each cardiac cycle was divided into 10 equitemporal fractions. The IVUS images were temporally sorted in accordance with the phase of the cardiac cycle. In our experiment we considered only the temporal fractions between the begin (30%) and end (100%) diastole in accordance with the clinical protocol used in our establishment for the elastographic

analysis of the coronary arteries. For each diastolic fraction the average angle of tissue rotation was computed. The obtained values were averaged over the entire pullbacks. The results of the *in-vivo* experiments are summarized in Fig. 3, showing the plots of mean rotational tissue deviation during diastole for all 5 pullbacks.

4 Discussion and Conclusions

This paper presents a novel scale-space dense OF algorithm for accurate quantification of the tissue displacement induced by IVUS probe motion.

Using a simplified model of the coronary artery with the homogeneous morphological structure a close-formed solution for intensity variation in IVUS images was derived. This variation was attributed to the redistribution of the biological scatterers due to deformation of the vessel wall. However, the theoretical solution has a limited practical value, as it is only suitable for motion tracking in the healthy cross-sections of an IVUS pullback. A mildly diseased part of the coronary artery usually has a more complex heterogeneous morphology.

Nonetheless, it was demonstrated that the concept of dense OF [10] provides a suitable alternative for motion description in IVUS images of a deformed coronary artery. Consequently, the flux of the biological scatterers through the boundaries of the imaged region results in the amplitude variation of the backscattered echo signals. This variation is highly dependent on the local material properties of the vessel wall. As the soft lipid-rich regions undergo larger deformation, the flux of scatterers and, thus, intensity variation are expected to be larger. However, for the stiff calcified formation the flux of scatterers is negligible and the classical intensity conservation constraint is applicable. The aforementioned flux is nullified, when the difference in the intraluminal pressure drops to zero (Eq. 2). In this case, OF equation reduces to the classical LK formulation. Hence, dense OF properly models the intensity variation in IVUS images.

The last hypothesis was also validated on the simulated IVUS images of a diseased cross-section with a TCFA. The analysis of the mean errors (Fig. 2) favorably agrees with the previous findings about the accuracy of tracking in the tissue-mimicking phantoms [17]. The range of accurate prediction of tissue rotation is limited to 5° . Within this capture range, we observed that the proposed method noticeably outperforms the LK algorithm in terms of the average magnitude error, and is slightly better than the classical approach in terms of the mean angular error.

The *in-vivo* experiments clearly emphasize the complexity of tissue motion during diastole. A similar general trend in the average rotational tissue was observed for all five pullbacks (Fig. 3). The amount of angular deviation in coronary arteries amounted to 1.7° at end diastole and showed a definite graduate rise to 2.6° at early diastole. Coronary vessel motion generally agrees with the pattern of cardiac contraction. During the beginning of the diastole, the heart undergoes the stage of rapid filling, while it exhibits static behavior during end-diastole. The rate of rising varied from one patient to another, suggesting a certain influence of the patient respiration on motion of the vascular structures. However, we can conclude that the cardiac contraction dominates the respiratory motion. The similar results were observed by Shechter and *et.al.* [18], who studied the influence of the physiological factors on the 3D displacement of the coronary vessel tree with MRI.

References

1. Hofman, J.M., Branderhorst, W.J., ten Eikelder, H.M., Cappendijk, V.C., Heeneman, S., Kooi, M.E., Hilbers, P.A., ter Haar Romeny, B.M.: Quantification of atherosclerotic plaque components using in vivo mri and supervised classifiers. *Magnetic Resonance in Medicine* **55** (2006) 790–799
2. Schoenhagen, P., Halliburton, S.S., Stillman, A.E., Kuzmiak, S.A., Nissen, S.E., Tuzcu, E.M., White, R.D.: Noninvasive imaging of coronary arteries: current and future role of multi-detector row ct. *Radiology* **232** (2004) 7–17
3. Nissen, S.E., Tuzcu, E.M., Schoenhagen, P., Brown, B.G., Ganz, P., Vogel, R.A., Crowe, T., Howard, G., Cooper, C.J., Brodie, B., Grines, C.L., DeMaria, A.N.: Effect of intensive compared with moderate lipid-lowering therapy on progression of coronary atherosclerosis: a randomized controlled trial. *The Journal of the American Medical Association* **291** (2004) 1071–80
4. Saranathan, M., Ho, V.B., Hood, M.N., Foo, T.K., Hardy, C.J.: Adaptive vessel tracking: automated computation of vessel trajectories for improved efficiency in 2d coronary mr angiography. *Journal of Magnetic Resonance Imaging* **14** (2001) 368–373
5. Dewey, M., Laule, M., Krug, L., Schnapauff, D., Rogalla, P., Rutsch, W., Hamm, B., Lembcke, A.: Multisegment and halfscan reconstruction of 16-slice computed tomography for detection of coronary artery stenoses. *Investigative Radiology* **39** (2004) 223–229
6. de Korte, C., Cespedes, E., van der Steen, A., Lencee, C.: Intravascular elasticity imaging using ultrasound: Feasibility studies in phantoms. *Ultrasound in Medicine and Biology* **23** (1997) 735–746
7. Maurice, R.L., Ohayon, J., Finet, G., Cloutier, G.: Adapting the lagrangian speckle model estimator for endovascular elastography: Theory and validation with simulated radio-frequency data. *Journal of the Acoustical Society of America* **116** (2004) 1276–1286
8. Baldewsing, R.A., Schaar, J.A., Mastik, F., Oomens, C.W., van der Steen, A.F.W.: Assessment of vulnerable plaque composition by matching the deformation of a parametric plaque model to measured plaque deformation. *IEEE Transactions on Medical Imaging* **24** (2005) 514–528
9. Morse, P.M., Ingard, K.U.: *Theoretical Acoustics*. Princeton University Press (1987)
10. Florack, L.: *Image Structure*. Kluwer (1997)
11. Lucas, B., Kanade, T.: An iterative image registration technique with an application to stereo vision. In: *DARPA Image Understanding Workshop*. (1981)
12. Ophir, J., Cespedes, E., Ponnekanti, H., Yazdi, Y., Li, X.: Elastography: A quantitative method for imaging the elasticity in biological tissues. *Ultrasonic Imaging* **13** (1991) 111–134
13. Virmani, R., Burke, A.P., Kolodgie, F.D., Farb, A.: Pathology of the thin-cap fibroatheroma: a type of vulnerable plaque. *Journal of Interventional Cardiology* **16** (2003) 267–72
14. Baldewsing, R.A., de Korte, C., Schaar, J.A., Mastik, F., van der Steen, A.F.W.: A finite element model for performing intravascular ultrasound elastography of human atherosclerotic coronary arteries. *Ultrasound in Medicine and Biology* **30** (2004) 803–813
15. Jensen, J.A., Svendsen, N.B.: Calculation of pressure fields from arbitrarily shaped, apodized, and excited ultrasound transducers. *IEEE Transactions on Ultrasonics Ferroelectrics and Frequency Control* **39** (1992) 262–267
16. Barron, J.L., Fleet, D.J., Beauchemin, S.S.: Performance of optical-flow techniques. *International Journal of Computer Vision* **12** (1994) 43–77
17. Danilouchkine, M.G., Mastik, F., van der Steen, A.F.W.: Accuracy in prediction of catheter rotation in ivus with feature-based optical flow - a phantom study. *IEEE Transactions on Information Technology in Biomedicine* **12** (2008) 356–365
18. Shechter, G., Resar, J.R., McVeigh, E.R.: Displacement and velocity of the coronary arteries: cardiac and respiratory motion. *IEEE Transactions on Medical Imaging* **25** (2006) 369–375

Harmonic Mapping for Flattening of Aneurysm Surfaces

Ashraf Mohamed^{1,2}, Liang-Der Jou², Chenyang Xu¹, and Michel E Mawad²

¹ Siemens Corporate Research, Inc.
Princeton, NJ, U.S.A

² Baylor College of Medicine
Houston, TX, U.S.A

ashraf.mohamed@siemens.com

Abstract. We describe an approach for harmonic surface mapping of blood vessel aneurysms into a topologically equivalent canonical space. We use this approach to map and visualize local hemodynamic variables associated with the surface of sidewall internal carotid artery aneurysms (ICA) imaged by 3D X-ray angiography. These variables are derived from steady-state computational fluid dynamic simulations. An invertible harmonic map of the aneurysm surface onto the unit disc allows visual inspection of the entire surface and associated quantities at once, unobscured by shape irregularities. Results indicate that the developed approach is close to being conformal, thereby preserving local shape. This approach has applications in the generation of statistical atlases of aneurysms and in quantitative group studies of aneurysm development, growth, rupture, and treatment.

1 Introduction

An aneurysm is a localized disease of the wall of an artery, leading to its bulging or dilatation. Aneurysms may occur at any location in the body, but are most commonly associated with the aorta or blood vessels feeding the brain. Intracranial aneurysms bear the medical risk of vessel rupture leading to intracranial bleeding, which may cause irreparable neurological damage or fatality [1]. Two approaches exist for the treatment of brain aneurysms. The endovascular approach is performed under fluoroscopic guidance and it involves the insertion of wire coils or glue inside the aneurysm with the intention of forming a blood clot that stops the blood flow into it. The second approach involves neurosurgical clipping of the aneurysm at its neck.

While some aneurysms rupture quickly after their formation, others may remain without complications for many years. The risk of aneurysm rupture is estimated to be between 0.5% and 2.5% per year [2]. The risks and costs associated with aneurysm treatment, combined with the uncertainty of rupture has created a large body of research efforts aiming to differentiate aneurysms that carry a high risk of rupture from those with a low risk. Studies have revealed some overall shape characteristics that affect the risk of rupture, including aneurysm

size, shape, aspect ratio [3]. Other recent studies have implied a link between the overall distribution of hemodynamic variables such as wall shear stress (WSS) and the risk of rupture[4, 5]. However, since populations of ruptured and unruptured aneurysms overlap under many of the metrics designed to assess the risk of rupture, it is still not possible to estimate the risk of rupture of some aneurysms with reasonable certainty. Large longitudinal and cross-sectional group studies that could reveal possible links between the risk of rupture and the distribution of local variables, such as WSS, are currently not possible due to the absence of an approach for establishing correspondence across aneurysms in different patients and in the same patient at different points in time. The availability of such a technique will enable the use of analysis methods that could unravel important local factors affecting aneurysm rupture.

We describe an approach for generating bijective smooth maps of aneurysm surfaces onto a common topologically equivalent canonical space. By solving a pair of linearized harmonic equations via the finite element method, these invertible maps are generated in a consistent manner across aneurysms. This approach makes many useful analysis methodologies applicable to the study of aneurysms, their formation, growth, and the risk of rupture. The theory behind the mapping approach is explained in Section 2. In Section 3, the use of this approach is demonstrated for the mapping of sidewall intracranial aneurysms of the internal carotid artery (ICA) imaged by three-dimensional (3D) X-ray angiography. The resulting mapping onto the unit disc makes it possible to visualize and inspect the whole aneurysm surface and associated Computational Fluid Dynamics (CFD)-derived WSS at once, unobscured by surface irregularities. We show that in reality, the resulting map is close to being conformal, thereby preserving the local shape of the aneurysm surface during mapping. The presented preliminary results also visually suggest the existence of differences in the configuration of an area distortion measure between ruptured and unruptured aneurysms. In Section 4, we discuss directions for future work.

2 Methods

2.1 Harmonic Mapping to the Unit Disc

In Fig.1, an illustration of the developed approach for aneurysm surface mapping is provided. Assume that a representation of the aneurysm surface and the blood vessels to which it is attached is available. This surface representation may, for example, be obtained through segmentation of the vasculature from a 3D angiographic medical image (e.g., X-ray or magnetic resonance angiography) followed by isosurface extraction to produce a triangular surface mesh. Assume that the surface of the aneurysm has been separated from the parent artery after identification of the neck and performing mesh partitioning via a proper method. Sidewall aneurysms originate from a diseased focal spot of the artery wall and their surface may therefore be assumed topologically equivalent to the unit disc. Therefore, the unit disc may be chosen as a canonical space for this class of aneurysms.

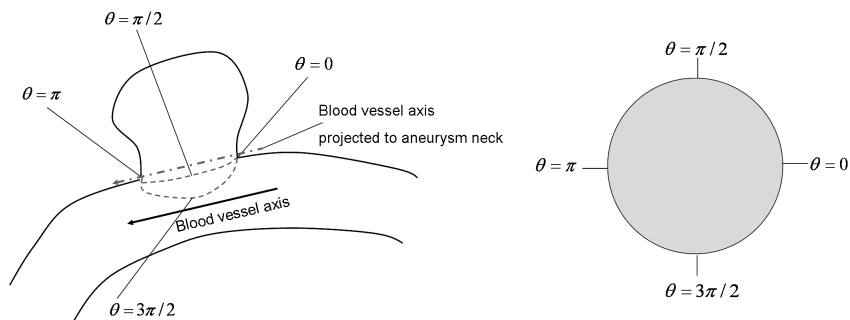


Fig. 1. Illustration of the mapping of sidewall ICA aneurysms to the unit disc. The aneurysm neck is a closed topological circle and the most proximal neck point may be found from the parent vessel's orientation. Mesh partitioning separates the aneurysm from its parent vessel at the neck. The function ϕ maps the aneurysm surface onto the unit disc such that the most proximal point goes to $\theta = 0$.

Let $\mathcal{S} \in \mathbb{R}^3$ denote the surface of the aneurysm and assume that \mathcal{S} is a smooth genus 0 (with no holes or handles) orientable surface. Since \mathcal{S} is topologically equivalent to the unit disc $\mathbb{D} = \{(u, v) : u^2 + v^2 \leq 1\}$, its boundary \mathcal{B} with total length L is a topological circle. The goal of the surface mapping problem is to find a smooth and bijective (therefore invertible) function $\varphi : \mathcal{S} \rightarrow \mathbb{D}$ such that \mathcal{B} is mapped to the unit circle. To specify the problem further, assume that point $\mathbf{A} \in \mathcal{B}$ must be mapped to the point $(1, 0)$ and define $l_{\mathbf{p}}$ as the distance along \mathcal{B} from \mathbf{A} to any point $\mathbf{p} \in \mathcal{B}$ traveling in the counterclockwise direction while observing the outside surface of \mathcal{S} . We choose point \mathbf{A} to be the most proximal point on the aneurysm neck. Defining Δ as the Laplace-Beltrami operator on \mathcal{S} , a harmonic mapping $\varphi = (u, v)$ is found by solving the Dirichlet problem [6, 7]:

$$\left. \begin{aligned} \Delta u(\mathbf{p}) &= 0 \\ \Delta v(\mathbf{p}) &= 0 \end{aligned} \right\} \mathbf{p} \in \mathcal{S} \setminus \mathcal{B} \quad (1)$$

$$\left. \begin{aligned} u(\mathbf{p}) &= \cos(2\pi l_{\mathbf{p}}/L) \\ v(\mathbf{p}) &= \sin(2\pi l_{\mathbf{p}}/L) \end{aligned} \right\} \mathbf{p} \in \mathcal{B} \quad (2)$$

The harmonic mapping φ is the minimizer of the Dirichlet functional [8]:

$$\mathcal{D}(\varphi) \equiv \frac{1}{2} \int_{\mathcal{S}} (\|\nabla u\|^2 + \|\nabla v\|^2) d\mathcal{S} \quad (3)$$

subject to the boundary conditions (2). Equation (3) implies that φ minimizes the deformation induced by the mapping.

2.2 Finite Element Formulation

To obtain a discrete harmonic map φ_T over the triangular surface mesh \mathcal{S}_T which is a discretization of \mathcal{S} , we use linear finite element theory [8, 6]. Let \mathcal{B}_T

be the boundary of \mathcal{S}_T . The minimization of the functional (3) over the set of all piecewise linear functions on \mathcal{S}_T is achieved by the transformed mesh node coordinates $(U_Y, V_Y), Y \in \mathcal{S}_T \setminus \mathcal{B}_T$ satisfying the linear equations:

$$\sum_{Y \in \mathcal{S}_T \setminus \mathcal{B}_T} D_{XY} U_Y = - \sum_{Y \in \mathcal{B}_T} D_{XY} \cos(2\pi l_Y / L) \quad (4)$$

$$\sum_{Y \in \mathcal{S}_T \setminus \mathcal{B}_T} D_{XY} V_Y = - \sum_{Y \in \mathcal{B}_T} D_{XY} \sin(2\pi l_Y / L) \quad (5)$$

which can be written in matrix form as:

$$\mathbf{D}\mathbf{u} = \mathbf{b}_u \text{ and } \mathbf{D}\mathbf{v} = \mathbf{b}_v \quad (6)$$

The elements D_{XY} are easily computed from the geometry of \mathcal{S}_T as follows [6]. For each edge XY belonging to two triangles XYJ and XYK , we have

$$D_{XY} = -0.5(\cot(\angle J) + \cot(\angle K)) \quad (7)$$

where $\angle J$ is the angle at the vertex J in the triangle XYJ and $\angle K$ is the angle at vertex K in the triangle XYK . If mesh nodes X and Y are not connected by an edge then $D_{XY} = 0$. The diagonal entries of \mathbf{D} are computed as :

$$D_{XX} = - \sum_{Y \neq X} D_{XY} \quad (8)$$

Since the matrix \mathbf{D} is positive definite, symmetric and sparse [8,7], we use the conjugate gradient method to compute the solutions \mathbf{u} and \mathbf{v} . Since φ_T is harmonic and maps the boundary \mathcal{B}_T homeomorphically into a convex region $\mathbb{D} \in \mathbb{R}^2$, therefore, φ is bijective [8]. We note that a harmonic map need not be conformal (preserve local angles) in general. However, the results provided below, indicate that the deviation of this harmonic map from conformality is small

3 Experiments and Results

We illustrate the utility of the mapping approach described above in the surface flattening and visualization of CFD simulation results for sidewall ICA aneurysms. The triangular surface meshes used for CFD simulations and for flattening are based on 3D digital subtraction angiography (DSA) images (*syngo* Inspace 3D, Siemens Healthcare, Forchheim, Germany) with a typical size of 512x512x400 and isotropic voxel size of 0.4mm. A subvolume region of interest for CFD simulations is defined manually to include the aneurysm and the parent vessel. The used image segmentation approach involves smoothing, thresholding, connected component labeling, and hole filling in order to generate a segmented object with a genus 0 surface. Steady-state (diastole) CFD simulations are carried out and the resulting surface attached WSS is extracted. Details of the

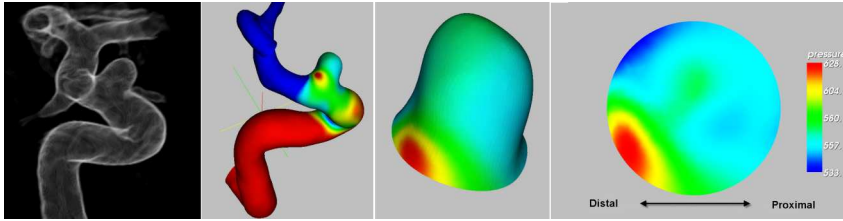


Fig. 2. Mapping an unruptured sidewall ICA aneurysm to the unit disc. Left to right: volume rendered 3D DSA image of the artery and aneurysm; surface rendered image after CFD simulation showing wall pressure values; aneurysm surface with attached wall pressure after neck identification and mesh partitioning; wall pressure values mapped to the unit disc.

surface mesh generation approach and CFD simulations methods can be found in [4, 5]. Mesh partitioning via a clip plane is used in order to separate the aneurysm from the parent vessel. Point **A**, which is the most proximal point on the aneurysm neck, is determined manually.

We evaluate the angle and area distortion introduced by the devised mapping via the following measures. Let A_a be the total original aneurysm mesh surface area and XYZ be a triangle in this mesh with area A_{XYZ} before mapping and area \tilde{A}_{XYZ} after mapping. With the area of the unit disc equal to π , the area distortion of XYZ may be defined as

$$d_{XYZ} \equiv \frac{\tilde{A}_{XYZ}}{A_{XYZ}} \cdot \frac{A_a}{\pi} \quad (9)$$

At each mesh vertex X connected to M triangles in the original mesh, let $a_{Xi}, i = 1, \dots, M$ denote the ratio of the angle i to the sum of all angles around X . Let the similar ratio for the mapped mesh be denoted by $\tilde{a}_{Xi}, i = 1, \dots, M$. The angle distortion error $|\tilde{a}_{Xi} - a_{Xi}|/a_{Xi}$ is averaged over all triangles attached to X to produce a single value at X , and then the overall average for the whole mesh is computed. Angle distortion errors computed over 15 aneurysms were 6.1% on average with a maximum of 10.6% and minimum of 2.8%. These results indicate that the devised mapping is at least close to being quasi-conformal. The FE implementation of the mapping typically takes one second or less on a modern day computer (2.13 GHz Intel Pentium M, 2.0GB of RAM). The number of nodes of the aneurysm surface meshes was 11192 on average.

In Fig.2, we demonstrate the approach via an example unruptured ICA aneurysm. The mapping allows the visualization of the whole aneurysm surface at once, thereby easily understanding the spatial variation of quantities, such wall pressure. For dynamic CFD studies, our results indicate that it is substantially more easy to visually observe pattern changes over the whole surface across time in a cine-type image over the unit disc.

In Fig. 3, we compare WSS patterns from two unruptured and two ruptured aneurysms. These patterns agree with the conclusions drawn in [5]. Despite the

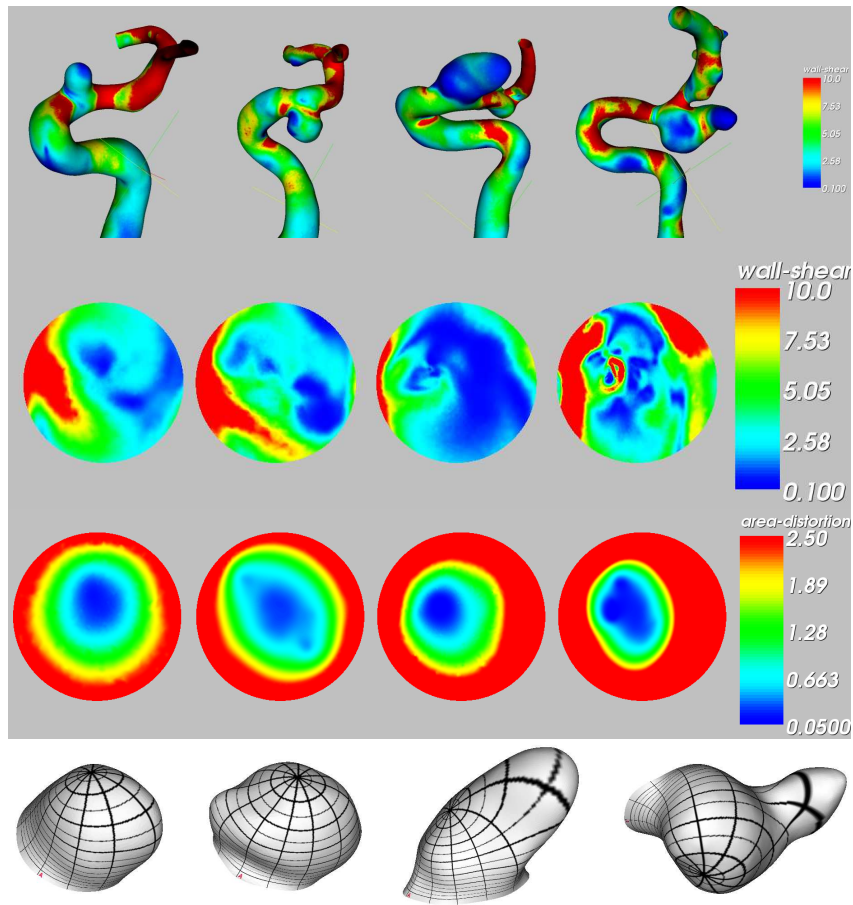


Fig. 3. Mapping of two unruptured (left) and two ruptured (right) ICA aneurysms to the unit disc. Top to bottom: WSS values for the ICA with attached aneurysms; mapping of WSS onto the unit disc; area distortion for the mappings; parameterization of the aneurysm surfaces via radial lines and circles of increasing diameters in the unit disc.

absence of differences in the range of WSS between ruptured and unruptured aneurysms, the distribution of the WSS seems to vary more rapidly over the unit disc for ruptured aneurysms. These rapid changes seem to be related to shape irregularities of ruptured aneurysms. From the flattened WSS maps, it is further easy to conclude that the low WSS region occurs at the proximal aneurysm wall, locates at the dome, or occupies most of the entire aneurysm; the high wall shear stress region often, but not always, occurs at the distal part of the surface. In the same figure, we show the area distortion due to the mapping. The results

based on these limited samples, as well as others not shown here, indicate that the distribution of the blue areas (d_{XYZ} close to 0, or relative compression due to mapping) is more eccentric and distal for ruptured ICA aneurysms than for unruptured ones. The same observation of significant distortion off the center of the disc is also evident through the parameterization of the aneurysm surface according to the computed mapping.

4 Disucssion and Future Work

We presented an approach for generating smooth, invertible harmonic maps of aneurysm surfaces onto a standardized canonical space. In the experiments presented above, we demonstrated the utility of the generated maps in the flattening of saccular intracranial aneurysm surfaces to the unit disc, the unobscured visualization of CFD-derived variables such as wall pressure and WSS, and the visualization of area distortion maps. The choice of the canonical space for the mapping depends on the topology of the analyzed class of aneurysms. A fusiform aneurysm involving the whole circumference of the artery is topologically equivalent to a cylinder and therefore may be mapped to a sphere with two caps cut off, or to the unit square after one surface cut parallel to the cylinder’s axis [6].

Beside aneurysm surface flattening and visualization, the presented approach has many applications in the study of aneurysm formation, growth, and risk of rupture. By bijectively mapping different aneurysms in a consistent way, correspondence between points on the surfaces of these aneurysms may be established, and surface-attached variables are transformed into a space where statistical analysis can be performed. This allows the construction of statistical atlases that link these surface attached variables (e.g., local curvature and WSS) to clinical variables, such as the risk of rupture and treatment outcome. These statistical atlases, when mapped to new patients, provide a wealth of information that may help in clinical decision making [9]. Additionally, the inverse mapping from a canonical space to an aneurysm provides a parameterization of the aneurysm surface [8], thereby allowing the use of frequency and space-time analysis methods for the study of surface associated quantities affecting risk of rupture, such as local curvature [10]. Furthermore, the properties of the mapping itself, such as the transformation Jacobian, may act as a shape descriptor that will help understand anatomical shape variability and differences between groups of ruptured and unruptured aneurysms [11].

The presented approach relies on harmonic maps, which minimize shape distortion. For a non-closed surface, such as the surface of a saccular aneurysm separated from the parent artery, harmonic maps are not conformal (angle-preserving) in general [12]. However, the presented results indicate that the generated maps are close to being conformal and therefore, preserve the local shape. To guarantee the generation of a conformal map (or quasi-conformal for a discrete surface mesh), it is possible to use the approach described by Jin et al. [13] for changing a topological disc into a topological sphere. Further future work includes investigating robust approaches for the localization of the aneurysm

neck, approaches for automatically identifying the most proximal point of this neck, and investigating the sensitivity of the mapping to these approaches.

References

1. Weir, B.: Unruptured intracranial aneurysms: A review. *J. Neurosurg* **96** (2002) 3–42
2. Beck, J., Rohde, S., El-Beltagy, M., Zimmermann, M., Berkefeld, J., Seifert, Z., Raabe, A.: Difference in configuration of ruptured and unruptured intracranial aneurysms determined by biplanar digital subtraction angiography. *Acta Neurochir.* **145** (2003) 861–865
3. Raghavan, M.H., Ma, B., Harbaugh, R.E.: Quantified aneurysm shape and rupture risk. *J. Neurosurg.* **102** (2005) 355–362
4. Jou, L.D., Wong, G., Dispensa, B., Lawton, M.T., Higashida, R., Young, W.L., Saloner, D.: Correlation between luminal geometry and hemodynamics in fusiform intracranial aneurysms. *American Journal of Neuroradiology* **26** (Oct. 2005) 2357–2363
5. Jou, L.D., Lee, D.H., Morsi, H., Mawad, M.E.: Wall shear stress on ruptured and unruptured intracranial aneurysms at the internal carotid artery. *American Journal of Neuroradiology* (Oct. 2008)
6. Hacker, S., Angenent, S., Tannenbaum, A., Kikinis, R.: Nondistorting flattening maps and the 3-D visualization of colon ct images. *IEEE Transactions on Medical Imaging* **19**(7) (July 2000) 665–670
7. Hacker, S., Angenent, S., Tannenbaum, A., Kikinis, R., Sapiro, G., Halle, M.: Conformal surface parameterization for texture mapping. *IEEE Transactions on Visualization and Computer Graphics* **6**(2) (April-June 2000) 181–189
8. Floater, M.S., Hormann, K.: Surface Parameterization: a Tutorial and Survey. In: *Advances in Multiresolution for Geometric Modelling*. Springer-Verlag, Heidelberg (2005) 157–186
9. Davatzikos, C.: Spatial transformation and registration of brain images using elastically deformable models. *Comp. Vis. and Image Understanding, Special Issue on Medical Imaging* **66**(2) (May 1997) 207–222
10. Rohde, S., Lahmann, K., Beck, J., Nafe, R., Yan, B., Raabe, A., Berkefeld, J.: Fourier analysis of intracranial aneurysms: Towards objective and quantitative evaluation of the shape of aneurysms. *Neuroradiology* **47** (2005) 121–126
11. Woods, R.P.: Characterizing volume and surface deformations in an atlas framework: theory, applications, and implementation. *NeuroImage* **18** (2003) 769–788
12. Schoen, R.M., Yau, S.T.: *Lectures on Harmonic Maps*. Cambridge, MA: Harvard Univ., Int. Press (1997)
13. Jin, M., Wang, Y., Yau, S.T., Gu, X.: Optimal global conformal surface parameterization. In: *Proceedings of IEEE Visualization 2004, Austin, Texas, USA* (Oct. 10-15 2004) 267–274

Efficient Semi-automatic Segmentation for Creating Patient Specific Models for Virtual Environments

Y. Song, A. J. Bulpitt and K. Brodlie

School of Computing, University of Leeds, UK
{yisong, andyb, kwb}@comp.leeds.ac.uk

Abstract. There is an increasing demand for the development of virtual environments for training in vascular interventional radiological procedures. This requires fast and precise segmentation of varied abdominal structures from a wide range of image modalities. This paper presents an efficient semi-automatic segmentation system which combines image processing techniques and mathematical morphology operations to obtain an initial segmentation close to the target structure shape. This initial segmentation is then embedded into a level set function to obtain a refined segmentation result. Minimal intervention is required in comparison to other level set based approaches. The approach also dramatically decreases processing time and reduces the risks of leaking at weak boundaries, without compromising the accuracy of the segmentation.

1 Introduction

Our work is part of the CRaIVE¹ project to develop a physics based Virtual Environment (VE) for training in vascular interventional radiological procedures. It aims to provide an alternative to apprenticeship training using physical and animal models where not only are the traditional physical models expensive, but their fixed anatomy also constrains the training achievements where a wide range of pathology is required to be presented to trainees.

Creating virtual humans for this task requires major abdominal structures to be segmented with particular interest in those cases where typical symptoms are presented. Currently, our data are collected from various hospitals and research institutes in order to cover a large variety of cases. Consequently, the resource images to be segmented vary greatly in quality, size and resolution and the presented abdominal structures are typically significantly different from those found in healthy cases.

A myriad of different segmentation methods have been proposed and implemented in recent years. See [14][6][1] for recent reviews. Model-driven, knowledge based image analysis is one of the techniques often used; this aims to describe

¹ Collaborators in Radiological Interventional Virtual Environments, <http://www.craive.org.uk>

and capture a priori information regarding the shape, size and position of each structure. Normally deformable models[4], statistical shape models[5] and probabilistic atlases[9] are employed. The limitation of these approaches is the generation of a suitable template model which is able to capture both natural variations and deformations caused by pathology. As our system needs to handle various abnormalities, sometimes with extreme shape deformation, current model-driven approaches are not well suited to our application.

In addition, the varied image modalities further limit the applications of previous segmentation techniques. For example, approaches based on the region growing technique[11] or mathematical morphology operations[19] such as DTT (Differential tip-hats) and conditional dilation etc., can provide good results on contrast-enhanced images. However since these techniques are based on the image intensity similarity, when adjacent neighbouring tissues have similar intensity to the target structure, the region growing approach is easily over segmented, while mathematical morphology operations could fail to divide the adjoining tissues completely.

Approaches based on the level set method [13][2] have also been used successfully for medical image segmentation. However, the problem of "leaks" on the boundary is still open to research. Pan and Dawant[10] propose to progressively slow down the speed as the front passes over boundary points. They also added a priori anatomical information to the accumulative speed function. Other drawbacks include its sensitivity to positioning seeds in the volume data and the non-trivial work of setting parameters according to the image modalities and object structures[16]. Tools [7][18] have been developed to allow interactive editing of level set models.

In this paper, we are interested in developing a general solution to recovering abnormal structures in real time with minimal user interaction. In contrast to previous work focusing on either specified image type, (e.g. CT or MR image[14]) or specified structures (e.g. liver or vascular segmentation[6][1]), the proposed segmentation system must be able to cope with a wide variety of structure shapes and image modalities. As automatic segmentations relying on the statistics of image intensities, mean organ shape or position do not work effectively for our purpose, we develop an efficient semi-automatic segmentation system. Fig.1 shows the major components involved in our segmentation framework. Our approach combines image processing techniques and mathematical morphology operations to identify the tissue of interest and obtain an initial segmentation close to the target structure shape. The initial segmentation is then refined using a level set method, instead of growing a new segmentation from seed points as in previous approaches. For many cases, this framework requires little pre-processing on its input. Smoothing the input image is not usually required to produce reasonable solutions, though it may still be warranted in some cases.

Although this is a semi-automatic system, the required external interventions are limited to two interactive operations:

- * Definition of a range of intensity values that classify the tissue type of interest, which is an alternative to automatic estimation based on intensity distribution;
- * A seed point is placed in a desired region as an input to a simple region growing algorithm to provide the initialization for the level set approach. This can greatly reduce the labour requirement of manual seed placement used by other level set based approaches.

Unlike other level set based approaches, our system is not sensitive to the parameter settings. Default parameters are applied without the need to tune on a case by case basis. Furthermore, no information on general shape, location and orientation of an anatomical structure of interest is required in our system.

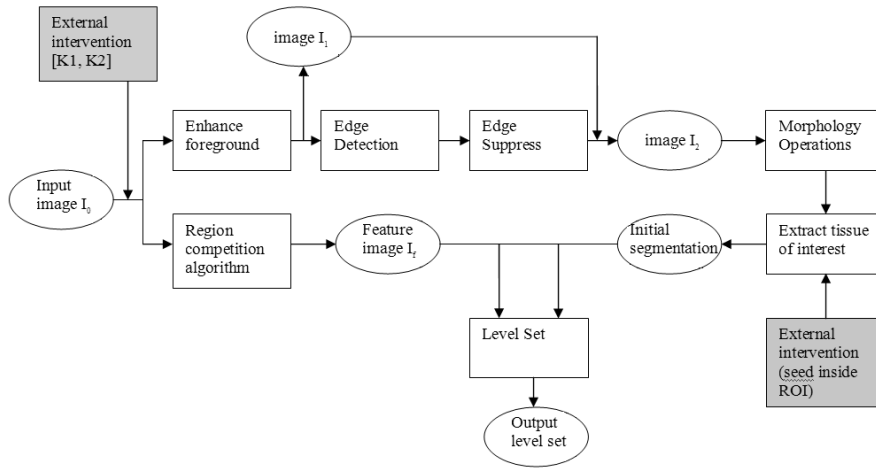


Fig. 1. Work flow

2 Methodology

A large body of work has explored the level set method and its applications in image segmentation [3][17]. Although the level-set technique is relatively insensitive to initial conditions, a reasonable prior segmentation as the initialization could 1) increase the chances of segmenting a complex object without missing parts and 2) help to reduce the amount of time needed by the front to propagate through a whole object and hence reduce the risk of leaks on the edges of regions visited earlier. Many approaches place seeds and implement a fast marching algorithm to grow the seeds as the initial segmentation which is the input of level set method applied afterward. The disadvantage is the initial segmentation

result is sensitive to the seed positions and seed numbers. For example, when segmenting an elongated object, it is undesirable to place a single seed at one extreme of the object since the front will need a long time to propagate to the other end of the object. Obviously placing several seeds along the axis of the object is probably the best strategy to ensure that the entire object is captured early in the expansion of the front. However, this normally requires users with sufficient anatomical knowledge and it is also a non trivial process.

To overcome those shortcomings, we propose an initialization method which employs edge enhancement following by mathematical morphology operations to ensure that the major object structures could be captured. This prior segmentation will then be embedded into the level set function for further refinement. As the level set then starts from a close approximation to the actual structure shape, this approach can improve the accuracy of results and dramatically decrease processing time. Consequently, the risk of leaks which is common to previous level set based approaches can be minimized.

In this section, our approach is demonstrated using an example of aorta segmentation. The abdominal CT data set was collected at an in-plane resolution of $0.84375mm$ by $0.84375mm$ with an inter-slice distance of $1mm$. The data dimensions are $512 \times 512 \times 401$. No contrast was infused. The images show slices through the point $(284, 271, 203)$.

2.1 Segmentation Initialization

Edge enhancement Generally speaking, the first step in automatic segmentation is region of interest (ROI) detection. A common approach is based on statistical estimation of image intensity values that could classify the tissue type of interest. Normally an assumption is made based on the intensity histogram of the ROI[12]. Sometimes the anatomical structures have to be used as guidance. For example, the liver is the biggest organ in the abdomen and adjacent to the lung area which always appears as the darkest region. Obviously, when the original images vary greatly in resolution and quality, and organ segmentation is not limited to liver, relying on such estimations is not sufficient. Alternatively, we provide interactive tools to explicitly define an interval $[K_1, K_2]$, where the intensity values of the tissue of interest lie. The same intensity interval $[K_1, K_2]$ is applied to calculate the feature image in section 2.2. Given an intensity range $[K_1, K_2]$, we have

$$I_1(x) = \begin{cases} I_0(x) & \text{if } I_0(x) \in [K_1, K_2]; \\ 0 & \text{else.} \end{cases} \quad (1)$$

The gradient magnitude of image I_1 at each pixel is computed (fig.2b) and a lower hysteresis threshold T is applied to the result to suppress spurious edges, similar to that used in the Canny edge detection algorithm, as shown in fig.2c. Currently, the threshold T is estimated using the histogram of the gradient image. However, an interactive way to adapt the threshold value in real time is also provided. The remaining edges are enhanced to the maximum intensity value C of image I_1 . These can be briefly described as Equation 2:

$$I_1'(x) = \begin{cases} C & \text{if } \nabla I_1(x) > T; \\ 0 & \text{else.} \end{cases} \quad (2)$$

Next, image I_1' is subtracted from the image I_1 . The resulting image I_2 is shown in fig.2d. The image I_2 results in better performance than image I_1 when applying morphological operations to separate adjoining tissues, as discussed in the following section. Fig.3 illustrates the differences.

$$I_2(x) = I_1(x) - I_1'(x) \quad (3)$$

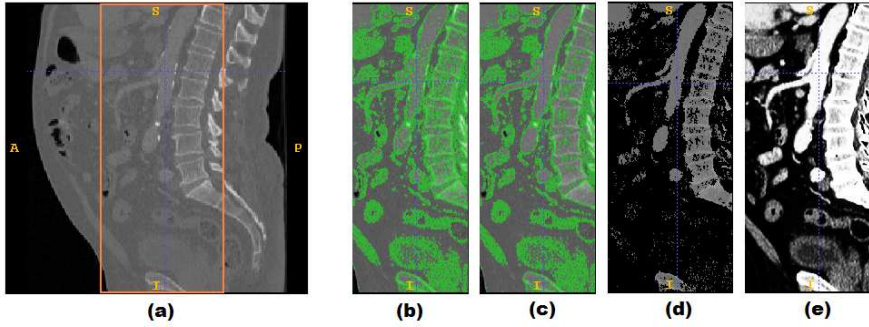


Fig. 2. Edge enhancement. (a) Original slice in sagittal view (image I_1). The area inside the rectangular box indicates the location of the abdominal aorta. (b) The gradient magnitude of image I_1 (only partial image I_1 , i.e. the area inside the rectangular box of (a) is displayed). (c) Spurious edge suppression. (d) Image I_2 after subtracting the enhanced edge from image I_1 (e) Feature map of image I_0

Mathematical morphology scheme We apply morphological erosion followed by interactive region growing algorithm to remove the areas that do not belong to the target organ. The morphological erosion is defined as:

$$E(I_2, B) = I_2 \ominus (-B) = \bigcap_{\beta \in B} (I_2 - \beta) \quad (4)$$

B is the structure element, having: $-B = \{-\beta | \beta \in B\}$. By applying it to the image I_2 , we can separate the adjoining tissues (as shown in fig.3).

Next, the object regions are extracted to provide an initial segmentation to be embedded into the level set function. Although it may be possible to automatically identify the target organ from a set of candidate regions using prior knowledge of organ shape, for best efficiency and accuracy we simply provide a user interface to guide the extraction. Starting from a user-supplied seed point

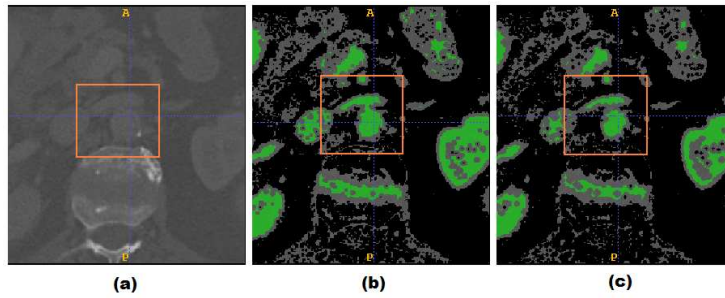


Fig. 3. Applying morphological erosion on images with or without edge enhancement. (a) Original slice in axial view (the square indicates the location of abdominal aorta). (b) Result without edge enhancement. (c) Result with edge enhancement, where the adjoining tissues have been correctly separated (indicated by the green color areas).

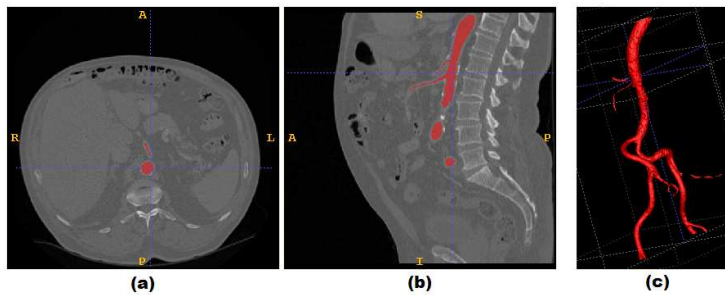


Fig. 4. Prior segmentation which is extracted from a set of candidate regions by placing one seed inside the region representing the real abdominal aorta. Red indicates the region of the prior segmentation. (a) original image in axial view. (b) original image in sagittal view. (c) 3D view of the prior segmentation result.

or a seed region, the system implements a simplified region growing algorithm based on connected-components to extract the target organ, as shown in fig.4.

The initial segmentation is further refined by a level set approach. Using the property of keeping the evolution front smooth, this can reduce some of the "leaking" that is common in connected-component schemes, e.g. applications using region growing or morphology operations.

2.2 Level Set Initialisation

It is shown in section 2.1.2 that the initial segmentation is a good approximation of the actual organ shape. In this section, the accurate shape recovery is implemented in a modified form of the basic level set equation developed in[8], i.e.

$$\frac{d}{dt}\psi + \alpha P |\nabla \psi| - \beta K |\nabla \psi| = 0 \quad (5)$$

$\psi(x, t)$ is the level set function. The evolution front is obtained by extracting the zero level set i.e. $\psi(x, t) = 0$. We embed the initial segmentation as an initial front of the function ψ at $t = 0$. The propagation term P from Equation 5 is an image based force defined from the feature image $g(I)$. In our framework, we compute the feature image using a modified version of the region competition method by Zhu and Yuille[20], where the intensity values fall in the interval $[-1, 1]$. Fig.2e displays the feature image, which is calculated according to Equation 6. The intensities of the feature image have been mapped into the interval $[0, 255]$.

$$g(I) = \{P_{obj}(i) - P_{back}(i) \mid i \in I\} \quad (6)$$

where $P_{obj}(i)$ is the probability that a pixel in the image belongs to the foreground; $P_{back}(i)$ is the probability that the pixel belongs to the background. The intensity ranges of the foreground and background have been defined in the section 2.1.1 in an interactive way.

2.3 Level Set Evolution

Fig.5 shows some screen shots obtained at intermediate evolutions to demonstrate the idea that our approach requires less iterations and can efficiently reduce the risk of leaking at weak boundaries. For comparison, we also segmented the same dataset using SNAP² where its evolution speed is calculated based on the same feature map as ours (fig.2e). As with other level set based applications, SNAP is sensitive to both the seed positions and seed numbers. Here, 27 seeds have been placed evenly along the aorta carefully avoiding areas close to weak edges (fig.5d). Other parameters required by SNAP were set to the same values as ours if possible. For our approach, the segmentation is nearly complete at 60 iterations. At 115 iterations, the result has not changed significantly, nor have any "leaks" occurred in the result. In contrast, using SNAP the aorta shape has only been roughly formed at 240 iterations, except the left common iliac (fig.5g). At 520 iterations, the aorta segmentation is completed. However, "leaking" has occurred between the abdominal aorta and the spine, as shown in fig.5h.

3 Evaluation and Experimental Results

3.1 Example results

Besides the aorta segmentation demonstrated in section 2, we visualize other segmentation results to illustrate that our method is a general approach for

² SNAP is an application developed on the National Library of Medicine Insight Segmentation and Registration Toolkit (ITK). <http://www.itksnap.org> or as part of ITK from <http://www.itk.org>

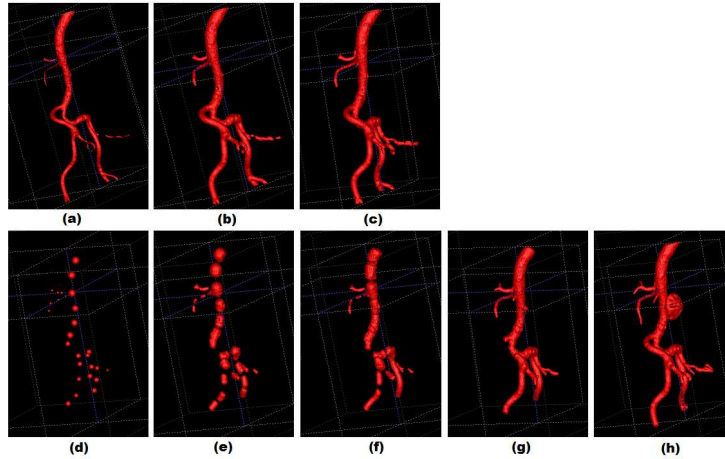


Fig. 5. Intermediate evolution results: comparison between our approach and SNAP. (a)-(c) our approach, showing results of (a) initial segmentation (b) at 60 iterations (c) at 115 iterations. (d)-(h) intermediate results from SNAP (d) initial segmentation by placing 27 seeds evenly along the aorta (e) at 60 iterations (f) at 115 iterations (g) at 240 iterations (h) at 520 iterations.

abdominal structure segmentation on varied image modalities. The same procedure and default parameters (as in section 2) were applied to obtain aorta, vein, kidney and liver segmentations (fig.6). Fig.6a shows a result from a high resolution CTA image provided by St. Mary’s London Hospital and Imperial College London. The result in Fig.6b is also from contrast enhanced CT, but at low resolution (provided by St James’s University Hospital Leeds). Fig.6c shows the segmentation from a CT image provided by Royal Liverpool University Hospital with no contrast infused. This is a typical case of right renal obstruction used in a VE for performing nephrostomy. Fig.6d is from an MR renal donor angiogram image with contrast infused, provided by Royal Liverpool University Hospital, which is used to construct a VE of renal collecting system.

The successful segmentation demonstrates the wide applicability of the work. Current tests demonstrate that other image modalities such as CT, MR and Angiogram images etc. could be suitable to segment abdominal structures and create the virtual environments. The approach is however unlikely to be successful for modalities with very poor SNR such as Ultrasound. As CT images are our major resource for creating virtual human anatomy, the evaluations in the following section focus on CTA image segmentation.

3.2 Evaluation of accuracy

We evaluated our method on 17 cases where the manual segmentation results were provided by Imperial College London. All cases are contrast enhanced images (CTA) of high resolution (provided by St. Mary’s London Hospital). The

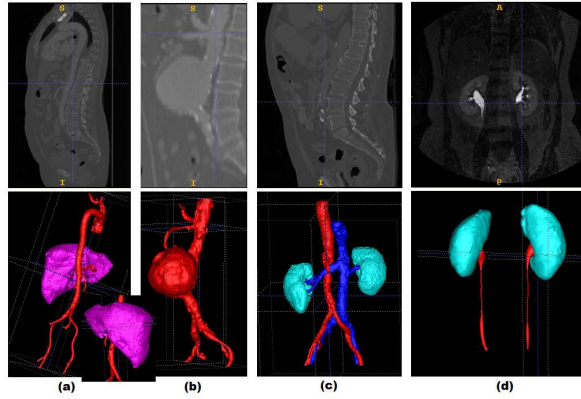


Fig. 6. Abdominal structure segmentations. (a) 275th slice (sagittal view) in image of dimension $512 \times 512 \times 615$. (b) 117th slice (sagittal view) in image of dimension $230 \times 200 \times 346$. (c) 284th slice (sagittal view) in image of dimension $512 \times 512 \times 423$. (d) 39th slice (coronal view) in image of dimension $384 \times 384 \times 65$.

segmentation results include ascending aorta, arch of the aorta, brachiocephalic arteries, common carotids, subclavian arteries, descending aorta, celiac artery, superior mesenteric artery, renal artery, common iliac arteries, external iliac arteries, internal iliac arteries and common femoral arteries. Table 1 lists some representative comparison results. The numeric evaluation is based on the measurement of volume overlapping rate[15] and voxel distance. Manual segmentation results are taken as reference models.

TPVF denotes the fraction of the total amount of tissue in reference model with which our result overlaps. The relatively low volume overlap rate is caused by the inconsistent segmentation along the aorta medial axis when it is performed by different observers. The main differences between our result and the manual segmentation are at the common carotids, subclavian arteries and renal artery (as shown in fig.7c). Although there is a basic segmentation guidance on which part of the aorta should be segmented, it is impossible to define case by case on how far those branches should be presented in the segmentation result. Fig.7 visualizes the differences using the case of STM002, where the blue depicts those voxels which are missed by our method but included by the manual segmentation (mainly at common carotids, subclavian arteries and ascending aorta); the yellow illustrates voxels which are missed by the manual segmentation but correctly identified by our method (mainly at the renal artery and external iliac arteries). Here, red indicates voxels of being segmented by both methods. When results are evaluated explicitly on the specified areas which are common to both methods, the performance improves significantly, as shown in Table 2. The datasets STM002 and STM010 are taken as examples, as they currently have the worst performances.

Table 1. Evaluation results

| Dataset | FNVF | FPVF | TPVF | Max. Positive Dist.[<i>mm</i>] | Max. Negative Dist.[<i>mm</i>] | Ave. Positive Dist.[<i>mm</i>] | Ave. Negative Dist.[<i>mm</i>] |
|---------|--------|--------|--------|----------------------------------|----------------------------------|----------------------------------|----------------------------------|
| STM002 | 0.1764 | 0.1329 | 0.8236 | 35.15 | 25.48 | 2.91 | 2.31 |
| STM003 | 0.1016 | 0.0286 | 0.8984 | 32.81 | 21.09 | 2.72 | 2.07 |
| STM004 | 0.1083 | 0.0706 | 0.8917 | 20.26 | 10.91 | 2.56 | 2.04 |
| STM005 | 0.1575 | 0.0389 | 0.8425 | 26.62 | 12.85 | 2.79 | 2.40 |
| STM006 | 0.1636 | 0.0824 | 0.8364 | 27.25 | 17.03 | 2.58 | 2.37 |
| STM007 | 0.1511 | 0.0789 | 0.8489 | 31.38 | 23.77 | 3.11 | 2.35 |
| STM008 | 0.1368 | 0.0567 | 0.8632 | 36.70 | 24.75 | 3.02 | 2.28 |
| STM009 | 0.1371 | 0.0367 | 0.8629 | 30.69 | 12.27 | 2.43 | 2.69 |
| STM010 | 0.2469 | 0.0638 | 0.7530 | 28.94 | 26.66 | 2.33 | 2.30 |
| STM011 | 0.0814 | 0.0577 | 0.9186 | 16.60 | 16.60 | 2.57 | 2.87 |
| STM012 | 0.0552 | 0.1246 | 0.9448 | 20.39 | 21.28 | 2.47 | 2.45 |
| STM013 | 0.0843 | 0.0732 | 0.9157 | 40.62 | 14.06 | 2.24 | 2.08 |

Table 2. Performance evaluation is carried out explicitly on the specified areas

| Dataset | FNVF | FPVF | TPVF |
|---------|--------|--------|--------|
| STM002 | 0.0434 | 0.1002 | 0.9566 |
| STM010 | 0.0551 | 0.0414 | 0.9449 |

The segmentation resolution can also cause differences between two methods. This can be seen in fig.7, where the descending aorta has been amplified and displayed at the right corner of (a) and (b), respectively. As shown in fig.7a, being done slice by slice on DICOM data, the manual segmentation normally has aliasing artefacts in the result. On the contrary, our method refines the segmentation using the level set, which helps to smooth the blood vessel wall, as shown in fig.7b.

3.3 Evaluation of efficiency

The practical viability should also be considered when evaluating a semi-automatic segmentation method. The computational time and the human operator time required to complete segmentation can be used to characterize the efficiency of a segmentation method.

Our system includes computing the image gradient and the level set task for which the computational time increases significantly when image resolution and data size increases. The datasets in table 1 have also been used to test the efficiency of our system. From the data we currently have, they represent the largest volume size and the highest resolution. The data resolutions range from $0.779297mm \times 0.779297mm \times 1mm$ to $0.951172mm \times 0.951172mm \times 1mm$. The data dimensions vary from $512 \times 512 \times 554$ to $512 \times 512 \times 659$. All 17 cases are contrast-enhanced CTA. Because of the simplicity of the user interactions in

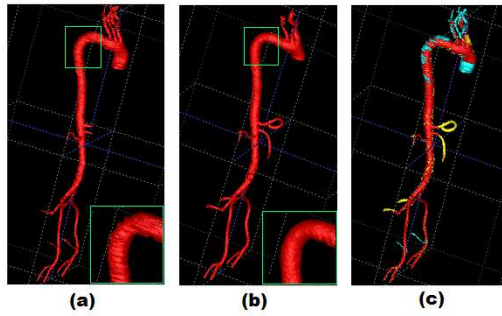


Fig. 7. Visualization of the differences between our result and the manual segmentation result on case STM002. (a) Manual segmentation result. (b) Our segmentation result. (c) Visualization of differences.

our system, the human operation time is negligible compared to the computational time of the image processing and level set tasks, so we do not time them separately. The evaluation is carried on a PC with a Core2 CPU at $2.66GHz$. The average segmentation time is 5 minutes to obtain the segmentation accuracy shown in table 1. In contrast, for another semi-automatic level set based approach (SNAP), a minimum of 2 hours is needed for the same dataset, where the segmentations were completed by an experienced medical student. No exact operation time has been given for the manual segmentation.

4 Conclusion and Future Work

One of our primary motivations in developing this framework is to achieve both greater efficiency and accuracy in segmentation on a variety of image modalities and for a variety of structures. Our approach combines image processing techniques and mathematical morphology operations to identify the tissue of interest and obtain an initial segmentation close to the target structure shape. The initial segmentation is automatically embedded into the level set function to obtain a refined segmentation result. Note that only minor intervention is required to set up individual computations. Traditional seed positioning is replaced by seed fronts representing a good approximation to the original structures. Consequently only 50 to 70 iterations are needed to propagate to the structure boundaries. This dramatically decreases processing time and reduces the risks of leaking at the weak boundaries, without compromising the accuracy of segmentation. Currently, the default parameters used by our system work well in a variety of image modalities, such that adjustment of these parameters for each case which is common in other level set based methods tends not to be necessary. The evaluation will be extended to other image modalities as manual segmentations become available.

Acknowledgements: This work is funded by the UK Engineering and Physical Science Research Council (EP/E002749). The authors would like to thank Dr Fernando Bello and Dr Vincent Luboz from Imperial College (St. Mary's London Hospital) for help with collecting the test data and providing manual segmentations for evaluations. We would also like to thank Dr Derek Gould in University of Liverpool for data acquisition and valuable clinical advice.

References

1. Campadelli, P. and Casiraghi, E. *Liver Segmentation from CT Scans: A Survey*. LNCS 4578, pp.520-528, Springer Berlin, 2007.
2. Caselles, V., Kimmel, R. and Sapiro, G. *Geodesic Active Contours*. International Journal of Computer Vision, 22(1) 6179, 1997.
3. Droske, M., Meyer, B., Rumpf, M. and Schaller, K. *An adaptive Level Set Method for Medical Image Segmentation*. 17th Int. Conf. on Info. Proc. in Medi. Ima. 2001.
4. Gao, L., Heath, D.G., Fishman, E.K. *Abdominal Image Segmentation Using Three-dimensional Deformable Models*. Investigative Radiology 33(6), pp.348-355, 1998.
5. Heimann, T., Meinzer, H.P. and Wolf, I. *A Statistical Deformable Model for the Segmentation of Liver CT Volumes*. Proc. MICCIA2007 workshop.
6. Kirbas, C. and Quek, F. *A Review of Vessel Extraction Techniques and Algorithms*. ACM Computing Surveys, vol.36, no.2, pp.81-121, 2004.
7. Museth, K., Breen, D.E., Whitaker, R.T., Mauch, S., and Johnson, D. *Algorithms for Interactive Editing of Level Set Models*. Computer Graphics Forum 24, 4, pp.1-22, 2005.
8. Malladi, R., Sethian, J.A. and Vemuri, B.C. *Shape Modeling with Front Propagation: A Level Set Approach*. IEEE Trans. Pat. Ana. and Mach. Intel. vol.17, No.2, 1995.
9. Park, H., Bland, P.H. and Meyer, C.R. *Construction of an Abdominal Probabilistic Atlas and Its Application in Segmentation*. IEEE Trans. on Medi. Ima. vol.22, no.4, pp.483-492, 2003.
10. Pan, S. and Dawant, B.M. *Automatic 3D Segmentation of the Liver from Abdominal CT images: A Level-set Approach*. Proc. SPIE-Int. Soc. Opt. Eng., Medical Imaging 2001: Image Processing, San Diego, CA, pp.19-22, 2001.
11. Pohle, R., Toennies, K.D. *Segmentation of Medical Images Using Adaptive Region Growing*. Proc. SPIE Medical Imaging 4322, pp.1337-1346, 2001.
12. Rusko, L., Bekes, G., Nemeth, G. and Fidrich, M. *Fully Automatic Liver Segmentation for Contrast-enhanced CT Images*. Proc. MICCIA2007 workshop.
13. Sethian, J.A. *Level Set Methods and Fast Marching Methods: Evolving Interfaces in Computational Geometry, Fluid Mechanics, Computer vision, and Material Science*. Cambridge University Press, UK, 1999.
14. Suri, J.S., Liu, K., Reden, L. and Laxminarayan, S. *A Review on MR Vascular Image Processing: Skeleton Versus Nonskeleton Approaches II*. IEEE Trans. on Info. Tech. in Biomedicine, vol.6, no.4, 2002.
15. Udupa, J., LeBlanc, V., Schmidt, H., Imielinska, C., Saha, P., Grevera, G., Zhuge, Y., Molholt, P., Jin, Y. and Currie, L. *A Methodology for Evaluating Image Segmentation Algorithm*. SPIE Medical Imaging, San Diego CA, USA, 2002.
16. Whitaker, R.T., Breen, D.E., Museth, K. and Soni, N. *A Framework for Level Set Segmentation of Volume Datasets*. Proc. Volume Graphics 2001, pp 159-68.

17. Watanabe, M., Kikinis, R. and Westin, C. *Level Set Based Integration of Segmentation and Computational Fluid Dynamics for Flow Correction in Phase Contrast Angiography*. LNCS2489 pp.405-412, Proc.5th Int.Conf.on MICCAI2002.
18. Wang, K.C., Taylor, C.A., Hsiau, Z., Parker, D. and Dutton, R.W. *Level Set Methods and MR Image Segmentation for Geometric Modelling in Computational Hemodynamics*. Proc. 20th Annual Int. Conf. of the IEEE Eng. in Medi. and Bio. Soc. vol.20, no.6, 1998.
19. Too, S.W., Cho, J.S., Noh, S.M., Shin, K.S. and Park, J.W. *Organ Segmentation by Comparing of Grey Value Portion on Abdomial CT image*. Proc. 5th Int. Conf. on Sig. Proc. Beijing, pp.21-25, 2000.
20. Zhu, S.C. and Yuille, A. *Region Competition: Unifying Snakes, Region Growing, and Bayes/MDL for Multiband Image Segmentation*. IEEE Trans.on Pat.Ana.and Machine Intel. vol.18, No.9, 1996.

Automatic Stent Implant Follow-up in Intravascular Optical Coherence Tomography Images

Serhan Gurmeric¹, Gozde Unal¹, Stephane Carlier², Yan Yang³, and Greg Slabaugh³

¹ Faculty of Engineering and Natural Sciences, Sabanci University, Turkey
{sgurmeric, gozdeunal}@sabanciuniv.edu,

² Cordis Corporation J&J, Belgium,

³ Siemens Corporate Research, Princeton, NJ USA

Abstract. Atherosclerotic plaques and their rupture cause narrowing or blockage of the coronary arteries and may lead to sudden cardiac death. As a remedy, after a coronary angioplasty, often a stent is implanted to prevent restenosis. Although it was observed that drug-eluting stents can significantly reduce the occurrence of neointimal hyperplasia, in-stent restenosis still occurs, therefore, studying the distribution of the stent struts during patient follow-ups is important. In this paper, we will present new computer methods for automated analysis of strut distribution in monitoring the restenosis and degree of neointimal tissue growth over struts from the intravascular optical coherence tomography data. Our system will be a useful computer-aided monitoring tool for follow-up studies of stent implantation in the clinical workflow.

1 Introduction

Coronary artery diseases such as atherosclerosis are the leading cause of death in the industrialized world. Medical imaging techniques have greatly assisted the diagnoses and treatments for coronary artery diseases. These imaging approaches include coronary X-ray angiography, computed tomography angiography (CTA), magnetic resonance angiography (MRA), intravascular ultrasound (IVUS), and optical coherence tomography (OCT). Among them, CTA and MRA are non-invasive imaging modalities, but the low resolution has limited their ability to resolve different constituents of atherosclerotic plaques. IVUS and intravascular OCT, however, are able to achieve much higher resolution than CTA and MRA by performing invasive catheterization on patients. OCT is a relatively new imaging technique that is analogous to ultrasound, but it measures the intensity of back-reflected infrared light instead of acoustical waves [1]. OCT has shown promise as a method for intravascular imaging, and was compared to IVUS in several works [2, 3]. The biggest advantage of OCT is its high resolution. Both in vitro and in vivo studies [2, 4] have shown that the resolution (on the order of 10 μm) can not only differentiate between typical constituents of atherosclerotic plaques, such as lipid, calcium, and fibrous tissue, but can also resolve the thin fibrous cap that is thought to be responsible for plaque vulnerability[5]. Atherosclerotic plaques may cause narrowing or blockage of the coronary arteries, resulting in reduced blood supply to the heart tissue, and sometimes lead to serious results such as heart attacks. To open a blockage, the procedure of percutaneous transluminal coronary angioplasty (PTCA) is usually applied, and a stent is often implanted after angioplasty to keep the artery open and prevent restenosis (regrowth of the plaque). Stents are small metal scaffolds either made from bare metal or coated with drug to inhibit restenosis. The

former are known as bare-metal stent (BMS) and the latter are known as drug eluting stents (DES). It was observed that drug-eluting stents can significantly reduce the occurrence of neointimal hyperplasia (NIH) [6]. However, in-stent restenosis after drug-eluting stents implantation still occurs[7]. Studies have shown that nonuniform circumferential stent strut distribution affects local drug concentration [8], thus the number and distribution of the stent struts might also affect the magnitude of NIH after stent implantation in human coronary arteries [9]. Therefore, automatic computer methods for analysis of strut distribution in monitoring the restenosis and degree of neointimal tissue growth over struts will help the clinical workflow and increase efficiency of stent implant follow-ups.

Previous studies on stent strut distribution, mentioned above, performed manual detection and measurement of the stent struts, and require enormous amount of time to process OCT pullbacks. An automatic stent detection method in [10] was developed by using brightness pattern in IVUS images. In this paper, we present a novel automated method for analysis of strut distribution during stent implant follow-up in patients from the OCT pullback datasets, which exhibit different characteristics than IVUS data. We developed a new spline contour evolution for delineating both the lumen boundary and the struts in the case of neointimal hyperplasia. We then describe an algorithm for detecting stent struts in a series of OCT images. In our developed computer application, for clinical use purposes, we also incorporated interactive features for correcting the splines and marking struts if necessary. Section 2 explains the steps and details of our algorithm, Section 3 presents the validation results and experiments, and Section 4 concludes with discussions.

2 Method

In this section, we explain our method for stent detection and analysis in OCT pullbacks. The raw image data format is in the rectangular domain as shown in Figure 1.a, and we developed our method completely using the native image data rather than the scan-converted polar image in Figure 1.b.⁴

2.1 Preprocessing the OCT pullbacks

Catheter artifacts, which form ring-like shadows around the catheter center in the image interferes with the image processing operations such as computation of image gradients, therefore, a prefiltering of the image is usually required.

We observe that in OCT pullbacks, the arterial wall and stent struts fall into the brighter intensity range, which hence contains the useful target information for our purposes. As a preprocessing step, we carry out a histogram based filtering approach to exploit this character of the OCT image. The density for image intensities, call $p(i)$, is estimated through a histogram, and typically, a unimodal distribution with a heavy tail towards the bright intensity side is obtained (Figure 1.c). The most likely value of $p(i)$, i.e. its mode, is computed. To eliminate the noise from the lower intensities, and concentrate on the brighter side of the density values on the right side of the mode, a certain percentage, say b , of the mode is computed, and all those intensities below that value is annihilated to 0 (Figure 1.f). After this step, a Gaussian filter with a variance of $\sigma = 2.5$ was applied and a morphological opening operation was performed to remove the remaining isolated bright pixels in dark

⁴ Note that in the intravascular image processing community, the terms polar and rectangular image are used interchangeably. We call the display image (circular) as the polar image and the raw image as the rectangular image as recommended by the cardiologist imaging expert in the team.

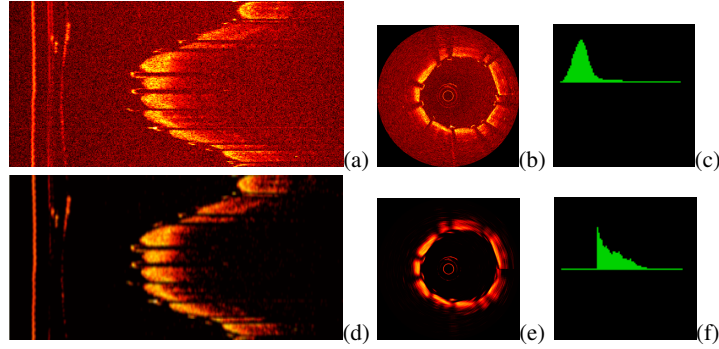


Fig. 1. (a) raw image (rectangular domain); (b) display image (polar domain); (c) Density estimate of the image (a); (d) rectangular image after filtering (a); (e) display image of (d); (f) Density estimate of the image (d).

regions. The result of the overall pre-filtering operation is shown in Figure 1.d-e. The pre-filtered image will be utilized next in the spline contour propagation step, which will be followed by the strut detection.

2.2 Spline Segmentation for Lumen and Stent

The lumen boundary is represented by a deformable spline contour and will be propagated with ordinary differential equations, which will be derived for its evolution. Deformable models or active contours [11] have proven to be versatile models in segmentation of various anatomic structures such as vessel borders [12].

First, as required in most active contour methods, a good initialization is preferable for the success of the active contour method. For that purpose, we will detect the arterial wall that appears as a wide bright 1-dimensional (1D) blob from the near field towards the far field of the catheter.

Spline Initialization: We developed an algorithm for initializing our spline control points on a pullback image frame as follows:

1. Shoot rays from the center of the image, i.e. take a row, say row y , of the rectangular image, apply a closing operation (dilate and erode) to smooth and fill small gaps in order for the 1D signal $I(x)$ where $x \in [0, N]$ to become differentiable. This operation is done on every other k^{th} row (e.g. 6th) to initialize a certain variable number of control points of the spline so that enough variability of the lumen contour will be captured.
2. Detect the following over each 1D signal:

$$(I(x_1) = 0) \& \left(\frac{dI(x_1)}{dx} > 0 \right) \quad (1)$$

then

$$\left(\frac{dI(x_2)}{dx} < 0 \right) \& (I(x_2 + 1) = 0) \quad (2)$$

These rules lead to detection of the bright intensity peaks.

3. Over the detected intervals $h = x_2 - x_1$, find the maximum width h .
4. If $h <$ "minimum width threshold", go to the next selected row signal, i.e. go to step 1.
5. If a maximum h is found, detect the beginning of that interval, i.e. x_1 . Record x_1 as the control point.
6. Repeat 1-5 until all rows of the rectangular image is processed.
7. The spline now can be initialized at the control point set (x_1, y) collected via the above algorithm.

Spline Evolution: We utilized a cubic spline, with four polynomial blending functions. The initial spline obtained from our method above is usually very close to the lumen border, and is only supposed to evolve a few pixels for a refinement. We utilize a geodesic active contour energy functional [13, 14]:

$$E(C) = w_1 \cdot \text{image term} + w_2 \cdot \text{smoothness term} = w_1 \int_C F ds + w_2 \int_C ds \quad (3)$$

where w_1, w_2 are the weights of the data term and the smoothness term on the contour, and $F = g(|\nabla I|)$, where g is a monotonically decreasing function inversely proportional to the image gradient: $g = 1/(1 + |\nabla I|)$.

In an earlier similar spline-based active contour work [15], uniform rational B-splines [16] were utilized. Here, the lumen contour is represented with a Catmull-Rom spline, which belong to a family of cubic interpolating splines, [17] with four cubic polynomials functions: $h_{00}(t) = 2t^3 - 3t^2 + 1$, $h_{10}(t) = t^3 - 2t^2 + t$, $h_{01}(t) = -2t^3 + 3t^2$, and $h_{11}(t) = t^3 - t^2$, where $t \in (0, 1)$ for each interval, i.e. between two control points. One difference of Catmull-Rom splines from B-splines is that the interpolated contour goes exactly through the control points since the segments are formed using the two end points P_j and P_{j+1} and their tangents T_j and T_{j+1} :

$$C_j(t) = h_{00}(t)P_j + h_{01}(t)P_{j+1} + h_{10}(t)T_j + h_{11}(t)T_{j+1}, \quad j = 1 \dots K \quad (4)$$

The contour C will be a concatenation of the segments C_j . Note that the control points P_j and segments C_j have the same index for a clockwise transversal of the spline, and very close control points will be deleted for regularity of the contour. The tangent vectors are formed by the simple three point differences:

$$T_j = \frac{(P_{j+1} - P_j) * 0.5}{|(P_{j+1} - P_j)|} + \frac{(P_j - P_{j-1}) * 0.5}{|(P_j - P_{j-1})|} \quad (5)$$

for internal points $j = 2, \dots, K - 1$, and one-sided differences are used at the endpoints of the control point set. One nice property of the Catmull-Rom spline is its practicality for interaction purposes because when the user clicks to draw or correct spline points, the constructed contour goes through the exact points, which the user marks.

We propose a new modified spline evolution, in which the control points of the spline will be evolved by integrating image energy terms from its two adjacent segments. The differential equation for the control points, i.e. the motion equation of the spline, are thus obtained as:

$$\frac{\partial P_j}{\partial t} = \int_{C_j} (w_1 F \kappa + w_2 \kappa) N_j ds + \int_{C_{j-1}} (w_1 F \kappa + w_2 \kappa) N_{j-1} ds - w_1 \left(\int_{C_j} \nabla F_n + \int_{C_{j-1}} \nabla F_n \right) \quad (6)$$

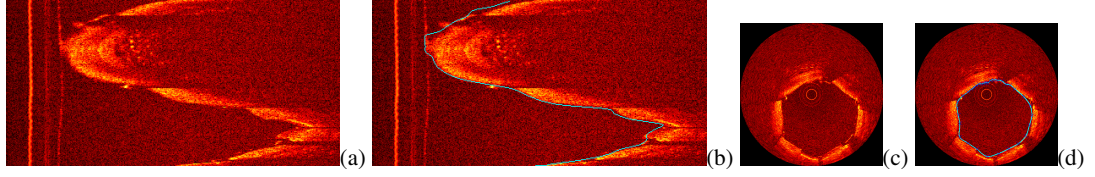


Fig. 2. (a) and (c) OCT images without splines; (b) and (d) with splines deformed to fit to the lumen border.

where κ is the curvature on the spline segment, and N_j is the unit normal vector over the segment C_j , which is the next segment and C_{j-1} is the previous segment for the control point P_j . The last two terms include the normal component: $\nabla F_n = (\nabla F \cdot N)N$. Geodesic active contours have a well-known drawback as being too local during contour evolution since they depend on pointwise image gradients. With Eq (6), this problem is alleviated by the both the semi-globalization and the smoothing effect provided by integration of the image terms on two adjacent spline segments of the current control point.

In summary, Eq (6) updates the control points P_j , and hence the contour C is updated to deform towards the lumen border in a smooth geometry as shown in sample results in Figure 2.

Three situations require attention during processing OCT pullbacks for stent implant follow-up: newly implanted stent case; minimum neointimal hyperplasia case such as a follow-up of a DES; and more important NIH or instent restenosis cases, which all present different challenges to the algorithm.

Newly Implanted Stent case: This is the situation with a stent freshly implanted into the artery, hence the vessel wall tissue did not have the chance to grow over the struts yet. The struts shadows are usually visible as in Figure 2. The first spline contour estimated using the update equation Eq (6) is used in strut detection which will be explained in the next section.

Minimum and Important Neointimal Hyperplasia Cases: In the follow-up studies of stent implantation, the stent struts are usually not directly in contact with the blood pool. Instead, there is an extra layer of neointimal hyperplasia (NIH). Figure 3 depicts a case with minimal NIH development (a) and a case with more prolific development of NIH (c). For a strut detection using our method (next subsection) on the images with NIH, the results would not be satisfying because the lumen spline segmentation result is far away from the actual stent boundary. The spline contour estimated using the update equation Eq (6) is used as the first spline, and a second one is initialized as a dilated version of the first one over the artery wall. Then, Eq (6) is used for the second spline as well over smoothed image intensities. This second spline then gets stuck at the bright strut edges, and will be used in the strut detection that will be explained in the next section. Fig. 3(b) and (d) show the two spline contours on the OCT images with NIH.

2.3 Stent Strut Detection

Looking at a typical OCT frame with stents (Figure 4-a), it is easy to observe that stent struts usually block the penetration of the infrared light and leave a dark shadow in the

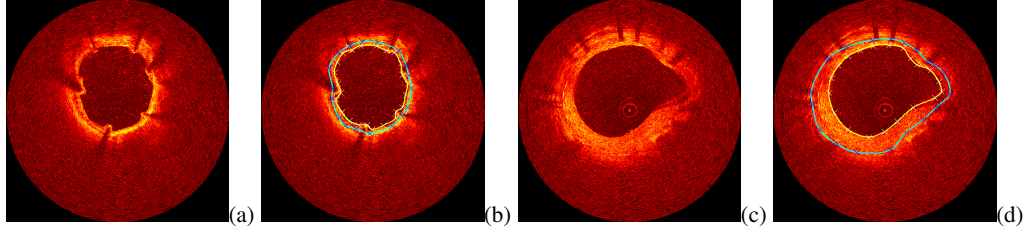


Fig. 3. (a) an OCT image frame with minimum NIH; (b) Spline is deformed over the image (a) to fit to the strut boundary; (c) an OCT image frame with extreme NIH; (d) Spline is deformed the over image (c) to fit to the strut boundary.

far field of the image domain. We developed a stent strut detection algorithm based on the shadows by shooting imaginary rays from the center of the catheter to imitate the real light beams. Traversing the rows of the rectangular OCT image data, and starting from the spline contour C on each row, we sample the intensity profile towards the far field to form the energy:

$$E(y) = \int_{C(y,x)}^{C(y,x+r)} I(x) dx$$

This forms a vector of estimated energies in the vicinity of the lumen contour in its normal direction, which coincides with the infrared beam direction. Here, r , which is the extent of the energy interval, is a certain percentage set intuitively and heuristically, e.g. 10% of the range size M (column size) of the rectangular image.

Next, to detect possible shadows of struts, using the normal energy, the contour is traversed tangentially. The energy $E(y)$'s are differentiated to detect the start and end of the strut shadows. Hence, the following rules are obtained:

$$\text{Strut} = \begin{cases} \text{strut shadow start} & \text{if } \nabla E^-(y) < S\% \\ \text{strut shadow end} & \text{if } \nabla E^+(y) < S\% \end{cases} \quad (7)$$

where the ∇^- and ∇^+ indicate discrete approximations to one-sided derivatives of E on each side of the current coordinate y , normalized to $(0,1)$, and S is a percentage that signifies the drop in the energy of the intensity, hence the strut shadow. The parameter S was set to 80%.

Even if the struts are narrow and have vague trailing shadows, our strategy of traversing the image both in radial and tangential vessel wall direction and integrating the intensities helps improve the robustness. Our shadow detection algorithm works for most cases when there are reasonably defined trailing shadows of struts, as shown in Figure 4. In the figures, the circles depict the struts that are detected by our algorithm with their radii indicating the width of the shadow, hence an approximation to the strut width. As can be seen from images in (c)-(f), starting from the second spline contour, our algorithm is able to detect struts in the more challenging NIH imaging scenarios as well.

Sew-up stitch problem in the Pullbacks: A typical artifact, called as the sew-up stitch, is observed in Figure 5.a at 8 o'clock. During a pullback operation, the catheter is moving while sending the light beam sideways to image the vessel wall. As the full 360° rotation

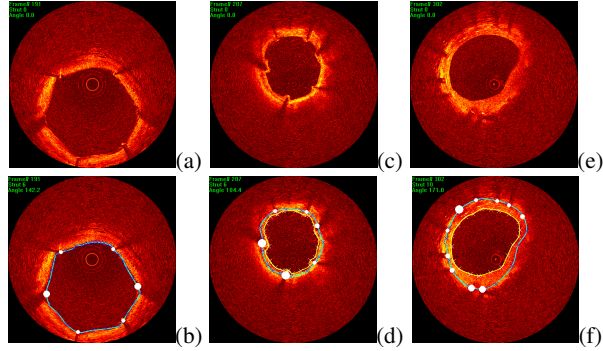


Fig. 4. (a) an OCT image frame with newly implanted stents; (b) detected struts ; (c) image with minimum NIH case; (d) detected struts over the second spline; (e) image with extreme NIH case; (f) detected struts over the second spline.

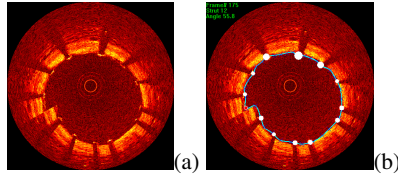


Fig. 5. (a) an OCT image frame with sew-up stitching problem; (b) Detected and marked with a red circle.

is completed for recording one cross-section image, the catheter has already advanced slightly in physical space in $1/15^{th}$ of a second during a catheter pullback at 1mm/s , therefore, the 0° and 360° beams do not end up at the same position, and the sew-up stitches appear as easily observed as a seaming artifact in the display image. Our strut detection method will sometimes label these artifacts as struts when they leave shadow-like trails. Therefore, we detect this situation by computing the tangent of the spline on the rectangular image, and the persistence of the orientation of the tangent vector to stay roughly horizontal (i.e. $\pm 10^\circ$) for a few positions on the contour. Figure 5.b shows an example detection of the stitch region and it is marked with a red circle and later removed from the strut list.

3 Results

Our data set consisted of 20 *in vivo* OCT pullbacks of each several hundred image frames, with raw rectangular image size of $N \times M = 200 \times 700$. The pullback images were acquired with a LightLab OCT transducer and the pullback speed was 1mm/s with an axial resolution of 12 microns. Parameters in our algorithm are fixed as follows. The density mode parameter b in the prefiltering step, is set to 15%. The "minimum width threshold" in the spline initialization step is set to 20% of the rectangular image column M . For the spline motion equation Eq 6, the weight $w_1 = 1$, and $w_2 = 0.1$. Our method is robust against the parameter set, and once set, they were not changed during the experiments.

Our algorithm works in near real time, which takes less than 1 second to complete the spline segmentation and strut detection, therefore can be used interactively online.

For our validation studies, we compared manual strut detection with automatic detection over a set of images. The expert interventional cardiologist in our team, went through 7 of the OCT pullbacks and tested our method over a total of 33 images. Among these seven pullbacks, three of them had newly implanted stents, three had minimum NIH in the stents (DES), and one had much more NIH (BMS) over stents. For the assessment of

| Cases | % correctly detected number of struts | Max Angle btw struts | Stent Eccentricity |
|-------------|---------------------------------------|----------------------|--------------------|
| New Implant | 0.86 ± 0.12 | 59.6 ± 15.4 | 0.73 ± 0.08 |
| NIH Cases | 0.86 ± 0.09 | 77.5 ± 21.3 | 0.67 ± 0.11 |
| All cases | 0.86 ± 0.10 | 71.3 ± 21.1 | 0.69 ± 0.10 |

Table 1. Validation Studies: Normalized number of detected struts, maximum angle between struts, stent eccentricity are calculated over our dataset with newly implanted stent cases and neointimal tissue growth cases.

strut distribution, on each image frame, we measure the total number of detected struts, the strut eccentricity, and the maximum angle between the struts as shown in Table 1 as the mean \pm standard deviation values. The percentage of correctly detected struts is calculated over each image as $1 - \text{normalized error}$ where the normalized error is defined as the absolute difference between the number of struts marked by the physician and the number of struts detected by our algorithm, which is later normalized by the physician marked strut count. In these first set of validation studies, our algorithm achieved a reasonably good accuracy in detection, which is around 86%.

One interesting parameter to assess is the maximum angle between struts in a frame. Looking from a circular distribution point of view, if one half of the stent circumference has less struts than the other, this may be an indicator for less drug presence hence more NIH on that side of the vessel wall.

Another measure we calculated is the stent eccentricity, defined as the minimum divided by the maximum stent diameter calculated by our algorithm. This is another indicator for malpositioning of the stent as can be observed in the last column of Table 1 farther away from 1, the ideal eccentricity.

Finally, the computer application we have developed is aimed at clinical use, therefore, we have included interaction components such as possibility of correcting the spline contours, and marking the struts that are misdetected. To distinguish between the different phases after stent implant, mode of operation is easily chosen to indicate that the OCT pullback has a newly implanted stent or an NIH case, so that in the latter case a second spline contour can be estimated or drawn by the user.

4 Conclusions and Discussions

We presented novel computational methods for automatic stent implant follow-up from OCT pullbacks. We developed a new spline-based segmentation method for both the lumen boundary and stent strut boundaries. Following that, we described a strut detection

algorithm by detecting their trailing shadows in the OCT images, which is to the best of our knowledge new in the computational medical imaging. In the end, a strut distribution analysis is carried out and a number of measures important for stent implant follow-up and monitoring of the neointimal tissue growth over struts are calculated. Our experimental results demonstrated that our algorithm works well on the segmentation of target boundaries in OCT images, and detected stent struts and their trailing shadows in presence. In most cases, the shadow that corresponds to a stent strut is visible and detectable, but sometimes there are struts whose trailing shadows are not visible. Our ongoing work to improve our method includes a second pass to follow the contour and detect the visible bright struts, which were missed with the shadow detection only.

Our results and initial validation tests are very promising, however, further extensive validation studies will be performed to test and improve our stent follow-up analysis system. Our algorithm provides a convenient tool that automatically detects and analyzes the distribution of stent struts, thus reduces a lot of manual work that is associated with this task and thus will be a useful computer-aided monitoring tool in the procedure of stent implantation and its follow-up studies.

References

1. Brezinski, M.E., Tearney, G.J., Brett, B.E.: Imaging of coronary artery microstructure with optical coherence tomography. "American Journal of Cardiology" **77** (1996) 92–93
2. Jang, I., Bouma, B., Kang, D., Park, S., Park, S., Seung, K., Choi, K., Shishkov, M., Schlendorf, K., Pomerantsev, E., Houser, S., Aretz, H., Tearney, G.: Visualization of coronary atherosclerotic plaques in patients using optical coherence tomography: Comparison with intravascular ultrasound. "American Journal of Cardiology" **39** (2002) 604–609
3. Patwari, P., Weissman, N.J., Boppart, S.A., Jesser, C., Stamper, D., Fujimoto, J.G., Brezinski, M.E.: Assessment of coronary plaque with optical coherence tomography and high-frequency ultrasound. "American Journal of Cardiology" **85** (2000) 641–644
4. Yabushita, H., Bouma, B., Houser, S., Aretz, H., Jang, I.K., Schlendorf, K., Kauffman, C., Shishkov, M., Kang, D.H., Halpern, E., Tearney, G.: Characterization of human atherosclerosis by optical coherence tomography. "Circulation" **106** (2002) 1640–1645
5. Xu, C., Schmitt, J., Carlier, S., Virmani, R.: Characterization of atherosclerosis plaques by measuring both backscattering and attenuation coefficients in optical coherence tomography. "Journal of Biomedical Optics" **13**(3) (2008)
6. Sousa, J., Costa, M., Sousa, A., Abizaid, A., Seixas, A., Abizaid, A., Feres, F., Mattos, L., Falotico, R., Jaeger, J., Popma, J., Serruys, P.: Two-year angiographic and intravascular ultrasound follow-up after implantation of sirolimus-eluting stents in human coronary arteries. "Circulation" **107** (2003) 381–383
7. Lemos, P., Saia, F., Ligthart, J., Arampatzis, C., Sianos, G., Tanabe, K., Hoye, A., Degertekin, M., Daemen, J., McFadden, E., Hofma, S., Smits, P., de Feyter, P., van der Giessen, W., van Domburg, R., Serruys, P.: Coronary restenosis after sirolimus-eluting stent implantation: morphological description and mechanistic analysis from a consecutive series of cases. "Circulation" **108** (2003) 257–260
8. Hwang, C.W., Wu, D., Edelman, E.R.: Physiological transport forces govern drug distribution for stent-based delivery. "Circulation" **104** (2001) 600–605
9. Takebayashi, H., Mintz, G., Carlier, S., Kobayashi, Y., Fujii, K., T.Yasuda, Costa, R., Moussa, I., Dangas, G., Mehran, R., Lansky, A., Kreps, E., Collins, M., Colombo, A., Stone, G., Leon, M., Moses, J.: Nonuniform strut distribution correlates with more neointimal hyperplasia after sirolimus-eluting stent implantation. "Circulation" **110** (2004) 3430–3434

10. Dijkstra, J., Koning, G., Tuinenburg, J., Oemrawsingh, P., Reiber, J.: Automatic stent border detection in intravascular ultrasound images. In: Proceedings of CARS. (2003) 1111–1116
11. Kass, M., Witkin, A., Terzopoulos, D.: Snakes: Active contour models. *Int. J. Computer Vision* **1**(4) (January 1988) 321–331
12. Unal, G., Bucher, S., Carlier, S., Slabaugh, G., Fang, T., Tanaka, K.: Shape-driven segmentation of the arterial wall intravascular ultrasound images. *IEEE Trans. Information Technology in Biomedicine* **12**(3) (2008) 335–347
13. Caselles, V., Kimmel, R., Sapiro, G.: Geodesic active contours. In: ICCV95. (1995) 694–699
14. Kichenassamy, S., Kumar, A., Olver, P., Tannenbaum, A., Yezzi, A.: Gradient flows and geometric active contours. In: Proc. ICCV. (1995) 810–815
15. Slabaugh, G., Kong, K., Unal, G., Fang, T.: Variational guidewire tracking using phase congruency. In: MICCAI, LNCS 4792, Brisbane, Australia, Springer (2007) 612–619
16. van Dam Foley, J., Feiner, S., Hughes, J.: *Computer Graphics: Principles and Practice*. 2nd edn. Addison Wesley Reading (1996)
17. Catmull, E., Rom, R.: A class of local interpolating splines. In Barnhill, R.E., Reisenfeld, R.F., eds.: *Computer Aided Geometric Design*, Academic Press, New York (1974) 317–326

Detection of Coronary Calcifications Using Supervised Hierarchical Classification

U. Kurkure, D.R. Chittajallu, G. Brunner,
R.P. Yalamanchili and I.A. Kakadiaris

Computational Biomedicine Lab, Depts. of Computer Science, Elec. & Computer Engineering, and Biomedical Engineering, Univ. of Houston, Houston, TX, USA
{ukurkure,rchittajallu,gbrunner,rpyalamanchili2,ioannisk}@uh.edu

Abstract. Accurate quantification of coronary artery calcium provides an opportunity to assess the extent of atherosclerosis disease. Coronary calcification burden has been reported to be associated with cardiovascular risk. Currently, an observer has to identify the coronary calcifications among a set of candidate regions that are obtained by thresholding and connected component labeling. To relieve the observer of such a labor-intensive task, an automated tool is desired that can detect and quantify the coronary calcifications. However, the diverse and heterogeneous nature of the candidate regions poses a significant challenge to the accurate detection of coronary calcifications. In this paper, we investigate a supervised hierarchical classification-based approach to distinguish the coronary calcifications from all the candidate regions. At each level of the hierarchy we learn an ensemble of classifiers where each classifier is a cost-sensitive learner trained on a distinct asymmetrically sampled data subset. Our method attained the accuracy, sensitivity, and specificity of 97.95%, 90.76%, and 98.35%, respectively, on a dataset of electron beam computed tomography scans from 205 subjects.

1 Introduction

Coronary artery calcium (CAC) burden as measured by non-contrast computed tomography (CT) is a significant and independent predictor of the atherosclerosis disease, and is associated with future cardiac events [1]. Therefore, accurate identification and quantification of the CAC may allow diagnosis and monitoring of progression of the atherosclerosis. The calcifications are highly dense regions compared to other soft tissues and, hence, they appear as bright structures in the CT scans. The coronary calcifications are located in the three main coronary arteries and their sub-branches - the left main/left anterior descending artery (LM/LAD), the left circumflex (LCX), and the right coronary artery (RCA) - that cover different portions of the heart surface area. The clinical standard to detect the coronary calcifications is to apply a connected component labeling method using a threshold of 130 Hounsfield units (HU) and a minimum size constraint of four pixels. The thresholding also results in candidate regions from non-coronary calcifications, noise artifacts, and metal implants. Figure 1 shows



Fig. 1. CT image of a heart depicting typical candidate regions from the positive and the negative class - coronary calcifications in LAD (A), RCA (B), aorta (C), and image noise (D,E).

the typical candidate regions for the coronary and the aortic calcifications as well as the image noise. The coronary calcifications are then identified manually from all the candidate regions. However, manual annotation is a labor intensive and time-consuming task, especially for longitudinal studies and large-scale screening. Hence, automated computational methods for detecting the coronary calcification are desired to ease the manual burden as well as to provide means to investigate possible improvements in cardiovascular risk assessment.

Related Work: Surprisingly little work has been performed towards the detection of the coronary calcifications from the non-contrast CT scans. To the best of our knowledge, Ukai *et al.* [2, 3] first proposed a method for coronary calcification detection using some diagnostic rules, and later improved their method by utilizing a neural networks based classification method to discriminate between the coronary calcifications and the artifacts. The method was evaluated on CT scans (acquired in the mass screening for lung cancer) of subjects with very few coronary calcifications and, thus, is limited in scope.

Recently, Isgum *et al.* [4] proposed a two-stage classification method using the k-nearest neighbor classifier for coronary calcification detection. In their method, the candidate regions of size greater than a certain threshold were excluded to reduce the complexity of the problem. The candidate regions with high negative probability in the first stage of classification were discarded and only the remaining ones were considered for the second stage of classification. The second stage was employed to reduce the effect of uneven class priors present due to very small number of coronary calcifications as compared to the rest of the candidate regions. However, the classifiers were trained on the unbalanced data and, hence, were biased towards the majority class. Aorta segmentation was used to characterize the aortic calcifications in order to overcome the complex composition of the negative class. However, the effect of the complex class

composition was not investigated without the aorta segmentation. Moreover, it is desirable to penalize the misclassification of the coronary calcifications more severely than the false positives. This introduces an asymmetry in the learning goals for the two classes which was not explored by the authors.

In this paper, we propose a novel hierarchical classification method to detect coronary calcifications in the non-contrast cardiac CT scans. Our contributions are as follows. First, we utilize a hierarchical tree structure in an attempt to resolve the asymmetry in the class compositions. At the top level, we learn to distinguish the arterial (the coronary and the aortic) calcifications from other highly dense regions present within the heart region. At the second level, we learn to separate the coronary calcifications from the aortic calcifications. We investigate the possibility of such separation without requiring the segmentation of the aorta in this work. Second, for each level of the hierarchy we construct an ensemble of classifiers that are trained on different asymmetrically sampled subsets to overcome the problems of uneven class priors and large dataset. Thirdly, each classifier in the ensemble is designed to be a cost-sensitive learner to deal with the asymmetric learning goals. We also introduce novel meta-features to characterize the coronary calcifications and their neighborhood region for better discrimination.

This paper is structured as follows: In Section 2, we present our proposed hierarchical classification scheme. In Section 3, we present the experimental evaluation of our method and compare the results with other classification schemes. Finally, we conclude in Section 4.

2 Materials & Methods

Data: The heart scans were obtained by electron-beam CT (EBCT) imaging with a slice thickness of 3 *mm* and an x-y pixel spacing of 0.508 - 0.586 *mm*. Scans from 205 subjects with approximately 20-35 image slices per scan were used in our experiments. There were 20 coronary calcifications and 335 negative candidate regions in the heart region per scan on average. We created three mutually exclusive data subsets - S_1 (50 subjects) and S_2 (50 subjects) - for training and validation, respectively, and S_3 (105 subjects) for testing. For training and testing purposes the arterial calcifications were manually annotated.

Feature Extraction: To identify a coronary calcification among the candidate regions, a human observer mostly relies on prior knowledge of the expected location of the coronary arteries relative to the heart. To incorporate the information about the location, we compute the three-dimensional coordinates of the location of the peak HU pixel of the candidate region in a relative coordinate system defined by a unit bounding box around the heart region. The unit heart region bounding box is obtained from the segmented heart region [5]. The observer also uses appearance clues from the candidate region and its surrounding neighboring region to distinguish the coronary calcification from the rest of the candidate regions. Since the coronary arteries mostly span through the pericardial fat af-

ter originating from the ascending aorta, except in the distal section when they enter the ventricular wall, the neighboring regions of the coronary calcifications provide significant clues to distinguish the coronary calcifications from the image noise, which mostly has blood in its neighboring region. Based on these observations, we extracted meta-features or region-features for three regions of interest: the candidate region, its neighborhood region, and both regions combined. The neighborhood region is defined as a ribbon-like region of certain width around the candidate region. Specifically, we compute the mean, standard deviation, skewness, kurtosis, and entropy of pixel level texture features from the region of interest. In our experiments, we use the Laws texture energy measures [6] to compute the pixel features. Other than the above-mentioned features, the partial list of features include: area in mm^2 , shape moments (λ_1 and λ_2), eccentricity, compactness, anisotropy, inertia, and HU density-based region statistics (e.g., mean, maximum, minimum, standard deviation, skewness, kurtosis, and entropy).

Hierarchical Classification Method: In our classification-based approach, the positive class is composed of the coronary calcifications, while the negative class consists of the aortic calcifications, image noise, and metal implants. The majority of the candidate regions belong to the negative class. Moreover, the negative class is broader and richer than the positive class, introducing asymmetry in the class compositions. To account for this asymmetry, we utilize a hierarchical structure for classification of coronary calcifications. At the first level, an ensemble of classifiers is constructed using features selected specifically to discriminate the arterial (coronary and aortic) calcifications from the rest of the candidate regions. At the second level, another ensemble of classifiers is constructed using features selected specifically to separate the coronary calcifications from the aortic calcifications. The final decision is a combination of decisions of the classifiers from the two stages and is given by

$$D(x) = \begin{cases} +1, & \text{if } D^2(x) = +1 \\ -1, & \text{if } D^2(x) = -1, \\ -1, & \text{if } D^1(x) = -1 \end{cases} \quad (1)$$

where D^1 and D^2 are the hard-output decisions of the ensemble of classifiers from the two levels of the hierarchy. Next, we describe the important characteristics of our hierarchical classification approach.

Asymmetric Sampling for Data Selection: At the first level of the hierarchy, the number of coronary and aortic calcifications is comparatively much smaller than the number of other candidate regions. At the second level of the hierarchy, the number of coronary calcifications is higher than the aortic calcifications. Training on such unbalanced data will be biased towards the majority class and it will degrade the performance of the classifier. We address the large dataset problem and the unevenness of the positive and negative classes by employing an asymmetric random sampling strategy. Asymmetric random sampling is performed

by randomly selecting candidates from the majority class until the number of the selected candidates is equal to the number of the minority class candidates.

Ensemble of Classifiers: A single classifier trained on an under-sampled subset assumes that the distribution of candidates in the sampled subset is the same as in the original dataset, which may not be the case in practical situations. Thus, some potentially relevant candidate regions may get eliminated during the sampling process, hampering the performance of the classifier. Use of multiple classifiers trained on differently sampled subsets would improve the accuracy of prediction, and also there would be less possibility of distortion of data distribution. Thus, for each level of the hierarchy, we constructed four asymmetrically-sampled subsets from the training set to train individual classifiers whose decisions were combined to obtain the final decision. We investigated two combination rules - simple majority voting rule (MVR) and weighted majority rule (WMR) - to combine the decisions of the individual classifiers. In the WMR, the weights are directly related to the *competency* or accuracy of the classifiers, and are computed as the logarithm of odds of *competency*, ($w_i = \log(\frac{A_i}{1-A_i})$, where A_i is the prior probability for correct classification, computed from the validation set).

Asymmetric Cost for Misclassification: Failing to detect coronary calcifications may cause a serious atherosclerotic condition go undiagnosed, leading to further complications with the subject's health, whereas false detections may lead to further, more expensive and intrusive examinations, which may ultimately discover the correct diagnosis. This asymmetry in the learning goals of the positive and negative classes demands cost-sensitive learning algorithms. The support vector machines (SVMs) are capable of incorporating different costs for the positive and the negative classes by modifying its objective function as follows:

$$\frac{1}{2}w^T w + C_p \sum_{i=1}^{k-1} \xi_i + C_n \sum_{i=k}^n \xi_i, \quad (2)$$

where C_p and C_n are the cost parameters for the positive and the negative classes, respectively [7]. However, the specific costs for this problem are not easy to determine. Hence, we employ a greedy search algorithm in which the classifiers determine the optimal costs using the 3-fold cross-validation method. For each value of C_p , we vary the ratio $w_C = C_p/C_n$ for a range of values above 0.5 to favor high detection rate.

Feature Selection: The classification accuracy of a classifier depends largely on the selection of relevant features and removal of non-redundant features from a large set. The relevance of a feature with respect to a particular outcome or the redundancy between any two features can be characterized in terms of correlation or mutual information. We used a mutual information (*MI*)-based *minimum-redundancy-maximum-relevance* (mRMR) feature selection heuristic proposed by Peng *et al.* [8]. The feature selection is performed in two steps. First, a subset \mathbf{F}^1 of N features is selected from the large feature set \mathbf{F}^o such

that an m^{th} feature is added incrementally to the currently selected set \mathbf{F}_{m-1}^1 with $m - 1$ features, if it maximizes the following condition:

$$\max_{f_i \in \mathbf{F}_{m-1}^{1*}} \left[MI(f_i, L) - \frac{1}{m-1} \sum_{f_j \in \mathbf{F}_{m-1}^1} MI(f_i, f_j) \right], \quad (3)$$

where the first term corresponds to the relevance, the second term corresponds to the redundancy, \mathbf{F}_{m-1}^{1*} is the set $\{\mathbf{F}^o - \mathbf{F}_{m-1}^1\}$, L is the target class, and f_k is the k^{th} feature. In the second step, we form P sequential feature subsets in multiples of k features such that $\mathbf{F}_{1*k}^1 \subset \mathbf{F}_{2*k}^1 \subset \dots \subset \mathbf{F}_{p*k}^1$ and select the feature subset \mathbf{F} that corresponds to the minimum classification error using the SVM.

Classification Algorithms: We refer to our proposed hierarchical classification method that utilizes an ensemble of SVMs combined using either MVR or WMR at each hierarchy level as HEC. The individual SVMs in this method were trained with and without the asymmetric costs (AC) separately. Moreover, we constructed two additional hierarchical classifiers that used only a single SVM at each stage of the hierarchy. We refer to these hierarchical single SVM-based classifiers as HSC. To compare with non-hierarchical methods, we also constructed a single SVM classifier and an ensemble of SVMs, referred to as SSC and SEC, respectively, that were trained to identify coronary calcifications in a single stage.

We extracted three different feature subsets that provided the highest average cross validation accuracy - two sets of 30 and 80 features for the first and second level of the hierarchy, respectively, and one set of 120 features for the single level classification method. We observed that the location features were always selected, confirming the idea that the location of the candidate regions with respect to a heart-centered coordinate system plays a significant role in the identification of coronary calcifications. We expected the shape and size features to be relevant because of the tubular structure of the coronary arteries, however, these feature never got selected, signifying that shape and size are not the discriminating characteristics of coronary calcifications.

3 Results and Discussion

In our experiments, we used LIBSVM [9] to train the SVMs with the gaussian radial basis kernel function. The width parameter γ , the penalty cost parameter C , and the ratio of asymmetric misclassification cost C_p/C_n were optimized using a grid search technique in the 3-fold cross-validation method. The performance of the classification methods was evaluated using accuracy (ACC) and F-measure (F_1). The F-measure combines precision and recall to provide a single metric for performance evaluation. Table 1 reports the overall performance of the selected classifiers on the unseen test dataset. It can be observed that the proposed hierarchical classification method, HEC-MVR-AC, provided the highest accuracy of 97.95%. The highest precision of 75.48%, the highest F-measure of 82.42%, and the lowest misclassification error of 767 candidate regions further demonstrate

Table 1. Performance evaluation of selected classifiers. The initials are defined as follows: SSC (single stage classifier), SEC (single stage ensemble of classifiers), HSC (hierarchical classification method with single classifier at each level), HEC (hierarchical classification method with ensemble of classifiers at each level), AC (asymmetric cost), MVR (majority voting rule), WMR (weighted majority rule), TPR (true positive rate), TNR (true negative rate), ACC (accuracy), P (precision), F_1 (F-measure), FP (false positives), and FN (false negatives).

| Method | TPR (%) | TNR (%) | ACC (%) | P (%) | F_1 (%) | FP+FN |
|------------|---------|---------|--------------|--------------|--------------|-------|
| SSC | 91.97 | 97.79 | 97.48 | 69.89 | 79.42 | 944 |
| SEC-MVR | 91.37 | 98.09 | 97.73 | 72.78 | 81.02 | 848 |
| SEC-WMR | 91.92 | 97.80 | 97.49 | 69.98 | 79.47 | 941 |
| HSC | 91.72 | 97.83 | 97.51 | 70.26 | 79.57 | 933 |
| HEC-MVR | 90.71 | 98.33 | 97.92 | 75.19 | 82.22 | 777 |
| HEC-WMR | 91.77 | 98.09 | 97.75 | 72.84 | 81.22 | 841 |
| HEC-MVR-AC | 90.76 | 98.35 | 97.95 | 75.48 | 82.42 | 767 |

the strength of the proposed method. It missed 1.74 coronary calcifications at the expense of 5.56 false candidates per scan on average.

Table 2 presents the number and the percentage of the candidate regions that were misclassified by the proposed method for different regions/categories. The category-wise misclassification error percentage was computed as the ratio of the number of misclassified candidate regions in a particular category to the total number of candidate regions in that category. It can be observed that, though most of the errors were from the noise artifacts among the false positives, the error percentage of the ascending aorta candidates was the highest. Likewise, the number of errors from the right coronary artery were highest among the false negatives but the error percentage of the left main calcifications was the highest. The location of the ascending aorta calcifications among different subjects overlaps significantly with the left main and the proximal region of the right coronary artery leading to such high error percentages. Further investigation is required in to the design of informative features to discriminate between the ascending aorta calcifications and the coronary calcifications near the ostia.

4 Conclusion and Future Work

In this paper, we have demonstrated that using a hierarchical classification method, and combining the decisions of multiple classifiers improved the detection of the coronary calcifications over a single classifier. At the top level of the hierarchy, the method discriminates between the arterial (the coronary and the aortic) calcifications and other highly dense regions present within the heart region. At the second level, the method distinguishes the coronary calcifications from the aortic calcifications without requiring explicit segmentation of the aorta. Multiple classifiers are trained on different asymmetrically sampled data subsets for each stage of the hierarchy and their decisions are combined to overcome the problem imbalanced dataset and to improve the prediction accuracy. Each classifier is trained using different penalty costs for the positive and the negative classes to accommodate asymmetric learning goals. The proposed

Table 2. The number and percentage (%) of the candidate regions misclassified by the HEC-MVR-AC method on the unseen test data subset. The initials are defined as follows: N (noise artifacts), AA (ascending aorta), DA (descending aorta), LM (left main), LAD (left anterior descending), LCX (left circumflex), and RCA (right coronary artery).

| N | AA | DA | LM | LAD | LCX | RCA |
|-------|--------|-------|--------|-------|--------|-------|
| 542 | 40 | 2 | 43 | 24 | 40 | 76 |
| 1.56% | 13.94% | 0.50% | 46.24% | 3.38% | 11.63% | 9.12% |

method provided encouraging preliminary results, and it has opened multiple avenues for future research to achieve the final goal of improving cardiovascular risk assessment. Development of a more compact frame of reference using a local heart-centered coordinate system, aligned in terms of translation, scale, and rotation, could further improve the accuracy of the method.

References

1. Taylor, A., Bindeman, J., Feuerstein, I., Cao, F., Brazaitis, M., O'Malley, P.: Coronary calcium independently predicts incident premature coronary heart disease over measured cardiovascular risk factors: mean three-year outcomes in the prospective army coronary calcium (PACC) project. *Journal of the American College of Cardiology* **46**(5) (2005) 807–14
2. Ukai, Y., Niki, N., Satoh, H., Watanabe, S., Ohmatsu, H., Eguchi, K., Moriyama, N.: An algorithm for coronary calcification diagnosis based on helical CT images. In: Proc. International Conference on Pattern Recognition. Volume 3., Washington, DC, USA, IEEE Computer Society (Aug. 1996) 543–547
3. Ukai, Y., Niki, N., Satoh, H., Watanabe, S., Ohmatsu, H., Eguchi, K., Moriyama, N.: A coronary calcification diagnosis system based on helical CT images. *IEEE Trans. on Nuclear Science* **45**(6) (Dec 1998) 3083–3088
4. Isgum, I., Rutten, A., Prokop, M., van Ginneken, B.: Detection of coronary calcifications from computed tomography scans for automated risk assessment of coronary artery disease. *Medical Physics* **34**(4) (2007) 1450–61
5. Kurkure, U.: Computational Methods for Non-Invasive Cardiovascular Image Analysis. PhD thesis, University of Houston, Houston, TX (May 2008)
6. Laws, K.: Textured Image Segmentation. PhD thesis, University of Southern California, Los Angeles, CA (1980)
7. Osuna, E., Freund, R., Girosi, F.: Support vector machines: Training and applications. Technical Report AIM-1602 (1997)
8. Peng, H., Long, F., Ding, C.: Feature selection based on mutual information: Criteria of max-dependency, max-relevance, and min-redundancy. *IEEE Trans. on Pattern Analysis Machine Intelligence* **27**(8) (2005) 1226–1238
9. Chang, C., Lin, C.: LIBSVM: a library for support vector machines. (2001) Software available at <http://www.csie.ntu.edu.tw/~cjlin/libsvm>.

An Alternative Approach to Spectrum-Based Atherosclerotic Plaque Characterization Techniques Using Intravascular Ultrasound (IVUS) Backscattered Signals

Amin Katouzian¹, Babak Baseri¹, Elisa E. Konofagou^{1,2}, and Andrew F. Laine^{1,2}

¹ Biomedical and ² Radiology Departments, Columbia University, NY USA
{ak2432,laine}@columbia.edu

Abstract. In this paper, the discrete wavelet packet frames are used to delineate the atherosclerotic plaque components using intravascular ultrasound (IVUS) backscattered signals. The frames are classified in an unsupervised fashion deploying K-means clustering technique and the generated prognosis histology (PH) images are quantified using relative histology images. While existing tissue characterization algorithms fail to differentiate between blood and plaque signals, the proposed algorithm can be used to estimate the lumen border at higher levels of wavelet expansion. We will demonstrate the in-vitro and in-vivo tissue characterization as well as lumen border detection results employing 40 MHz rotating unfocused single-element transducers. It is concluded that our two dimensional (2-D) algorithm, which is independent of the cardiac and catheter motions, performs well in both in-vivo and in-vitro cases.

Keywords: Wavelet Packets, Atherosclerotic Plaque Characterization, Intravascular Ultrasound (IVUS).

1 Introduction

Cardiac catheterization supplemented with IVUS is often used in routine interventional procedures to investigate the sides of stenosis throughout the artery in addition to angiogram. The IVUS not only provides the 2-D gray scale cross sectional images of the arterial wall and atherosclerosis but also its radiofrequency (RF) signals can be further processed to characterize the plaque constitutes. The ultimate goal of such characterization is: 1) to detect the vulnerable plaques, 2) to study the progression or regression of the plaques subject to treatment approach. Although there are different definitions for plaque vulnerability by different histopathologists, we will justify our results with the one introduced in [1].

Real time acquisition, sufficient signal penetration and low cost image formation and acquisition techniques/instruments make IVUS superior to other imaging modalities to date. Accordingly, researchers have developed IVUS-based algorithms using different techniques such as elastography [2], integrated backscatter (IB) coefficients [3] and spectral analysis [4]. The later has been implemented in the

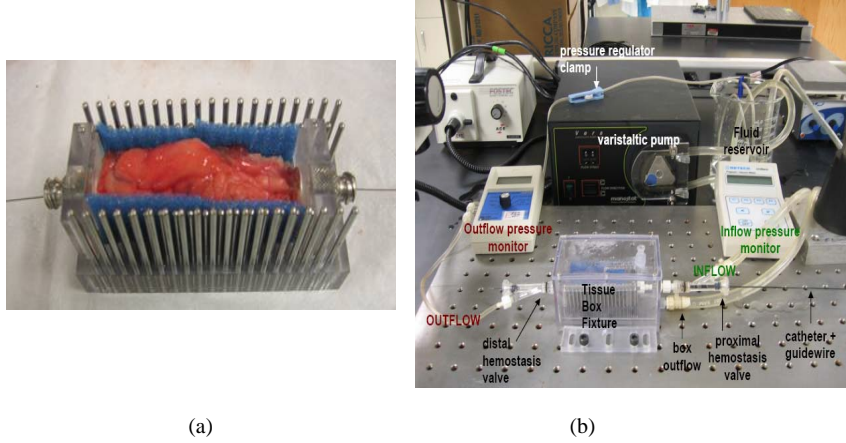


Fig.1. Tissue cage fixture (a), experiment setup (b).

VOLCANO (Rancho Cordova, CA) IVUS clinical scanners using 20 MHz 64 elements phased array transducers. It has been shown that the variability among extracted spectral features using 8-features algorithm and transducer's spectral parameters (bandwidth, center frequency) make the classification challenging [5].

This motivated us to develop a texture-based algorithm using discrete wavelet packet frame (DWPF) and 2-D envelope detection method based on the work by authors in [6]. The extracted textural features are perfectly suited for classification and capture characteristics of the plaque with the highest correlation to histology. This would resolve one of the main current limitations of IVUS, which is discrimination between fibrotic and lipidic tissues [7].

2 In-vitro Data Collection

We collected the hearts from two sources; autopsy and transplant surgery, within 24 hours postmortem. The arteries were dissected from the hearts with approximate size of $20-60 \times 20 \times 20 \text{ mm}^2$ ($l \times w \times h$). We tied off the major branches, attached the endplates to the distal and proximal ends, and placed the segment into a tissue cage fixture, Fig. 1(a). Circulating phosphate buffered saline (PBS) was used to ensure constant pressure (100 mmHg) as well as flow and to maintain the artery physiologically open at 37° Celsius, Fig. 1(b). The 40 MHz Atlantis Boston Scientific (Fremont, CA) IVUS catheter was introduced and advanced on a 0.014" guide wire and a complete automatic pullback was performed from the distal to proximal side. The RF data was collected using two 12-bit Acqiris boards (Monroe, NY) and digitized at periodic time intervals, $T_s = 2.5 \text{ ns}$ ($f_s = 400 \text{ MHz}$). The catheter pullback speed and the frame rate were set to 0.5 mm/s and 30 frames/s, respectively. After imaging, the artery was pressure fixed with 10% buffered formaldehyde under 100

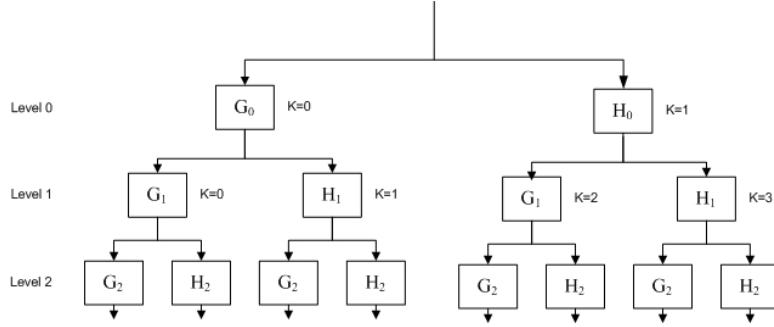


Fig. 2. Tree structure for discrete wavelet packet frames (DWPF) and associate indexes.

mmHg for three hours followed by decalcification. The histology blocks were sectioned from distal to proximal every 2mm (corresponding to 120 frames of the IVUS pullback) using the side rods. Blocks were then embedded in paraffin. For each block, three sections were used for histology. The first two sections were stained with hematoxylin and eosin (H&E) and Movat Pentachrome, and the last section was kept unstained for future necessary staining (e.g., Sirius Red).

3 Methods

Discrete wavelet packet transform (DWPT) [8] is the over complete version of the decomposition process in the discrete wavelet transform (DWT) [9-10], in which every generated coefficient in the decomposition tree is passed through high-pass and low-pass filters. The cost of such a generalization is an increased in computational complexity. Unlike the DWT and DWPT, the decompositions are translation invariant in DWPF and no decimation occurs between levels (Fig. 2). This makes the DWPF superior in algorithms used for texture segmentation. Since the IVUS signals are sampled at the rate of f_s , it is more appropriate to consider the discrete signals that can be represented by a set of wavelets packet coefficients at the first level ($l=0$).

For the tree-structured scheme demonstrated in Fig. 2, we can write:

$$S_{2k}^{l+1}(\omega) = G_l(\omega)S_k^l(\omega), S_{2k+1}^{l+1}(\omega) = H_l(\omega)S_k^l(\omega) \quad (1)$$

where ω represents the radian frequency and $S_k^l(\omega)$ is the Fourier transform of the frame coefficients at channel k and level l .

3.1 Filter Bank Specification

The high-pass $G_l(\omega)$ and low-pass $H_l(\omega)$ filters at level l , as described in [8], can be written as follows:

$$H_l(\omega) = H_0(2^l \omega), G_l(\omega) = G_0(2^l \omega) \quad (2)$$

Consequently, the multi-channel wavelet schematic in Fig. 2 behaves like a filter bank with channel filters:

$$\{F_k^l(\omega) | 0 \leq k \leq 2^l - 1\} \quad (3)$$

where $F_k^l(\omega)$ can be derived recursively as follows:

$$F_0^0(\omega) = G_0(\omega), F_1^0(\omega) = H_0(\omega) \quad (4)$$

$$F_{2k}^{l+1}(\omega) = G_{l+1}(\omega) F_k^l(\omega) = G_0(2^{l+1} \omega) F_k^l \quad (5)$$

$$F_{2k+1}^{l+1}(\omega) = H_{l+1}(\omega) F_k^l(\omega) = H_0(2^{l+1} \omega) F_k^l \quad (6)$$

It has been shown that the selection of the filters $G_0(\omega)$ and $H_0(\omega)$ can have significant impact on the texture classification performance [6]. The filter candidates must satisfy crucial criteria such as symmetry as well as boundary accuracy and have optimal frequency response. Hence, we selected Lemarie-Battle [10] wavelets, that are symmetric (have linear phase response) and quadrature mirror filters (QMF). The former property alleviates boundary effects through simple methods of mirror extension. The wavelets using QMF, as well as constructed filter bank $F_k^l(\omega)$ cover exactly the frequency domain and satisfy the property:

$$|G_0(\omega)|^2 + |H_0(\omega)|^2 = |G_0(\omega)| + |H_0(\omega)| = 1 \quad (7)$$

$$\sum_{k=0}^{2^l-1} |F_k^l(\omega)|^2 = \sum_{k=0}^{2^l-1} |F_k^l(\omega)| = 1 \quad (8)$$

3.2 Feature Extraction

The features were extracted by processing the IVUS signals for every frame in (r, θ) domain. Each frame contains 256 lines that span 360 degree with 2048 samples per line. In order to have an optimized frame size in respect to the computational complexity and the textural resolution, we interpolated (spline) and decimated the signals in the lateral and axial directions by factor of 2 and 4, respectively to generate

the square $M=512$ pixels frame. For each IVUS frame, a tensor product extension was used in which the channel filters were denoted by $F_{i \times j}^l(\omega_r, \omega_\theta) = F_i^l(\omega_r)F_j^l(\omega_\theta)$. Consequently, such an extension will lead to the orientation selectivity in the decomposition tree. Four possible orientations can be considered excluding the root node, which is omnidirectional:

1. The node last filtered by $G_l(\omega_r)H_l(\omega_\theta)$ corresponds to the vertical orientation. The highpass filter G_l and lowpass filter H_l are applied in the axial and lateral directions, respectively.
2. The node last filtered by $H_l(\omega_r)G_l(\omega_\theta)$ corresponds to the horizontal orientation. The lowpass filter H_l and highpass filter G_l are applied in the axial and lateral directions, respectively.
3. The node last filtered by $G_l(\omega_r)G_l(\omega_\theta)$ corresponds to the diagonal orientation. The highpass filter G_l is applied in the axial and lateral directions, respectively.
4. The node last filtered by $H_l(\omega_r)H_l(\omega_\theta)$ has the same orientation as its parent. The lowpass filter H_l is applied in the axial and lateral directions, respectively.

Finally, the envelope of the signals was computed and the feature matrix was constructed as follows:

$$\vec{V}_{i,j} = \{e_{k,i,j}^l \mid 0 \leq k \leq (2^{l-1}), i, j = 1, \dots, M\} \quad (9)$$

where $e_{k,i,j}^l$ represents the envelope value of pixel (i, j) for the k -th components at level l .

3.3 Classification

The overall justification of in-vivo real-time plaque characterization is performed by the interventional cardiologists through the use of classified tissues. For this reason, we chose the k-means clustering algorithm in order to classify the extracted features and generate the prognosis histology (PH) images. We utilized the unsupervised classifier to quantify the reliability of the extracted signatures. Our hypothesis is that if the classification results (PH images) driven by the unsupervised signatures preserve their high correlation with the histology images used here as ground truth, then the features can be used reliably in the training data set for supervised classification. We have categorized plaque components into four classes ($N_c = 4$) i.e., lipidic, fibrotic, calcified and background (no tissue).

For every representation matrix $X_{M \times M}$ a label was assigned to each pixel by modulo N_c . We computed the center of clusters $\{\bar{C}_\kappa \mid 0 \leq \kappa \leq N_c - 1\}$ by calculating the mean vector for each class. The pixel $\{x_{i,j} \mid i, j = 1, \dots, M\}$ was assigned to the class κ if the Euclidean distance between the corresponding pixel and the class center

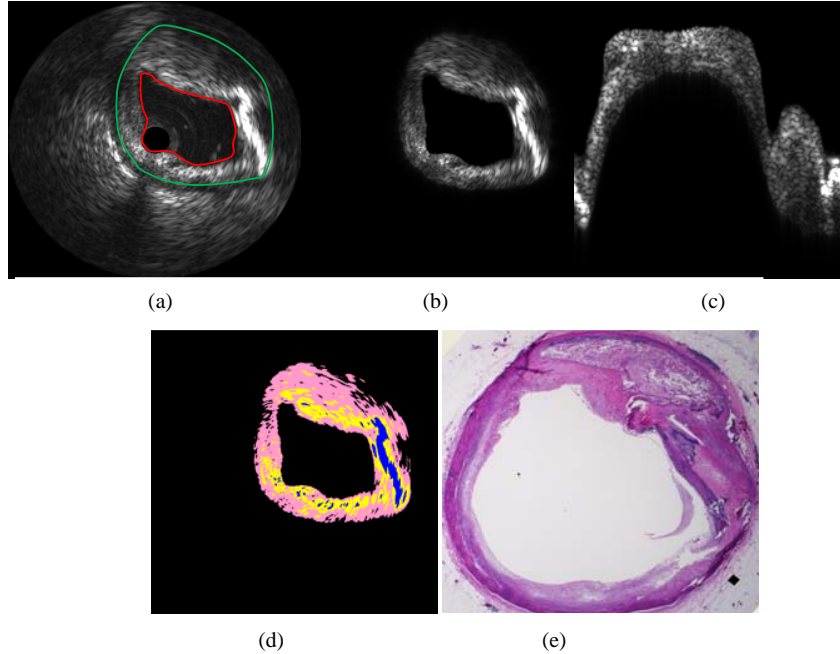


Fig. 3. IVUS image with manually traced vessel wall (green) and lumen (red) borders (a), segmented plaque in Cartesian coordinates (b), segmented plaque in (r, θ) coordinates (c), generated PH image (pink, yellow and blue represent lipidic, fibrotic and calcified components, respectively) (d), Movat Pentachrome histology image (e)

\bar{C}_κ was the closest. The centers of the clusters were updated in an iterative fashion by recomputing the relative mean vectors. The procedure was terminated once no change in labeling occurred.

4 Experimental Results and Quantification

Sixty four cross-sections of interest (CSI) collected from 32 cadaver hearts, including 26 left anterior descending (LAD), 28 right coronary artery (RCA) and 20 left circumflex (LCX) segments that had more than 30% stenosis. As we mentioned in the preceding section, we decimated the signals and used spline interpolation to generate 512-by-512 scan converted (Cartesian domain) B-mode images. For each frame, an expert manually segmented the plaque by tracing the vessel wall and lumen borders, Fig. 3(a). The corresponding plaque signals were read and saved in a matrix with the same size of IVUS image in the (r, θ) domain, Fig. 3(c).

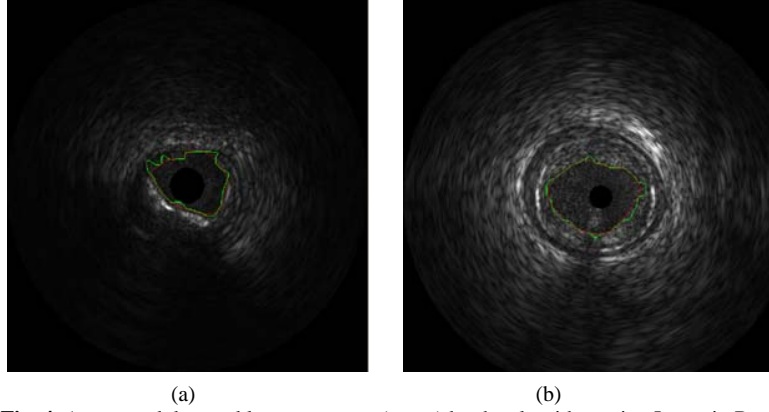
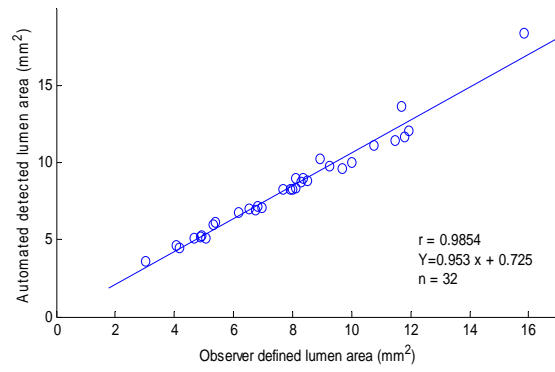


Fig. 4. Automated detected lumen contour (green) by the algorithm using Lemarie-Battle filters of order 18, expansion level $L=4$, number of classes $N_c=2$ and manually traced contour (red) by and expert. In-vivo (a), In-vitro using circulating human blood (b)

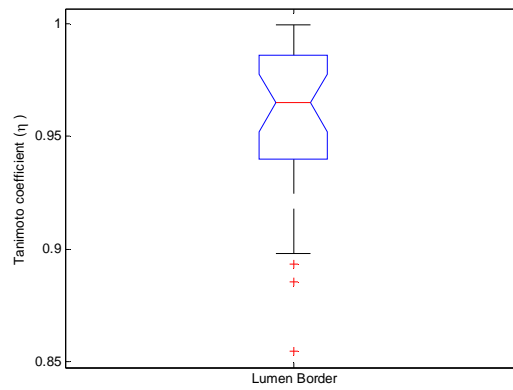
We performed our algorithm on 512-by-512 matrices and selected Lemarie-Battle filters of order 18, decomposition level $L = 2$ and number of classes $N_c = 4$. Finally, the resulting classified images were mapped onto Cartesian plane, Fig. 3(d). Fig. 3 demonstrates a CSI, corresponding Movat Pentachrome histology image, and the PH image. The blue, yellow and pink colors exhibit calcified, fibrotic, and lipidic plaque components, respectively. Two independent histopathologists evaluated the results contrasting the histology images corresponding to the PH images. The accuracy of classified tissues was found to be 81.71%, 82.76% and 85.51% for fibrotic, lipidic and calcified components, respectively. The accuracy of IVUS-VH technique using autoregressive (AR) analysis in combination with a classification tree for 30 MHz single element transducers has been reported to be 90.4%, 92.8%, 90.9% and 89.5% for the training data set and 79.7%, 81.2%, 92.8% and 85.5% for the test dataset in fibrotic, fibro-lipidic, calcified and calcified necrotic regions, respectively.

As we mentioned in Section 1, none of the existing algorithms is capable of characterizing the atherosclerotic tissues and differentiate between blood and plaque signals (estimate the lumen border). We evaluated the algorithm performance on lumen border estimation using 18 in-vivo CSI collected from three patients and 14 in-vitro CSI collected from two cadaver hearts. Fig. 4 demonstrates the automatic detected lumen contours (green) and the manually traced contours (red) by an expert for both cases. Our results show that the manual and automated detected lumen borders are correlated very well ($r = 0.9854$, $y = 0.953x + 0.725$), Fig. 5(a). We also computed the Tanimoto coefficient (η), Fig. 5(b), to measure how well the automated detected contour is matched with corresponding manually traced contour:

$$\eta = \frac{N_c^{contour}}{N_a^{contour} + N_m^{contour} - N_c^{contour}} \quad (10)$$



(a)



(b)

Fig. 5. Comparison of automated detected lumen area and expert-defined lumen area (a), Box-Whisker plot of Tanimoto coefficients of lumen border.

5 Summary and Conclusion

In this paper, we presented a reliable two 2-D texture-derived atherosclerotic tissue characterization algorithm as an alternative to spectrum-based approaches like IV-VH, IB-IVUS and full-spectrum analysis. We processed the IVUS signals for each frame and extracted the textural features by using multi-channel wavelet packet analysis. The wavelet packet signatures were classified in an unsupervised fashion using K-means clustering algorithm.

The main advantage of the proposed algorithm is that it can reliably classify tissues regardless of the transducer center frequency or spectrum while inconsistency among the spectrum-derived features within the transducer's bandwidth still remains a major challenge. However, we were not able to detect the necrotic core components directly. Although both necrotic core tissues and lipid-rich pools have been recognized as markers for detection of vulnerable plaques, it is an advantage to have a classification algorithm that is able to detect the necrotic core in addition to fibrotic, lipidic and calcified tissues. In the future, we will attempt to extend the algorithm to supervised classification on raw IVUS backscattered signals and investigate this issue.

We will focus on two important aspects in future studies. First, the effects of blood on generated PH images and classification performance will be considered. In fact, it is an inevitable step to validate the reliability of the in-vitro trained classifier for in-vivo atherosclerotic plaque characterization. Secondly, the feasibility of tissue classification within the regions of acoustic shadowing behind calcification will be tested. It has been reported that the tissue characterization in these regions remains difficult [11]. Our hypothesis was that sufficient spectral features would not exist due to signal attenuation in the densely calcified regions. This can be investigated through our proposed technique, since the background (no tissue) had been considered as one of the classes. We will test the tissue characterization and lumen border detection performance using mechanically rotating single-element 40 MHz Atlantis Boston scientific and 45 MHz Revolution Volcano catheters in future studies.

Acknowledgement

We wish to express our sincere appreciations to Dr. Stephane Carlier for his invaluable support. We thank Boston Scientific Corporation (Fremont, CA) for providing us the 40 MHz acquisition system. We also thank Jennifer Lisauskas and Dr. Stephen Sum, at InfraRedx (Burlington, MA), who developed the artery fixation cage and their help in collecting IVUS data is acknowledged. The histology samples were processed at CVPPath (Gaithersburg, MD) under supervision of Dr. R. Virmani.

References

1. Virmani, R., Burke, A. P., Kolodgie, F. D., Farb, A.: Pathology of the thin-cap fibroatheroma: A type of vulnerable plaque. *J. Interven. Cardiol.*, vol. 16, No. 3, pp. 267-272 (2003)
2. Korte, C. L., van der Steen, A. F. W., Cespedes, E. I., Pasterkamp, G., Carlier, S. G., Mastik, F., Schoneveld, A. H., Serruys, P. W., Bom, N.: Characterization of plaque components and vulnerability with intravascular ultrasound elastography. *Physics in Med. & Biol.* vol. 45, pp. 1465-1475 (2000)
3. Kawasaki, M., Takatsu, H., Noda, T., Sano, K., Ito, Y., Hayakawa, K., Tsuchiya, K., Arai, M., Nishigaki, K., Takemura, G., Minatoguchi, S., Fujiwara, T., Fujiwara, H.: In Vivo Quantitative Tissue Characterization of Human Coronary Arterial Plaques by Use of Integrated Backscatter Intravascular Ultrasound and Comparison With Angioscopic Findings. *Circulation*, pp. 2487- 2492, May (2002)

4. Nair, A., Kuban, B. D., Obuchowski, N., Vince, D. G.: Assessing spectral algorithms to predict atherosclerotic plaque composition with normalized and raw intravascular ultrasound data. *Ultrasound in Med. & Biol.*, vol. 27, no. 10, pp. 1319–1331 (2001)
5. Katouzian, A., Sathyanarayana, S., Baseri, B., Konofagou, E. E., Carlier, S. G.: Challenges in Atherosclerotic Plaque Characterization with Intravascular Ultrasound (IVUS): From Data Collection to Classification. *IEEE Trans. on Information Technology in Biomedicine*, vol. 12, no. 3, pp. 315-327 (2008)
6. Laine, A. F., Fan, F.: Frame representation for texture segmentation. *IEEE Trans. Image Proc.*, vol. 5, no. 5, pp. 771-780 (1996)
7. Hiro, T., Leung, C. Y., De Guzman, S., Caiozzo, V. J., Fervid, A. R., Karimi, H., Helfant, R. H., Tobis, J. M.: Are soft echoes really soft? Intravascular ultrasound assessment of mechanical properties in human atherosclerotic tissue. *American Heart J.* vol. 133, pp. 1-7 (1997)
8. Coifman, R.R., Wickerhauser, M.V.: Entropy-based algorithms for best basis selection. *IEEE Trans. Inform. Theory*, pt. II, vol. 38, no. 2, pp. 713-718, Mar. (1992)
9. Rioul, O.: A discrete-time multiresolution theory. *IEEE Trans. Sig. Proc.*, vol. 41, no. 8, pp. 2591-2606, Aug. (1993)
10. Mallat, S.G.: A theory of multiresolution signal decomposition: The wavelet representation. *IEEE Trans. Patt. Anal. Mach. Intell.*, vol. 11, no. 7, pp. 674-693 (1989)
11. Tanaka, K., Carlier, S. G., Katouzian, A., Mintz, G.: Characterization of the intravascular ultrasound radiofrequency signal within regions of acoustic shadowing behind calcium. *J. Am. Coll. Cardiol.*, vol. 49, no. 9, Suppl. B, 29B (2007)

Growth Pattern of Atherosclerotic Calcifications

Lene Lillemark Larsen^{1,2}, Melanie Ganz^{1,2}, Erik B. Dam², Naga P. K. R. Dandu^{1,2}, and Mads Nielsen^{1,2}

¹ Department for Computer Science, Copenhagen University, Denmark
lene@diiku.dk

² Nordic Bioscience, Herlev, Denmark

Abstract. We present a novel method to analyze the growth of abdominal atherosclerotic plaques based on x-ray projections. The growth analysis can aid progression monitoring in clinical trials and in population screening programs. Our results are based on a longitudinal study over 8.5 years. The annotations of the calcifications are matched longitudinally using thin plate spline registration and area overlap calculations. The growth of the calcifications is measured by the distribution of the geometry statistics of the calcifications. The method was evaluated on 135 subjects with a total number of 611 calcifications. Our results show, for instance longitudinal growth of calcifications with a mean of 2.53 mm (± 1.95) in the blood flow direction and correlations with pathologically related biomarkers.

1 Introduction

Atherosclerosis is a primary cardiovascular disease (CVD), that is the main cause of the disease burden (illness and death) in Europe. The cost of CVD is estimated to 192 billion euro per year spread out on direct health care, productivity losses and informal health care [1]. Atherosclerosis is a chronic inflammatory process that builds up plaque in the intimal wall of the arteries. Atherosclerosis starts in the childhood and progresses during adolescence as development of fatty streaks, that evolves to fibrous caps and lastly formation of calcifications, which could lead to ruptures possibly resulting in strokes and heart attacks. Calcifications are widely used as a clinical indicator of atherosclerosis [2, 3].

X-ray imaging is an attractive image modality for quantification of calcifications that can aid in large scale clinical trials and screening programs due to the low cost, fast examination and non-invasiveness. Other image modalities such as intravascular ultrasound, computed tomography and magnetic resonance imaging have also been used for studies of the atherosclerotic growth [4–6], but to a smaller extent due to the cost and the patient discomfort. Available x-ray data already exist from clinical trials and routine screening for osteoporosis, which can be used for identifying the growth pattern of calcifications.

Our hypothesis is that the growth patterns are good estimators of the progression of atherosclerosis. The gold standard severity score for atherosclerotic calcifications is the AC24 score introduced by the Framingham group. AC24 is

quantifying the amount of calcification only as the amount along the arterial wall [7, 8]. To our knowledge this is the first study that characterizes the growth patterns of atherosclerotic calcifications from x-ray projections. Our region of interest is the lumbar region denoted by L1-L4. The amount of calcified deposit in L1-L4 can be an indicator of the risk of future cardiovascular events [9]. The annotations of the calcifications are registered by thin plate spline registration and then a suitable match is found using area overlap. Now we extract information of the individual calcifications about the growth patterns.

In this work we have used manual annotations of the images by radiologists, but an automated segmentation method [9] could be used instead, which would be cost-saving and minimize the degree of subjectivity.

In the next section we describe our dataset and then we give a brief overview of the thin plate spline algorithm and a description of our registration and matching process. We then describe the statistical geometry used to characterize the growth patterns. Finally we present our results and we discuss the validity of the method used in respect to well-known biomarkers of the pathology.

2 The Dataset

The dataset consists of 135 women with mean age 62.4 (± 7.0) and mean BMI 24.3 (± 4.0) at the initial scanning. The patients in our dataset had x-ray images taken twice, once in 1992 (baseline) and again in 2000/2001 (follow-up) as part of an osteoporosis study. The images are lateral x-ray projections, which were digitalized with a Vidar DosimetryPro Advantage scanner with a pixel size of $44.6 \times 44.6 \mu$. The images were scanned at the Center for Clinical and Basic Research (CCBR) in Copenhagen. The annotations of the images were done by three trained radiologists from CCBR. The annotations include six points of each vertebrae L1-L4, the posterior and anterior aorta wall and the calcified deposits, that were included if a dense area was visible in an area parallel to the lumbar spine; an example can be seen in Fig. 1. From the dataset 103 patients had baseline calcifications with an average of 4.8 (± 8.1) calcifications.

3 The Registration

The position in the scanner and the anatomy of the patients have changed in between the x-ray images. The calibration of the scanner also differs. This causes a significant variability in the position of the vertebrae and the aorta. Due to these combined variabilities image registration is needed to be able to extract the biological information about the growth of the calcifications. The registration is used to align the aorta and thereby the calcifications in the follow-up image to the baseline image. We use thin plate splines (TPS) for the registration [10]. Thin plate splines form a class of non-rigid mapping functions that are globally smooth. This makes them desirable for registering the deformable aorta and thereby the calcifications. We want to make predictive growth patterns from the baseline information by use of the follow-up information. TPS is non-symmetric

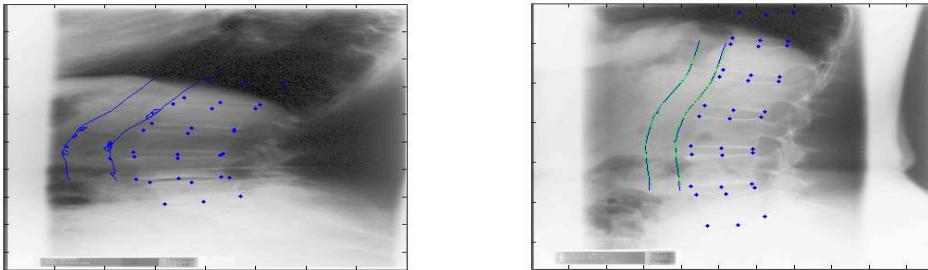


Fig. 1. The follow-up image (right) and the baseline image (left), where the aorta from the follow-up is registered to the baseline aorta. Blue are the original annotations of the structures and green are the registered annotations of the follow-up aorta on the baseline. Note that the registered follow-up aorta is well aligned with the baseline aorta.

in source and destination, so we need to register from follow-up to baseline, see Fig. 1. TPS map the corresponding set of landmarks so they minimize the bending energy. The landmarks we have used are the intersections between the line through the vertebrae annotations and the anterior/posterior aorta wall. Since the alignment in the registration could bias the analysis of the position and growth of the calcifications, the calcifications are unsuitable as landmarks. The mapping function f for the follow-up annotations $(x, y) \in \mathbb{R}^2$ is given by

$$f(x, y) = a_1 + a_x x + a_y y + \sum_{i=1}^N w_i U(\|(x_i, y_i) - (x, y)\|), \quad (1)$$

where (x_i, y_i) are the landmarks from baseline and $r = \|(x_i, y_i) - (x, y)\|$ is the Euclidean distance. $a_1 + a_x + a_y$ are affine motion coefficients, w_i are the weights for the combination of the distance measurements for the correspondence points and the thin plate splines. $U(r) = r^2 \log(r^2)$ is the radial basis function.

4 Matching

After the follow-up image is warped into the baseline image, we need to find the matching of individual calcification from the pair of images. We have matched the calcifications based on area overlap AO between the baseline and follow-up.

$$AO = \frac{|A_{baseline} \cap A_{follow-up}|}{|A_{baseline} \cup A_{follow-up}|} \quad (2)$$

The area overlap is a suitable method for matching, because it captures the matching calcifications without any assumptions of a certain shape of the calcifications. Alternatively we could have matched using nearest center of mass calculations. This method would need a threshold for the maximum distance

allowed between the possibly matching center of masses, which could bias the result. Ongoing research have not yet clarified how the calcifications emerge, grow together, rupture or get reabsorbed. Due to lack of knowledge of the behavior of the growth of the calcifications, more complicated matching methods with prior information about splitting, merges, creation or clearance of calcifications are likely not able to increase the quality of the matching without biasing the resulting growth pattern. We have based our growth descriptors on one-to-one correspondence; where there is only found one area overlap between the baseline and follow-up calcifications, see Fig. 2. The one-to-one correspondence ensures that no bias effect in the interpretation of how a one-to-many or many-to-one correspondence is created.

5 The Growth Measurements

The growth of the calcifications can be measured in three different biologically meaningful directions; longitudinal (in the blood flow direction), circumferential (around the aorta) and radial (the direction into the aorta).

Our hypothesis is that these directions can give good indicators of the growth pattern. The longitudinal growth would give an idea of whether the calcifications are making the aorta wall more stiff, due to calcifications occupying a longer part of the aorta wall. We have measured the longitudinal growth as the change in height of the calcifications. The x-ray attenuation makes the calcifications on the anterior/posterior sides of the aorta wall most visible in the x-ray images. This makes us capable of measuring the radial growth as the change in width of the calcifications. The area of the calcifications could give information about the overall growth of the calcifications. The area of the calcifications combines contributions from the circumferential and radial directions, due to the 2D projection. Because of the x-ray attenuation, the area will be based mainly on the radial and longitudinal direction.

To measure the overall growth direction we calculate the difference in the center of mass of the matched calcifications. This way we should get an identifier of the longitudinal growth direction. The difference in center of mass could also

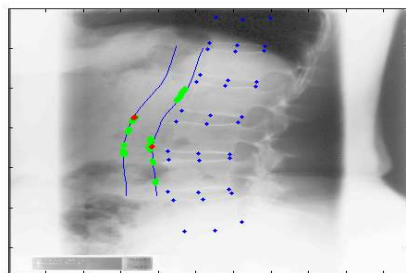


Fig. 2. An example of the matched calcifications. Blue shows the annotations of the vertebrae and the aorta wall. Red are the baseline calcifications and green are the follow-up calcifications. Note that the area overlap is a good indicator of the matching calcifications.

give an indicator of the radial growth direction, but we have to keep in mind that calcifications on the anterior and posterior aorta walls both grow towards the center of the aorta; causing the mean change in the radial direction to be canceled out by the movements in opposite directions.

The knowledge of the directions in the aorta is an important indicator of the growth pattern, because the growth needs to be measured in an aorta coordinate system. We have assumed that the y-direction in the images corresponds to the longitudinal direction and the x-direction to the radial direction which is a simple approximation to the aorta coordinate system. In future work the growth patterns will be based on the shape of the aorta.

Measurements of the shape of the calcifications in any direction using shape models or moments will be hard to interpret without biasing the growth patterns due to the projections into 2D and the correspondence to the aorta coordinate system. We have chosen to use the least committed method to avoid influence of artifacts in our method. The height H of a calcification is therefore simply measured as:

$$H = \max(y_1, \dots, y_i) - \min(y_1, \dots, y_i), \quad (3)$$

where y_i is the y-coordinate of the i'th boundary point of the calcification.

We have based the width of the calcification on the local width to avoid overestimation due to the curvature of the aorta. The width calculation is based on a modified scan-line algorithm [11], that finds the width for each scan-line through the calcifications and then chooses the maximal local width as the width of the calcification. The area of a calcification [12] is measured as:

$$A = \frac{1}{2} \sum_{i=1}^n (x_i y_{i+1} - x_{i+1} y_i), \quad (4)$$

where (x_i, y_i) are the i'th boundary point of a calcification and n is the total number of annotation points. The center of mass (CM) of the calcification is calculated as the position of the calcification in the aorta. This way we can describe the growth direction based on differences in the center of mass position for the matched registered calcifications. We assume the mass density is uniform and then by use of Green's theorem the CM is given by 5, where A is the area and (x_i, y_i) is the i'th annotation of the calcification [12]:

$$\begin{aligned} CM_x &= \frac{1}{6A} \sum_{i=1}^n (x_i + x_{i+1})(x_i y_{i+1} - x_{i+1} y_i) \\ CM_y &= \frac{1}{6A} \sum_{i=1}^n (y_i + y_{i+1})(x_i y_{i+1} - x_{i+1} y_i) \end{aligned} \quad (5)$$

6 Validation of Matching

The total number of calcifications at baseline is 611 and the number increases to 1321 at follow-up. We have been able to match 32.4% of the baseline calcifications to one corresponding follow-up calcification. This is in respect to 16.4% one-to-many correspondences (the calcifications may have grown together) and to 8.7% many-to-one correspondence, and 42.4% where no correspondence were

Table 1. The mean and standard deviation of the area, height and width of the unmatched and matched calcifications in mm. †= $p < 0.1$, *= $p < 0.05$, **= $p < 0.01$ and ***= $p < 0.001$ on a unpaired t-test between the unmatched and matched calcifications and a paired t-test for the growth. Note that the matched calcifications is a little larger than the total number of calcifications and that the calcifications grows significantly in area, height and width and the position of the calcifications in the aorta is moved in the blood flow direction.

| | Unmatched Baseline | Unmatched Follow-up | Matched Baseline | Matched Follow-up | Growth |
|----------------------------|-----------------------|------------------------|---------------------|----------------------|------------------|
| Area (mm ²) | 172** (± 199) | 211*** (± 313.57) | 205 (± 206) | 325 (± 317) | 120*** (± 240) |
| Height (mm) | 5.02** (± 3.75) | 5.76*** (± 4.81) | 5.81 (± 3.55) | 8.35 (± 5.26) | 2.53*** (± 4.33) |
| Width (mm) | 2.12† (± 1.20) | 2.23* (± 1.35) | 2.17 (± 1.24) | 2.46 (± 1.45) | 0.29** (± 1.32) |
| Cx (mm) | - | - | - | - | 0.91*** (± 0.81) |
| Cy (mm) | - | - | - | - | 2.02*** (± 1.95) |

found. In an intra/inter observer study of the manual annotations, the radiologists have area overlaps of 40-60 % of the calcifications. The relative low reproducibility in the annotations could account for a large number of the non-matched calcifications. The average size of the matched calcifications is a little larger than the average baseline calcification - e.g. mean height of unmatched and matched baseline calcifications are 5.02 mm and 8.35 mm respectively. This is due to difficulties in matching the smaller registered calcifications and the increased activity in the growth of the new and smaller calcifications. Tab. 1 shows mean and standard deviations for heights, widths and areas of the unmatched and matched calcifications.

7 Characterizing the Growth of the Calcifications

The linear correlation coefficients for unmatched and matched calcifications for the height, width and area can be seen in Tab. 2. Intuitively there are correlations between growth in area and growth in height and width. Our results also show a correlation between growth in width and height, indicating that calcifications grow both longitudinally and radially.

The characteristics of the growth of the calcifications can be seen in Tab. 1, based on signed values. The results show that the matched calcifications are growing longitudinally with a mean growth of 2.53 mm (± 4.33). This is an increase of 50.4 %. The mean growth in the radial direction is 0.29 mm (± 1.70), corresponding to 13.7 %, see Fig. 3. The center of mass is moved 2.02 (± 1.95) mm in the longitudinal direction, see Fig. 3. The absolute anterior/posterior center of mass movement is 0.91 (± 0.81) mm in the absolute inside radial direction. This indicates that more calcifications are placed on the anterior wall or the calcifications are growing towards the posterior wall.

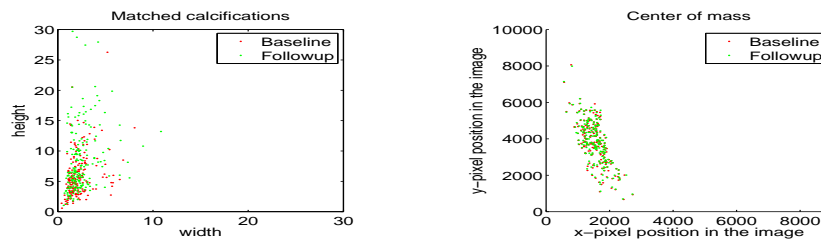


Fig. 3. Height and width (left) and center of mass (right) of the matched calcifications. Red is baseline and green is follow-up. Note that the calcifications grow longitudinally and the center of mass is moved in the flow direction.

We have correlated our growth patterns with known biological risk factors [13], see Tab. 3. A high cholesterol or triglyceride level correlates with growth in width and area of the calcifications. High glucose level correlates with growth in area and height of the calcifications.

8 Discussion and Future Work

The registration and matching process is necessary to describe the growth patterns for the calcifications and especially the growth direction, measured by change in the center of mass. Our results show that the calcifications grow longitudinally and the center of mass is moved with the blood flow. The calcifications will occupy more of the aorta wall as they grow. The calcifications grows downward the aorta, which could be caused by the turbulence in the direction of the blood flow, when the aorta wall becomes non-smooth, due to the existing calcifications.

Our results show that high cholesterol and triglyceride levels correlate with growth in width of the calcifications. This could correspond to intimal calcifications that likely are related to cholesterol and lipids that induce atherosclerosis [14]. A high glucose level correlates mainly to growth in heights possibly corresponding to the elongated medial calcifications observed in diabetes patients [2]. Glucose is a main factor of growth of all types of calcifications, which

Table 2. The linear correlation coefficient of the width, height and area of the matched and non matched calcifications. The correlations are all significant with $p < 0.001$. Note that there is correlation between height and width indicating that the calcifications grow longitudinally and radially.

| Correlation coefficient | Width vs. Height | Width vs. Area | Height vs. Area |
|-------------------------|------------------|----------------|-----------------|
| Baseline (unmatched) | 0.5156 | 0.7664 | 0.8587 |
| Follow-up (unmatched) | 0.5240 | 0.7443 | 0.8250 |
| Baseline (matched) | 0.3412 | 0.7391 | 0.8062 |
| Follow-up (matched) | 0.2701 | 0.7340 | 0.7380 |
| Growth | 0.2302 | 0.6753 | 0.7053 |

VIII

Table 3. The linear correlation between our growth patterns and the biological risk factors; †= $p < 0.1$, *= $p < 0.05$, **= $p < 0.01$ and ***= $p < 0.001$. Note correlation between area/width and cholesterol, area/height and glucose and area/height and triglyceride.

| Correlation coefficient and p-values | Cholesterol | Glucose | Triglyceride |
|--------------------------------------|-------------|---------|--------------|
| Growth in area | 0.21* | 0.33** | 0.21* |
| Growth in height | 0.15 | 0.39** | 0.22* |
| Growth in width | 0.26** | 0.20† | 0.18† |

can also be seen in the correlation.

At this point we can describe clinically meaningful growth patterns of the atherosclerotic plaques. More work will be based on modifying the growth patterns and get correlations with the different characteristic biomarkers. We will also try to further distinguish the growth pattern of medial and intimal calcifications [14] in our future growth patterns. We have shown that registration and plaque matching based on x-ray images can give a good description of the growth patterns, which indicates the ability for a simple and low cost method to measure the longitudinal progression of atherosclerosis.

Acknowledgments: We thank the radiologists Paola C. Pettersen, Qing He, and Jianghong Chen from CCBP for providing the annotated x-rays used in this study.

References

1. European Heart Network (EHN): <http://www.ehnheart.org/content/>
2. M. Abedin, Y. Tintut, L. Demer: Vascular Calcifications: Mechanisms and Clinical Ramifications. *Arterioscler. Tromb. Vasc. Biol.* 24, 1161–1170 (2004)
3. D.A. Eggen, J.P. Strong, and H.C.J. McGill: Calcification in the Abdominal Aorta: Relationship to Race, Sex, and Coronary Artherosclerosis. *Arch. of Path.* (1964)
4. J.H.C. Reiber, G. Koning, J. Dijkstra, A. Wahle, B. Goedhart, F.W. Sheehan, M.Sonka: Angiography and Intravascular Ultrasound. *Med. Imag.* 2, (2000)
5. E. Kuhl, R. Maas, G. Himelh, A. Menzel: Computational Modeling of Arterial Wall Growth. *Bio. Mo. Mech.* 6(5), 321–331 (2007)
6. H. Jin, K. Ham, J.Y. Chan, L.G. Butler, R.L. Kurtz, S. Thiam, J.W. Robinson, R.A. Agbaria, I.M. Warner, R.E. Tracy: High Resolution Three-dimensional Visualization and Characterization of Coronary Atherosclerosis *in vitro* by Synchrotron Radiation X-ray Microtomography and highly Localized X-ray Diffraction. *Phy. in Med. and Bio.* 47, 1–12 (2002)
7. D.P. Kiel, L. I. Kauppila, L. A. Cupples, M. T. Hannan, C. J. O'Donnell, P. W. F. Wilson: Bone Loss and the Progression of Abdominal Aortic Calcification over a 25 Year Period: The Framingham Heart Study. *Calc. Tis. Int.* 68, 271–276 (2001)
8. L.I. Kauppila, J.F. Polak, L.A. Cupples, M.T. Hannan, D.P. Kiel, P.W.F. Wilson: New Indices to Classify Location, Severity and Progression of Calcific Lesions in the Abdominal Aorta: a 25-year Follow-up Study. *Atheroscler.* 132, 245–250 (1988)
9. L. Conrad-Hansen, M. de Bruijne, F. Lauze, L.B. Tank, P.C. Pettersen, Q. He, J. Chen, C. Christensen, M. Nielsen: Quantifying Calcification in the Lumbar Aorta on X-ray Images. eds.: MICCAI Vol. 4792 of LNCS (2007) 352–359
10. F. L. Bookstein: Principle Warps: Thin-Plate Splines and the Decomposition of Deformation. *IEEE Trans. Pat. Anal. Mach. Int.* 11(6), 567–584 (1989)
11. J.D. Foley, A. van Dam, S.K. Feiner, J.H. Hughes: *Computer Graphics; Principles and Practice*. eds.: Addison-Wesley (1996)
12. Brian Mirtich: Fast and Accurate Computation of Polyhedral Mass Properties. *Jour. of Graph. Tools* 1 (2), 31–50 (1996)
13. J.C.M. Witteman, J.L.C. Van Saase, H.A. Valkenburg: Aortic Calcifications as a Predictor of Cardiovascular Mortality. *Lancet* (2), 1120–1122 (1986)
14. D. Proudfoot, C.M. Shanahan: Biology of Calcifications in Vascular Cells: Intima versus Media. *Herz* 26(4), 245–251 (2001)

Segmentation of Intravascular Ultrasound Images using Graph Search and a Novel Cost Function

Richard W. Downe¹, Andreas Wahle¹, Tomáš Kovárník²,
Hana Skalická², John J. Lopez³, Jan Horák², and Milan Sonka¹

¹ University of Iowa, Dept. of Electrical & Computer Engineering, Iowa City, USA

² Charles University in Prague, First Faculty of Medicine, Prague, Czech Republic

³ University of Chicago, Dept. of Medicine, Division of Cardiology, Chicago, USA

Abstract. Intravascular ultrasound (IVUS) is a valuable tool to assess atherosclerotic plaque in coronary arteries. However, IVUS is also an inherently noisy modality and is difficult to segment. We have developed a new approach based on 3-D optimal graph search and a novel cost function. Principal component analysis is used for pre-processing, and active contours provide the initial segmentation for the graph search. Our method was validated *in vivo* against manual expert tracings in IVUS pullbacks from 15 patients, demonstrating a good performance.

1 Introduction

Cardiovascular diseases are among the leading causes of death in the industrialized world. X-ray angiography is commonly used to assess atherosclerosis in coronary arteries, which however is limited to displaying the contrast-dye filled lumen and allows only an indirect assessment of atherosclerotic plaque. Intravascular ultrasound (IVUS) has been developed for analysis of angiographically visible and non-visible plaques, also more recently allowing plaque characterization. Of special interest are the lumen/plaque border, marking the inner boundary, and the media/adventitia border, marking the outer boundary of the vessel. Klingensmith et al. provide an overview of segmentation methods in [1]. IVUS is an inherently noisy modality, which makes conventional edge and region based segmentation techniques largely ineffective by themselves. Common methods are based on deformable geometries [2] or graph search with minimum-cost algorithms [3, 4]. Our approach uses optimal graph search in combination with a novel cost function. Li et al. [5] demonstrated an adaptation of max-flow/min-cut graph search techniques to optimal surface detection which permits an optimal solution to the problem of multiple surfaces in n -dimensions in polynomial time. This technique is ideally suited to the problem of IVUS segmentation, also allowing a simultaneous 3-D segmentation by coupling of the two borders.

Using the Rayleigh distribution for segmentation works well for catheters with high frequency (≈ 40 MHz). In our case, images from the Volcano IVG 3 were acquired using a solid-state catheter with much lower frequency (20 MHz).

This reduces the incidence of blood speckle in the lumen considerably, thus the Rayleigh correlation derived cost function fails to yield a usable segmentation.

A different approach is to filter out the Rayleigh-distributed speckle rather than trying to utilize it for segmentation of lower-frequency images. Lueck et al. [6] successfully applied principal component analysis (PCA) to the reduction of such noise in ultrasound images of the liver. Tao et al. [7] further applied the technique to the isolation of specific features (vessel wall) in Doppler ultrasound, further suggesting its utility for vascular segmentation. We developed a sliding-window approach to consider a restricted segment before and after the IVUS frame under consideration for PCA-based filtering. After quantization and thresholding using a method similar to Otsu [8], an active contour provides the initial segmentation as basis for a following graph-search segmentation step [4, 5]. Regional costs terms are used for the inner contour, 3-D edge terms for the outer contour. Interactive resegmentation allows for easy semi-automated manipulation of the result where necessary.

2 Methods

2.1 Pre-Processing

Principal Component Analysis. Lueck et al. [6] demonstrated a method for removing Rayleigh distributed noise from liver ultrasound images to improve segmentation results. The liver changes relatively little during imaging, whereas anywhere from 600 to 3000 or more IVUS frames are taken along the segment of the coronary artery, depending on pullback length, speed of the pullback, and acquisition rate. Of these frames, roughly 100–300 end-diastolic frames remain after gating, which are used in the present study. The appearance of the artery tissues being imaged often changes dramatically from frame to frame, and features are often extremely ambiguous, even for an expert. The use of phase-synchronous (here: end-diastolic) frames minimizes effects from cardiac motion. The remaining variability in appearance is handled by only processing a small sliding window at a time, thereby preserving most important local information in each frame while minimizing the loss of detail. Local intensity values were far more uniform and edges much stronger, making the extraction of cost terms for the graph search simpler than they otherwise might have been.

The entire pullback is treated as a matrix where the mean frame is computed and then subtracted from each frame on a voxel by voxel basis. The resulting matrix is multiplied by its transpose, to form a covariance matrix. This covariance matrix is a square matrix of dimension equal to the number of frames in the window. The sequence is outlined in the equations below, where the I 's are the frames, Ψ is the average frame, C is the covariance matrix, and $2W + 1$ is the size of the window (with $W = 6$ used in this study). In this way, we obtain the matrix containing the eigenvectors of the window in E , where X are the eigenvectors of C .

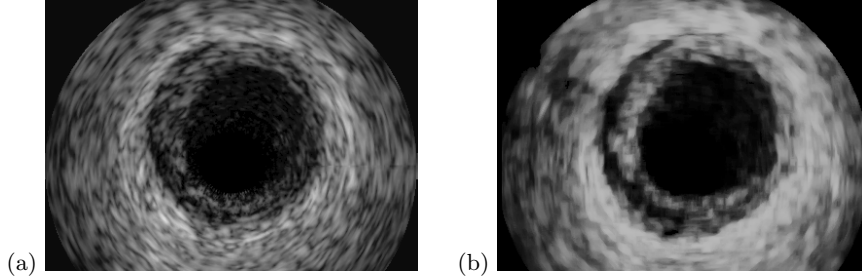


Fig. 1. Example of PCA output: (a) raw IVUS frame, (b) PCA-filtered frame.

$$\Psi = \frac{1}{2W+1} \sum_{n=-W}^{+W} \Gamma_n \quad (1)$$

$$\Phi_i = \Gamma_i - \Psi \implies A = [\Phi_0 \Phi_1 \dots \Phi_{2W}] \quad (2)$$

$$C = AA^T \quad (3)$$

$$E = [\Gamma_{-W} \dots \Gamma_0 \dots \Gamma_{+W}]^T X \quad (4)$$

The eigenvectors of C represent the principal modes of intensity variation in the image data as a function of position in the frame – thus the net effect is to isolate commonalities between the frames in the selected window. Done correctly, this should reduce noise and, more importantly, increase the homogeneity of intensity within the regions of interest. Figure 1 shows the effect of multiplying the 6 greatest magnitude eigenvectors computed over a ± 6 frame window back against the original frame. The vessel wall (outside the outer border) is fairly uniformly high intensity (white), and the plaque layer is shown as a darker band just inside, while the blood speckle within the lumen is filtered out such that the lumen now has an appearance of uniform black.

The eigenvectors are sorted in order of eigenvalue magnitude. This has the implicit theoretical effect of treating the noise in the IVUS images as Gaussian distributed noise. This is strictly speaking incorrect. For optimal results, it would be best to sort them by their correlation with a Rayleigh distribution [6]. This is an avenue that may be pursued in the future to improve the results; however it can be seen from Figure 1 that simple sorting by magnitude yields a substantial clarification of the borders of interest.

Quantization and Thresholding. The PCA procedure yields a floating point image with fractional intensity values, with a large bias near zero. To effectively make use of the image, we quantize the image to integral values and then perform a histogram equalization. To preserve as much information as possible within the image, two different quantization levels are used: a higher, initial level, to which each of the original floating point values are mapped prior to the equalization,

and a lower, collapsed final value, to which the values are remapped after a histogram equalization is performed. Finally, the image is median filtered to clean up any residual blood speckle and optimal thresholding is applied, as described by Otsu [8], but the intensity values of the pixels are not actually changed. Instead, the algorithm runs to the point of convergence and returns a threshold. This threshold is then defined as the stopping criterion for the subsequent estimation of the lumen boundary by an active contour.

Active Contour Estimation. IVUS images frequently contain large sections of dark shadow from highly echogenic plaque deposits, such as calcifications, which can adversely impact the overall border. Side branches are not followed, but introduce gaps in the contours at the bifurcation site which need to be bridged. A priori, we know that the border should be roughly elliptical, in all but the most diseased cases. While the PCA makes it possible to extract the cost information from local neighborhood information, it is useful to have an estimation of the location of the border prior to computing these cost terms, in order to address gaps in the border, shadows, and other artifacts. An initial estimate of the location of the lumen border is made using a spline-based active contour model.

On the data sets targeted with this cost function, the lumen is uniformly black in the center, and may contain blood speckle with low intensity values at its outer edges. The lumen/plaque border, after the histogram equalization, is nominally rather bright, but may contain holes as a result of shadows or artifacts preserved by the PCA. To account for that, 72 control points are initialized at the center and sequentially perturbed by one pixel at a time. After each perturbation, 360 data points around the contour are interpolated from the original 72 using B-splines, and each in turn is checked to see if the pixel beneath it has an intensity value above the computed threshold. If it does, the control point that caused the data point in question to cross the pixel is frozen, and its position is backtracked by 1 pixel to its location prior to the crossing of the threshold. This procedure continues until all control points are frozen. This gives us a contiguous border with a plausible shape sufficiently approximating the actual border.

2.2 Regional Cost Terms (Inner Border)

The estimate of the border computed with the active contour model of Section 2.1 may be close, but needs refinement. The PCA procedure considerably improves the homogeneity of the pixel intensity values throughout the image, thus we can use these as regional information. The cost terms for the inner border are formulated based on the local neighborhood and proximity to the estimated border from the active contour result. Those terms are generated according to:

$$C(r, \theta) = R(x, y, \theta) + D(r, \theta) \quad (5)$$

$$D(r, \theta) = e^{\frac{r-E(\theta)}{4}} + e^{\frac{E(\theta)-r}{2}} \quad (6)$$

$$R(x, y, \theta) = \begin{cases} 0 & x, y \text{ outside ROI,} \\ \sum_{n=0}^{nSize} I_{PCA}(x + n_x(\theta), y + n_y(\theta)) & \text{else} \end{cases} \quad (7)$$

The region of interest is designed to coincide with the same parts of the image where $D(r, \theta)$ is small – the exponent is small where we examine the local neighborhood, and it is large everywhere else in order to emphasize the ROI in the graph search. $E(\theta)$ is the location of the active contour at each angle θ . n_x and n_y are the x and y components of the normal to the active contour at each angle θ . $nSize$ is the size of the neighborhood, in the current implementation that value has been set to 15. The region of interest has been set to 8 pixels on either side of the active contour. Raw intensity information from the PCA output is used as the cost information. This has the benefit of more predictably uniform gray values; it also means that places where the PCA loses information the regional cost terms may suffer.

2.3 3-D Edge Terms (Outer Border)

The outer border was virtually impossible to identify with the active contour model used to estimate the inner border. The presence of plaque between the two borders makes it very difficult to identify a suitable stopping criterion. Edge information exists, but suffers due to the noise in the image. Moreover, simple edges fail to take 3-D relationships into account. To address this, we used a 3-D “ridge detection” for the cost terms for the outer border. For these terms, we used a single 7 by 7 convolution mask on a log-polar representation of the image. Two convolution operations were performed: one normal to the direction of the pullback, in the plane of the individual frames, such that the two dimensions were the radial and angular directions (r, θ), and the other in the longitudinal direction, (directions r, z). The kernel used was designed to emphasize the fact that the voxels immediately outside the media/adventitia surface were often some of the brightest in the image, while those below it are much darker.

$$\begin{pmatrix} +2 & +3 & +4 & +5 & +4 & +3 & +2 \\ +2 & +3 & +4 & +5 & +4 & +3 & +2 \\ +3 & +4 & +5 & +6 & +5 & +4 & +3 \\ 0 & 0 & 0 & 0 & 0 & 0 & 0 \\ -1 & -2 & -3 & -4 & -3 & -2 & -1 \\ -2 & -3 & -4 & -5 & -4 & -3 & -2 \\ -2 & -3 & -4 & -5 & -4 & -3 & -2 \end{pmatrix} \quad (8)$$

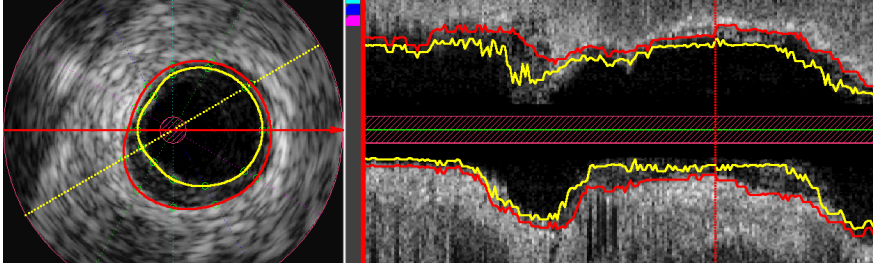


Fig. 2. New cost function tested on Volcano data.

2.4 Interactive Resegmentation

The 3-D graph search method described in more detail in [4, 5] is employed with our new cost functions to simultaneously detect both borders. Automated segmentations may naturally fail. Most frequently, this is caused by artifacts providing a high attraction to minimize the cost, or gaps in the boundary resulting in a high cost for the correct path. To compensate, we allow the user to manually trace a portion of the border where the computed segmentation has failed in one or more longitudinal planes. Then, all costs on a surface corresponding to the traced portion plus a spline-estimated surrounding region stretching to the adjacent longitudinal planes (the tracing tool uses a total of 6 such planes) are set to an arbitrarily chosen, but highly negative value. The cost terms in a local volume neighborhood of the computed surface are then subjected to Gaussian smoothing to retain the original cost information as being relevant, and to account for inaccuracies in the border location indicated by the user. Then, the graph search is recomputed with the altered cost function.

3 Results

3.1 Experimental Methods and Quantitative Analysis

Data from 15 patients were available, all imaged at the Charles University in Prague, Czech Republic. A Volcano IVG 3 imaging system was used with 20 MHz solid-state catheters. The typical processing time for the automated border detection was 2–3 minutes on a 2.4 GHz Intel Core2 processor (quad-core, only a single core used). Error metrics used for the evaluation of the cost function were computed point by point, at 360 angles around the border. Mean per-point signed, unsigned, and root-mean-square (RMSE) errors were determined radially from the frame center over all points in all pullbacks. The area error was computed by taking an estimate of the area within each border on each frame, computing the error frame by frame, and then taking the signed and unsigned means and the RMSE.

Figure 2 shows an example of our new cost function’s performance on data from the Volcano catheters. Table 1 illustrates the quantitative analysis of our

Table 1. Error statistics for Volcano catheter, using our cost function

| Data from 15 patients: | Lumen/Lamina | | | Media/Adventitia | | |
|--|--------------|----------|-------|------------------|----------|-------|
| | Signed | Unsigned | RMSE | Signed | Unsigned | RMSE |
| Positioning Error [†] | -0.123 | 0.302 | 0.482 | 0.004 | 0.240 | 0.390 |
| — failures >20 pixels removed | -0.016 | 0.178 | 0.220 | 0.042 | 0.141 | 0.186 |
| — failures >10 pixels removed | -0.005 | 0.117 | 0.137 | 0.027 | 0.097 | 0.120 |
| Area Error [‡] | -2.174 | 2.709 | 4.437 | 0.684 | 2.726 | 4.224 |
| Error statistics, single patient, after interactive resegmentation | | | | | | |
| Positioning Error (Before) [†] | -0.109 | 0.132 | 0.245 | -0.232 | 0.242 | 0.472 |
| Positioning Error (After) [†] | -0.095 | 0.125 | 0.238 | -0.046 | 0.115 | 0.273 |
| Area Error (Before) [‡] | -1.297 | 1.298 | 2.277 | -3.369 | 3.398 | 6.484 |
| Area Error (After) [‡] | -1.178 | 1.178 | 2.110 | 0.370 | 1.042 | 2.238 |
| Inter-Observer Variability, three patients | | | | | | |
| Positioning Error [†] | 0.041 | 0.127 | 0.210 | 0.011 | 0.072 | 0.104 |
| Area Error [‡] | 0.750 | 1.117 | 1.493 | 0.724 | 1.180 | 2.129 |

[†] Values in mm distance, computed point by point along the border.

[‡] Values in mm², estimated by triangulation. (1 pixel \approx 0.026 mm)

new cost function. The unsigned error value indicates that the performance is roughly equal to that reported in [4] for a Boston Scientific system with rotating 40 MHz transducer. Figure 2 also shows that there are often places within a segmentation that don't require any manual correction at all. Despite our new cost function being correct in the majority of cases, occasional failures as reflected by the RMSE errors have to be addressed.

3.2 Interactive Resegmentation

Due to the distribution of the segmentation errors, we evaluated the performance both over all data and with gross outliers excluded. We computed the error statistics with all samples as well as with any samples for which signed error was greater than 20 and 10 pixels each excluded. Table 1 shows that the error becomes much smaller when these failures are excluded, as would be expected, a point also reflected in the fact that the RMSE for both borders is considerably higher than the unsigned positioning error. The remaining errors are in the range of the inter-observer variability, determined in a subset of three patients.

Removing error samples regarded as outright failures has justification beyond theoretical definition of failure. We developed a feature for our segmentation program that permits an interactive resegmentation as discussed in Section 2.4. This feature works remarkably well, as demonstrated in Figure 3. In the initial segmentation, the outer border is completely missed in the latter half of the pullback, as the edge detector gets caught on the strong edges at the lumen/plaque surface. This in turn pushes the inner border several voxels into the vessel during this part of the pullback, causing increased error throughout. By manually tracing the outer border in a single longitudinal plane at two segments, and then

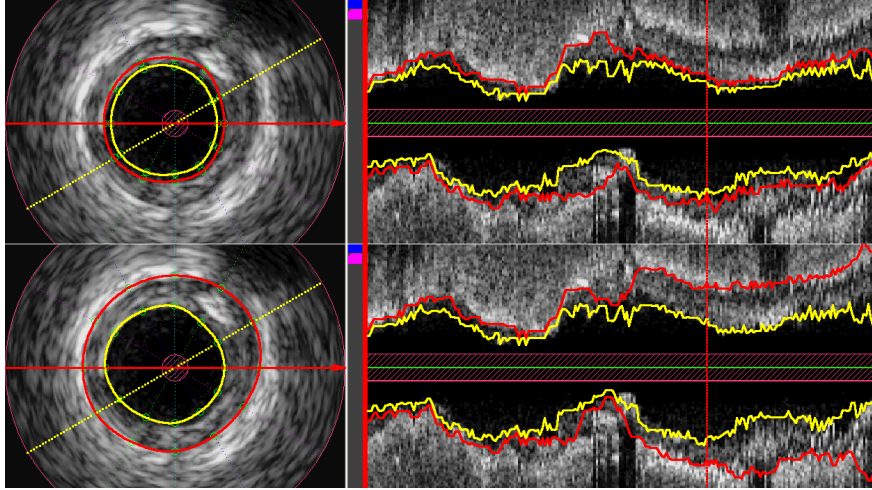


Fig. 3. IVUS frame in which the initial segmentation failed, before (top) and after (bottom) interactive resegmentation, by modifying only two outer-border segments in a single longitudinal plane.

re-running the graph search, we were able to completely correct this portion of the pullback, illustrating that the underlying cost function contained most of the information required for a correct segmentation, but localized errors caused the graph search to occasionally find an incorrect path in certain places.

4 Discussion and Conclusions

In summary, a new cost function for the segmentation of intravascular ultrasound data acquired with a solid-state catheter using optimal dual-surface detection graph search methods has been developed and validated against 15 manual tracings by human experts. While there remains room for improvement, the segmentation is accurate enough in a substantial number of cases not to require any manual correction. Table 1 shows that our error on the Volcano data is roughly comparable to that of a cost function reported for Boston Scientific catheters. Figure 2 and the RMSE values for the new cost function show better results than the error statistics indicate for those cases where it works well, and substantial deviations where it fails. Critical areas are pockets or regions of concavity artificially filled in by the combination of blood speckle with high intensity voxels adjacent to these, or lesions protruding into the vessel are completely eliminated due to zero intensity valued voxels on either side. To allow for easy correction of these areas, we developed a method for manually guiding the segmentation back onto the right track. Figure 3 shows that this method works well without the need for retracing the contours across larger segments as necessary with other methods.

Acknowledgments

The authors would like to thank Elisabeth J. Buettner, University of Iowa Department of Internal Medicine, for the expert tracings; funding was provided in part by NIH R01 HL063373 and R01 EB004640.

References

1. Klingensmith, J.D., Schoenhagen, P., Tajaddini, A., Halliburton, S.S., Tuzcu, E.M., Nissen, S.E., Vince, D.G.: Automated three-dimensional assessment of coronary artery anatomy with intravascular ultrasound scanning. *American Heart Journal* **145**(5) (May 2003) 795–805
2. Brusseau, E., de Korte, C.L., Mastik, F., Schaar, J., van der Steen, A.F.W.: Fully automatic luminal contour segmentation in intracoronary ultrasound imaging — A statistical approach. *IEEE Trans. Medical Imaging* **23**(5) (May 2004) 554–566
3. Li, W., von Birgelen, C., Di Mario, C., Boersma, E., Gussenhoven, E.J., van der Putten, N.H.J.J., Bom, N.: Semi-automatic contour detection for volumetric quantification of intravascular ultrasound. In: *Proc. Computers in Cardiology 1994*, Bethesda MD, Los Alamitos CA, IEEE-CS Press (1995) 277–280
4. Wahle, A., Lopez, J.J., Olszewski, M.E., Vigmostad, S.C., Chandran, K.B., Rossen, J.D., Sonka, M.: Plaque development, vessel curvature, and wall shear stress in coronary arteries assessed by X-ray angiography and intravascular ultrasound. *Medical Image Analysis* **10**(4) (August 2006) 615–631
5. Li, K., Wu, X., Chen, D.Z., Sonka, M.: Optimal surface segmentation in volumetric images—a graph theoretic approach. *IEEE Transactions on Pattern Analysis and Machine Intelligence* **28**(1) (January 2006) 119–134
6. Lueck, G., Burns, P.N., Martel, A.L.: Data weighting for principal component noise reduction in contrast enhanced ultrasound. In: *MICCAI 2006: LNCS 4191*, Springer-Verlag Berlin Heidelberg (October 2006) 76–83
7. Tao, Q., Wang, Y., Fish, P., Wang, W., Cardoso, J.: The wall signal removal in Doppler ultrasound systems based on recursive PCA. *Ultrasound in Medicine and Biology* **30**(3) (2004) 369–379
8. Otsu, N.: A threshold selection method from gray level histograms. *IEEE Trans. Systems, Man and Cybernetics* **9** (March 1979) 62–66

3-D Symbolic Reconstruction of Coronary Artery Tree from Multiple Views of Rotational X-Ray Angiography

Rui Liao¹, Yiyong Sun¹, Luc Duong¹

¹ Siemens Corporate Research, Princeton, NJ, 08540 USA

Abstract. The purpose of this study is to present an efficient and robust method for 3-D symbolic reconstruction of coronary artery tree from multiple ECG-gated views of X-ray angiography. 2-D coronary artery centerlines are extracted automatically from X-ray projection images using enhanced multi-scale analysis. For the difficult data with low vessel contrast, semi-automatic tool based on fast marching method is implemented to allow for user modification on the automatically-extracted 2-D centerlines. We first formulate 3-D symbolic reconstruction from multiple views as an energy minimization problem incorporating a soft epipolar line constraint and a smoothness term evaluated in 3-D. The minimization output, i.e. the 3-D coronary artery centerlines, therefore can be robust to the inaccuracies in 2-D centerline extraction and is inherently smooth in 3-D. We further propose to solve the energy minimization problem using α -expansion moves of Graph Cuts, a powerful optimization technique that yields a local minimum in a strong sense at relatively low computational complexity. Experiments on a synthetic phantom and on real porcine and human datasets demonstrate the efficacy of the proposed method.

1 Introduction

Cardio-Vascular Disease (CVD) is responsible for more than one third (36.3%) of total deaths in the United States in 2004 [1]. The gold standard for diagnosis of CVD is X-ray coronary angiography, which are 2-D projections of the coronary arteries and hence are subject to significant foreshortening that limits clinicians' ability to accurately determine geometric properties of coronary arteries and intracoronary devices. It is shown in [2] that 3-D reconstruction of coronary arteries from traditional angiography allows for 3D measure of the lesion length and hence is a promising technique to optimize the choice of length and number of stents used during Percutaneous Coronary Intervention (PCI). 3D symbolic model can further guide clinicians to choose the optimal patient-specific views that minimize vessel overlap and foreshortening [3,4,5], and provides the magnification factor for the vessel that's needed for estimation of lumen diameter in 3D [6,7]. Furthermore, 3D symbolic reconstruction is a critical step in modeling the dynamics and shape changes of coronary arteries during cardiac cycle [8], as well as in generating full vessel models by subsequent tomographic reconstruction for stenosis detection and analysis [7].

3-D symbolic reconstruction of coronary arteries from biplane angiography was investigated using two synchronized projections [4,5,8]. In many cases, however, using only two views is not sufficient to obtain a precise reconstruction of the complicated coronary tree, because the extracted 2-D vessel centerlines may not be accurate or complete due to low image contrast or superposition of vessels from a certain view. The advantage of utilizing multiple views for robust 3-D symbolic reconstruction of coronary trees was demonstrated in [6,7]. In these methods hard epipolar line constraint was typically imposed in order to reduce the number of candidate matching point per pixel, without which the computational complexity for the global optimiza-

tion by dynamic programming would be extremely high. However, hard epipolar line constraint is problematic for the vessels that are close to being parallel to the epipolar line or contain missing segments. In addition, smoothness regularization can be imposed only to the extent of the set of epipolar line intersection points, which are relatively sparse and hence, not guaranteed to be smooth in 3-D. Therefore, the reconstructed 3-D centerlines can be relatively jagged, especially when there is inaccuracy in the 2-D centerline extraction or projection matrix calibration.

A rotational X-ray sequence is acquired by rotating the C-Arm with constant SID (Source Intensifier Distance), constant cranio/caudal angle, and varying anterior/oblique angle in the range of -100 to 100 degrees, with the increment of ~ 2 degrees per projection. The goal of this paper is to describe an efficient and robust method for 3-D symbolic reconstruction of coronary artery tree using all the projections that correspond to the same cardiac phase. The contribution of this paper is twofold: first, Coherence Enhanced Diffusion (CED) is introduced for improved automatic coronary artery segmentation, and for the very difficult case of low contrast in coronary vessels where it is not reliable to perform fully automatic centerline extraction, semi-automatic interactive tool is implemented to allow user to edit the automatically extracted 2-D centerlines. Second, automatic 3-D symbolic reconstruction of coronary artery is formulated as an energy minimization problem that incorporates a soft epipolar line constraint and a smoothness term evaluated in 3-D, and is then realized using a new optimization approach named α -*expansion* moves of Graph Cuts (GCs) [9]. Graph Cuts has shown to be a powerful and efficient optimization technique, and has been successfully applied on a wide variety of computer vision problems including image restoration, stereo and motion, and image synthesis. For medical imaging, GCs optimization yields promising results for fast segmentation. To our knowledge, this is the first application of Graph Cuts technique for efficient 3-D centerline reconstruction of the coronary artery tree.

2 Methods

2.1 2-D Coronary Segmentation and Centerline Extraction

In order to reduce the noise and enhance coherent flow-like structures such as vessels in the X-ray projection images, a nonlinear diffusion technique named Coherence Enhanced Diffusion (CED) [10] is introduced. The diffusion equation is given by:

$$\partial_t I(x;t) = \nabla \cdot (D \nabla I(x;t)) \quad (1)$$

Here \mathbf{D} is a diffusion tensor that depends on local image structures so that not only the amount, but also the direction of the diffusion can be regulated. $t=3$ was adopted in our algorithm for the trade-off between performance and efficiency. Multi-scale Hessian-based filtering [11] is then applied on the CED preprocessed image to generate the vesselness feature image. The filter identifies the tubular structures using the eigenvalues λ_1 and λ_2 ($|\lambda_1| \ll |\lambda_2|$) of the **Hessian matrix**:

$$\mathbf{H}_\sigma = \sigma^2 \begin{bmatrix} \frac{\partial^2 \mathbf{u}_\sigma}{\partial x^2} & \frac{\partial^2 \mathbf{u}_\sigma}{\partial x \partial y} \\ \frac{\partial^2 \mathbf{u}_\sigma}{\partial x \partial y} & \frac{\partial^2 \mathbf{u}_\sigma}{\partial y^2} \end{bmatrix} \quad (2)$$

Here \mathbf{u}_σ is the convolution of the CED preprocessed image with a Gaussian kernel of size σ . Ideally σ should be the radius of the vessel of interest. The vesselness strength is calculated as [11]:

$$V_{\sigma} = \begin{cases} 0 & \lambda_2 < 0 \\ e^{R_b/2\beta^2} (1 - e^{-S^2/2\alpha^2}) & \lambda_2 \geq 0 \end{cases} \quad (3)$$

where $R_b = \lambda_1 / \lambda_2$, $S = \sqrt{\lambda_1^2 + \lambda_2^2}$, and the vesselness orientation is calculated as the eigenvector corresponding to λ_1 . Here α and β controls the sensitivity of the filter and was set to 3 and 1 respectively.

Coronary arteries are segmented by a hysteresis thresholding process on the vesselness image that retains connected components with all points that have vesselness above a low threshold and with at least one pixel with vesselness above a high threshold. The low and high thresholds were calculated as fixed quantiles (90 and 96 percent) of the accumulated histogram of the vesselness image. Only sufficiently large connected components are retained and the minimal size was set to 25 pixels. The segmented coronary arteries are then hole-filled by close operation and the centerlines are extracted automatically using topological thinning [12]. For large vessels with local diameter variations, small branches may be produced artificially by topological thinning. Only sufficiently long branches are retained by pruning and the minimal branch length was set to 5 pixels. Line linking is further performed according to their vesselness orientation and spatial location in order to connect those line segments that belong to the same vessel and are broken due to local vesselness discontinuity.

Our fully automatic 2-D centerline extraction algorithm in general works robustly for typical coronary angiography with sufficient contrast. Some examples are shown in Fig.1. Nevertheless, clinically there could be cases where the contrast of vessels is relatively low (e.g. due to diseases and blockages), and there is presence of peripheral anatomical structures of high contrast, as shown in Fig.2.a. Fully automated method that can robustly segment the coronary arteries in this challenging case is not yet known. Motivated by Intelligent Scissor (IS) [13] we propose a method for interactive editing of the automatically extracted centerlines when need is observed. In particular, when user moves the mouse, the shortest path between a seed point (e.g. the root of the coronary tree) and the current mouse position is searched on-the-fly by Fast Marching method [14]. The cost of a path L is:

$$C(L) = \sum_{p=1}^m 1/(0.001 + v(p)^4) + \omega S(L) \quad (4)$$

where $v(p)$ is the vesselness at pixel p , m is the number of pixels on the path L , $S(L)$ is the length of the path L , and ω controls the relative weights of these two factors (set to 50 experimentally). In order for the extraction of the smaller vessels to be less susceptible to the influence from the neighboring large vessels, a modified vesselness $v(p)$ is used. In particular, all points on the automatically extracted centerlines in Fig.2.e are assigned the same (maximum) value for their vesselness, and the vesselness for the points not on the automatically extracted centerlines is their coherence enhanced multi-scale vesselness response in Fig.2.c. Hence more accurate automatic centerline extraction leads to more convenient and robust semi-automatic editing. It can be seen that a path of stronger vesselness and shorter length is preferred over a path of weaker vesselness and a longer length. Since fast marching may produce jagged line segments due to the fact that it does not consider global topology, the output of the editing can be optionally smoothed by fitting B-Spline(s) that has minimized weighted summation of the total curvature and the distance to the original centerlines, as was done for the root segment pointed by the red arrows in Fig.2.f. A block diagram of the 2-D centerline extraction algorithm is shown in Fig.3.a.

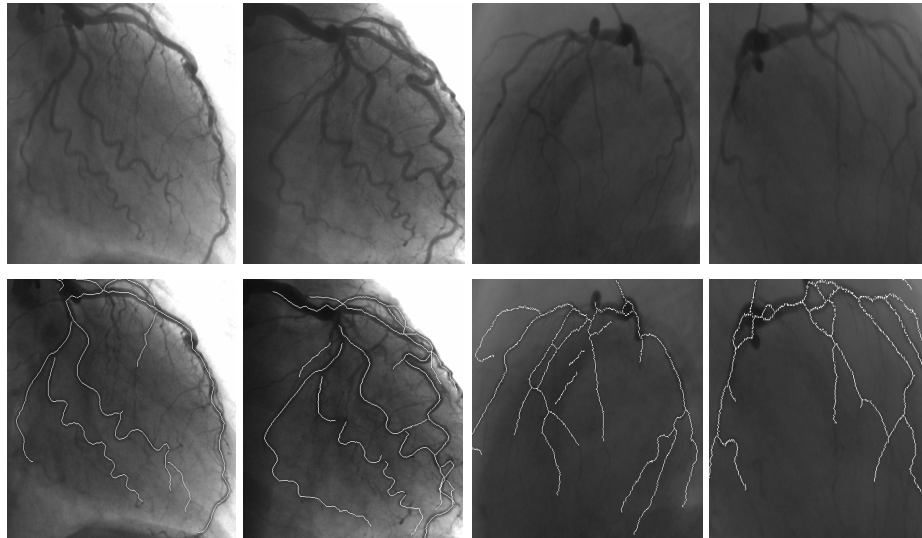


Fig. 1. X-ray angiography (upper) and automatically extracted coronary centerline (bottom).

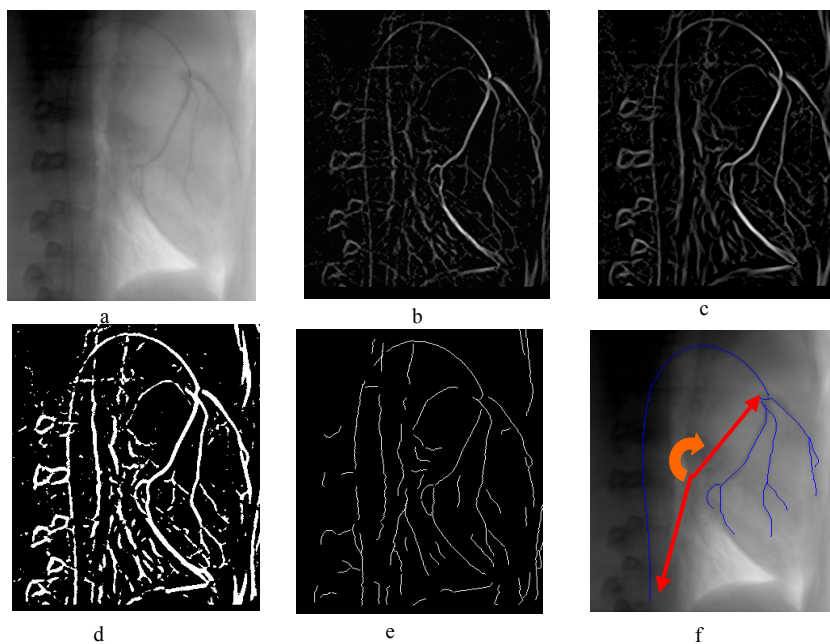


Fig. 2. Semi-automatic 2-D coronary artery segmentation and centerline extraction. (a) original X-ray image (b) multi-scale analysis (c) coherence enhanced multi-scale analysis (d) binarized mask by hysteresis thresholding (e) topological thinning with line segment pruning and connection (e) manual editing based on fast marching using the modified vesselness.

2.2 Multi-view Correspondence Matching

Suppose we have n views ($I_1 \dots I_n$) taken at the same cardiac phase and their corresponding acquisition geometry ($M_1 \dots M_n$). One view (I_1) is selected as the reference view and its optical center is computed according to M_1 . The 3-D space between the optical center and the imaging plane is divided into 3-D planes of equal depth increments, and a label l ($l \in L$) is attributed to each depth. Therefore, for a given pixel p on I_1 , (p, l) corresponds to a point in 3-D space, which is the intersection of plane l and the ray passing through the optical center and pixel p (Fig.3.b). The mapping for all the pixels on the 2D centerline P extracted from I_1 , $f : p \rightarrow f_p$ ($p \in P, f_p \in l$), is established via the minimization of the energy function:

$$E(f) = \sum_{p \in P} D_p(f_p) + \beta \sum_{p, q \in N} V_{p, q}(f_p, f_q) \quad (5)$$

Here $D(\cdot)$ is the data term that encodes the soft epipolar line constraint:

$$D_p(f_p) = \frac{1}{n-1} \sum_{i=2}^n d(\text{proj}_i(p, f_p), c_i(\text{proj}_i(p, f_p))) \quad (6)$$

where $\text{proj}_i(p, f_p)$ is the projection of the 3-D point (p, f_p) onto the i^{th} view, $c_i(r)$ is the point on the 2-D centerline of the i^{th} view that is closest to a given 2-D point r , and $d(p, q) = \min(|p-q|, K_l)$ for some constant K_l . The cap K_l (set to 20) is to make the distance penalty robust when the corresponding stereo point is missing in some views. A kd-tree structure [15] is implemented for an efficient search of the point $c_i(r)$ for any point r . It is clear that while the data term favors 3-D points that are closer to the epipolar lines, no hard epipolar line constraint is imposed. This property is crucial for the robustness of the reconstruction algorithm, especially when there is inaccuracies and incompleteness in the extracted 2-D centerlines. In addition, soft epipolar line constraint allows the smoothness regularization to be optimized up to the accuracy of a small depth increment ΔL in 3-D (further details are given later), which helps to improve the smoothness of the reconstructed coronary tree in 3-D.

The smoothness term $V(\cdot)$ involves the notion of neighborhood N :

$$N = \{(p, q), p \in P, q \in P, |p_x - q_x| + |p_y - q_y| = 1\} \quad (7)$$

$$\text{and } V_{p, q}(f_p, f_q) = \begin{cases} \min(|f_p - f_q|, k_2) & f_p, f_q \notin B, \\ \min(|f_p - f_q|, k_3) & \text{otherwise} \end{cases} \quad (8)$$

where B denotes the union of branching points that have three or more neighboring points on the 2-D centerline P in its eight-connection neighborhood. Higher smoothness penalty is imposed between non-branching points by $k_2 > k_3$ ($k_2 = 50, k_3 = 15$ in our algorithm). It is important to allow for discontinuity at a branching point because it may be the intersection of two vessels at different depth. Meanwhile reasonably high smoothness penalty for non-branching is necessary in order to achieve a smooth 3-D reconstruction. Furthermore, $V_{p, q}(\cdot)$ is a metric for any (p, q) , satisfying the necessary condition for α -expansion move of GCs optimization.

Consider a given input f and a label α , another configuration f' is defined to be within a single α -expansion of f when all pixels $p \in P$ either $f'_p = f_p$ or $f'_p = \alpha$. The critical step in the minimization of the energy function E in Eq. 5 by GCs is to locally decrease the energy function E for a given configuration f and a label α by finding the f'_p , among all α -expansions of f , that minimizes the energy function E . It has been shown that global searching of f'_p for a given f and α can be done efficiently by

constructing a directed graph using the data term and smoothness term defined in Eq. 6 and 7, and solving the maximum flow problem (see [9] for details). This local improvement is run over all the labels in L either in a fixed order or at random. If there is some label α that decreases the energy E , another circle of local improvements is repeated over all the labels. Otherwise the optimization process stops. It is shown [9] that experimentally the computational time increases only linearly with the number of labels in L , implying that a large number of labels (hence small depth increment ΔL) can be searched within tractable time. In comparison, most existing methods use dynamic programming for global optimization, whose time complexity increases quadratically with the average number of candidate positions per pixel. Hard epipolar line constraint hence has to be imposed in order to make the computation tractable. In our algorithm the number of labels was set to 256 and the increment ΔL was about 0.5mm. Note that the output E_{output} of Graph Cuts α -expansion move is a local minimum within a known factor of the global minimum: $E_{output} \leq 2 k_2 E_{optimal}$.

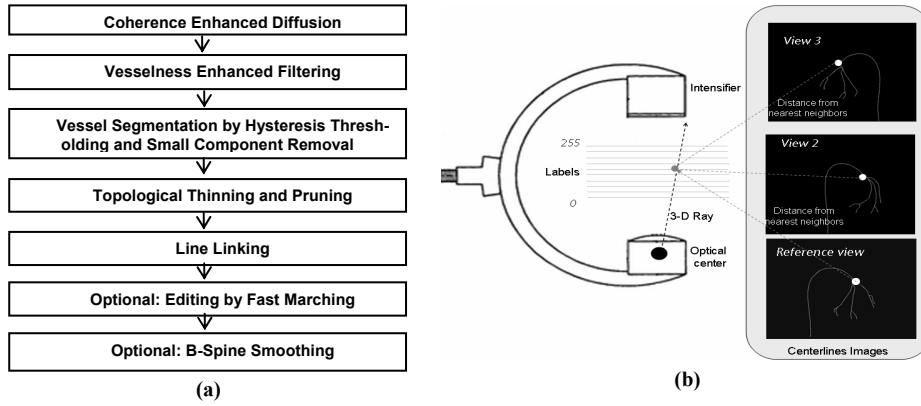


Fig. 3. Block diagram of 2-D coronary artery centerline extraction (a) and schematic view of multi-view matching using GCs for 3-D reconstruction (b). The intersection of the 3-D ray and a labeled plane is re-projected onto the other two views in (b).

3 Experiments

A synthetic 3-D heart phantom was designed to incorporate basic LAD, LCX and RCA coronary branches (Fig.4.a). 2-D projections of the 3-D centerline phantom were simulated using known projection matrices on 2-D images (512x512). Different numbers of views were used for reconstruction, and the angle between two consecutive views was determined in order that approximately the same total angulation was covered in each case. The 2-D re-projection error was averaged over ten views that were distinct from the views used for reconstruction. In Table 1, the 3-D error was relatively large when only two views were used, and became less than 1mm when five or more views were utilized, demonstrating the advantage of exploiting more views for reconstruction. The accuracy was relatively high (sub-millimeter), and the execution time increased only slightly with the increasing number of views used. 3-D reconstruction is very challenging for any optimization method when the number of views is limited and with wide baseline, even for motion-free and not-complicated structures. The result therefore demonstrates the strength and efficiency of GCs optimization.

The proposed method was further experimented on a porcine data (620x480) and a human data (512x512) acquired by Siemens Axiom Artis System. Cardiac phase was estimated from ECG signal. Breathing motion was negligible for the human data acquired during breathing holding, and was observed to be minimal for the porcine data, which otherwise need to be compensated by 2-D translation using bifurcation points. 2-D centerline extraction was fully automatic on the human data (Fig.1) and semi-automatic editing was needed for the porcine data (Fig.2), which could be accomplished reliably within a few minutes for trained users, and intra-observer variability was observed to be minimal due to the fact that user input was indeed minimal (essentially the end points only). CED was observed to improve the vessel segmentation result noticeably (Fig.2.c). Five projections were used for fully automatic reconstruction, and the reconstructed 3-D centerlines were re-projected onto the other view at the same cardiac phase that was not used for reconstruction. The reconstructed 3-D centerlines seem to be highly smooth (Fig.5.a), and their projections overlay reasonably well with the vessels in the X-ray images (Fig.5.b). The 2-D re-projection error for a projected point (purple line) was defined as its distance to the closest point on the expert-identified centerlines (blue line) in Fig.5.b, and the mean error was 1.15 ± 1.01 mm and 1.22 ± 0.93 mm respectively. Typical running time was 12s on 2.13 GHz Intel Pentium M when using five views and 256 labels.

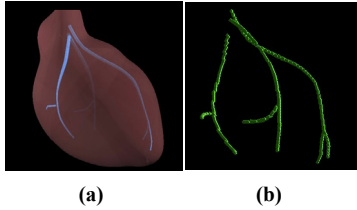


Fig. 4. A heart phantom (a) and reconstruction using five views (b).

Table 1. Validation of the proposed 3-D reconstruction method using a synthetic phantom.

| # of views / angle between views | Execution time (s) | Mean 2-D error (pixel) | RMS 3-D error (mm) |
|----------------------------------|--------------------|------------------------|--------------------|
| 2/90 | 11.497 | 5.30 ± 15.80 | 2.67 ± 5.59 |
| 3/60 | 12.208 | 2.35 ± 7.99 | 1.20 ± 2.86 |
| 4/40 | 12.198 | 2.08 ± 6.60 | 1.01 ± 2.08 |
| 5/30 | 12.869 | 1.86 ± 5.21 | 0.83 ± 1.58 |
| 6/24 | 12.899 | 1.75 ± 4.56 | 0.83 ± 1.41 |
| 7/20 | 13.330 | 1.75 ± 4.80 | 0.84 ± 1.55 |

4 Discussion and Conclusion

A framework based on GCs optimization is presented for efficient multi-view symbolic reconstruction of coronary artery tree. The accuracy as reported from the phantom and patient studies seems promising, and the efficiency is significantly improved compared to other approaches reported in the literatures, ranging from a few to tens of minutes [5~8]. Visually good and smooth reconstruction is demonstrated. Further study is required for in-depth quantitative comparison of the proposed method with other approaches in generating a smooth 3-D reconstruction by utilizing soft-epipolar line constraint and small depth increment. The reconstructed 3-D symbolic model can be used to optimize the visualization, quantitative assessment of coronary lesion, and 3-D measure of intracoronary devices, and will be clinically evaluated. Future work consists of dynamic analysis of each artery from the symbolic reconstructions obtained for different cardiac phases (Fig.6). Furthermore, after the estimated motion is compensated throughout the angiography sequence, tomographic reconstruction can be applied to obtain the full vessel lumen model for stenosis analysis.

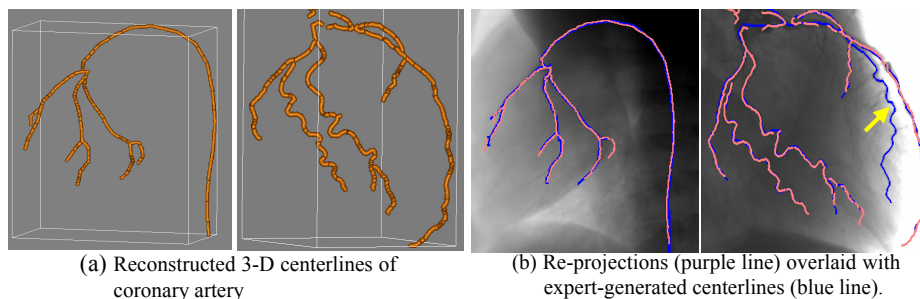


Fig. 5. Results for a porcine (left) and a human data (right). Note that for the human data, the vessel pointed by arrow is not visible in the reference view and hence is not reconstructed.

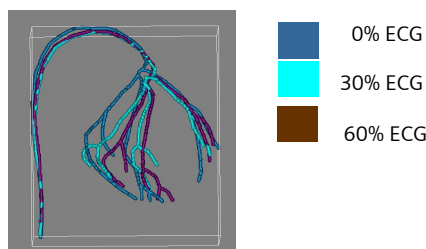


Fig. 6. Symbolic reconstruction for several cardiac phases.

References

1. Heart Disease and Stroke Statistics--2007 Update. A Report from the American Heart Association Statistics Committee and Stroke Statistics Subcommittee, *Circulation*, 2006.
2. R. Gollapudi, R.Valencia, S. Lee, G. Wong, P. Teirstein, M. Price, Utility of Three-Dimensional Reconstruction of Coronary Angiography to Guide Percutaneous Coronary Intervention, *Catheterization and Cardiovascular Interventions*, 69: 479-482, 2006.
3. T. Nguyen and J. Sklansky, "Reconstructing the 3-D Medial Axes of Coronary Arteries in Single-View Cineangiograms", *IEEE Trans. on Medical Imaging*, 13(1): 61-73, 1994.
4. AB Merle *et. al*, "3D Reconstruction of The Deformable Coronary Tree Skeleton from Two X-Ray Angiographic Views", *Computers in Cardiology*, 25: 757-760, 1998.
5. S.Y. Chen and J. Carroll, "3-D Reconstruction of Coroarny Arterial Tree to Optimize Angiographic Visualization", *IEEE Trans. on Medical Imaging*, 19(4): 318-336, 2000.
6. K. Sprague *et. al*, "Coronary X-ray Angiographic Reconstruction and Image Orientation", *Medical Physics*, 3(3): 707-718, 2006.
7. C. Blondel *et. al*, "Reconstruction of Coronary Arteries from A Single Rotational X-ray Projection Sequence", *IEEE Trans on Medical Imaging*, 25(5): 653-663, 2006.
8. S.Y. Chen *et. al*, "Kinematic and Deformation Analysis of 4-D Coronary Arterial Trees Reconstructed from Cine Angiograms", *Medical Imaging, IEEE Trans*, 22: 710-721, 2003.
9. Y. Boykov, O. Veksler, R. Zabih, "Fast Approximate Energy Minimization via Graph Cuts", *IEEE Trans on PAMI*, 23(11), 2001.
10. J. Weichert, "Multiscale Texture Enhancement", *Computer Analysis of Images and Patterns, Lecture Notes in Computer Science*, 970: 230-237, 1995.
11. A. Frangi, W. Niessen, K. Vincken, and M. Viergever, "Multiscale Vessel Enhancement Filtering", *Lecture Notes in Computer Science*, 1496: 130-137, 1998.
12. K. Palagyi, E. Sorantin, E. Balogh, A. Kuba, C. Halmi, B. Erdohelyi, K. Hausegger, "A Sequential 3D Thinning Algorithm and Its Medical Applications", *IPMI*, pp 409-415, 2001.
13. E. Mortensen, W. Barrett, "Intelligent Scissors for Image Composition", *ACM*, 1995.
14. J. Sethian, "Level Set Methods and Fast Marching Methods: Evolving Interfaces in Computational Geometry, Fluid Mechanics", *Computer Vision and Material Sciences*, 1998.
15. J. Friedman, J. Bentley, and R. Finkel, "An Algorithm for Finding Best Matches in Logarithmic Expected Time", *ACM Trans. on Mathematical Software*, 3(3):209-226, 1977.

IVUS elastography of complex human coronary plaques treated by directional atherectomy: Technical issues and preliminary clinical results

J r mie Fromageau¹, Yoshifumi Saijo², Roch Listz Maurice¹,
Marie-H l ne Roy Cardinal¹ and Guy Cloutier¹

¹ Laboratory of Biorheology and Medical Ultrasonics,
Research Center, University of Montreal Hospital, Montreal, Quebec, Canada, H2L 2W5.
² Department of Medical Engineering and Cardiology, Institute of Development, Aging and
Cancer, Tohoku University, Aobaku, Sendai 980-8575, Japan.

Abstract. *In vivo* IVUS elastography of human coronaries corroborated by histology is presented for the first time. Before elastogram calculation, the pre-processing included the detection of the vessel wall and global IVUS catheter rotation compensation. The pre-processing improved the quality of elastograms, particularly the correlation between consecutive radio-frequency IVUS frames was increased and the variance of elasticity maps decreased. Peak-systolic and end-diastolic strains were estimated from radial elastograms of plaques. Strain values with maximum occurrence at peak-systole and end-diastole were respectively linked with the presence of inflammation (CD68) and patient vulnerability objectively defined by the presence of calcium, lipid, smooth muscle cells, thrombi and CD68 marker of inflammation within excised plaques, medical history and patient's clinical condition.

Keywords: Elastography, Motion compensation, Vulnerable coronary plaques, Biomarkers of acute coronary syndrome, Atherosclerotic plaque image analysis.

1 Introduction

Intravascular ultrasound (IVUS) is an imaging technique that shows the blood vessel from the inside allowing to see the intima, media and adventitia with a good resolution. IVUS is widely used to image coronary arteries, especially the atherosclerotic pathology to determine the degree of stenosis and plaque burden. When a plaque ruptures, the formation of a blood clot within the vessel lumen can cause an acute coronary syndrome responsible of a heart attack, which is the leading cause of mortality in western countries [1]. Atheromatous plaques formed in the intima and the bulk of these lesions are typically made of soft lipid-rich necrotic cores, harder collagen-rich sclerotic tissues and often calcium. The main determinants leading to ruptured plaques are known to be a large lipid core covered by a thin fibrous cap and/or a dense infiltration of macrophages inside the fibrous cap [2].

IVUS elastography is a method that can estimate the strain distribution within vessel walls. Several studies showed the capability of IVUS elastography to identify plaque components, *in vitro* in human arteries [3] but also *in vivo* [4]. The major technical issue limiting the performance of IVUS elastography to characterize coronary arteries is the strong motion due to the heart beat. This motion changes the position of the IVUS catheter within the vessel lumen, and leads to rotation and out-

of-plane motion artefacts observed either on the B-mode or radio-frequency (RF) data. Several approaches were recently proposed to circumvent this difficulty [5,6] and an alternative is suggested in this manuscript. In addition, elastograms were computed with a robust algorithm known as the Lagrangian Speckle Model Estimator (LSME) [7]. This paper reports LSME elastograms applied to *in vivo* data obtained from 12 arteries before directional coronary atherectomy (DCA).

2 Methods

2.1 Clinical exams

Twelve patients (including two no re-flow cases and one perforation case) gave their written informed consent before being recruited. The research protocol was approved by the Review Ethical Committee of Sendai University. Before DCA, routine IVUS observations were performed and RF signals acquired at the same moment. IVUS scans were conducted with a Galaxy II® echograph (Boston Scientific, Natick, MA, USA) equipped with 40 MHz mechanically rotating probes. One sequence of 30 images was acquired for each patient with a fixed longitudinal position of the catheter within the maximum stenosis, at a frame rate of 30 images/s. RF signals were digitized with a CS8500 8-bits 500 MHz acquisition card (GAGE, Lockport, IL, USA). The DCA procedure consisted in removing the atheromatous plaque with a catheter designed for radial lesion cutting and excision. The excised specimens were fixed in 10% formalin and stained with normal Elastica-Masson's trichrome and CD68 monoclonal antibodies. These two staining gave information on the presence of calcium, lipid, smooth muscular cells, thrombi and inflammation. The vulnerability of the patient was determined based on histology analyses, medical history and clinical condition. Patient's vulnerability is a more generic condition than vulnerable plaque (vulnerable plaques are not the only culprit factors for the development of acute coronary syndromes, blood prone to thrombosis and myocardium prone to fatal arrhythmia also play a role) [8]. Table 1 gives an overview of the clinical classification of every patient and plaque components.

2.2 Data analysis

2.2.1 Image Segmentation. The first step of the data pre-processing consisted in segmenting IVUS images to detect vessel boundaries. The segmentation algorithm to detect the lumen and media-adventitia boundaries was based on a fast-marching model combining region and contour information [9]. Contours were validated by a cardiologist (Y.S.) before the next processing step. The artery wall (area between the detected lumen and media-adventitia boundary) defined the region of interest (ROI) that was used for image registration (Section 2.2.2).

2.2.2 Catheter Rotation Compensation. The second step consisted in a rigid motion compensation to remove the rotation observed between consecutive RF images. Each IVUS frame made of 256 radial lines in polar coordinates was unwrapped to obtain a matrix where rows correspond to propagation depths and columns to angles. A lateral translation in this representation thus corresponded to a rotation centered on the middle of the catheter in the Cartesian system.

Table 1: Systemic pressure in mmHg, patient vulnerability (0 = stable, 1 = at risk, 2 = high risk), and components of the plaque for each patient assessed on a binary scale: 0 = absence of the biomarker and 1 = presence. The level of inflammation was graded into three categories: 0 = no inflammation, 1 = medium level of inflammation and 2 = high level.

| Patient | Pressure (mmHg) | Patient vulnerability | Plaque components | | | | CD68 (level of inflammation) |
|---------|-----------------|-----------------------|-------------------|-------|---------------------|----------|------------------------------|
| | | | Calcium | Lipid | Smooth muscle cells | thrombus | |
| 0421KK | 138 / 72 | 0 | 0 | 1 | 1 | 1 | 0 |
| 0422MS | 124 / 68 | 0 | 0 | 0 | 1 | 0 | 1 |
| 0428NH | 132 / 80 | 1 | 0 | 1 | 1 | 0 | 0 |
| 0522KK | 158 / 88 | 0 | 0 | 0 | 0 | 0 | 0 |
| 0623AM | 142 / 78 | 1 | 0 | 1 | 1 | 1 | 2 |
| 0623YK | 152 / 92 | 2 | 0 | 1 | 1 | 0 | 2 |
| 0707SM | 138 / 82 | 0 | 0 | 0 | 1 | 0 | 0 |
| 0715RT | 114 / 76 | 2 | 1 | 1 | 1 | 1 | 2 |
| 0729TT | 162 / 94 | 0 | 0 | 0 | 0 | 0 | 0 |
| 0729YK | 128 / 74 | 1 | 1 | 1 | 1 | 1 | 1 |
| 0804ST | 168 / 94 | 2 | 1 | 1 | 1 | 1 | 2 |
| 0818KN | 132 / 88 | 2 | 0 | 0 | 1 | 0 | 0 |

The first 256 columns were selected as the initial image of the sequence. The second image was searched by lateral 2D correlations of ROIs and the rotation artefact was determined as the lateral shift with maximum correlation. Next, the new image compensated for rotation served as the initial image to align the third one and so on. A complete sequence was reconstructed with all images compensated for rotation. To quantify the improvement with this method, three parameters were evaluated before and after compensation: 1) the average correlation between RF images of the sequence, 2) the number of pixels in the whole sequence with correlations > 0.75 between images and 3) the mean from the whole sequence of the spatial variance of strain elastography images (which included variance due to mechanical heterogeneity within the ROI and tissue movement artifact).

2.2.3 Elastography algorithm. The LSME is described in details elsewhere [7]. The first step of this algorithm consisted in another local rigid registration on overlapping sub-windows (measurement windows – MWs) within the ROI that allowed compensating for potential residual translation movement using 2D cross-correlation analysis. For each MW, radial and circumferential displacement fields and correlation coefficient distributions were computed. The LSME is formulated as a nonlinear minimization problem that allows assessing the complete 2D-deformation matrix (Δ). In the context of IVUS elastography, Δ can mathematically be defined as [7] :

$$\Delta = \begin{bmatrix} \frac{\partial U_\varphi}{\partial \varphi} & \frac{\partial U_\varphi}{\partial r} \\ \frac{\partial U_r}{\partial \varphi} & \frac{\partial U_r}{\partial r} \end{bmatrix} \quad (1)$$

In this equation, U_r and U_φ are the radial and tangential displacement fields, respectively. The matrix component Δ_{rr} computed from consecutive RF images of the

IVUS sequence is the radial strain distribution that was analyzed in this study. The LSME numerical solution was reached using an inversion algorithm [10]. The size of 2D MWs was 350×20 pixels ($359 \mu\text{m} \times 28^\circ$), with 90% axial and lateral overlaps. LSME elastograms were filtered using a median filter (5×5 pixels).

For each elastogram, the spatial mean strain within the segmented ROI was estimated. A strain profile as a function of time (equivalent to a strain rate) was obtained by cumulating these average strain values. The strain profile permitted to detect easily the peak systolic and end diastolic moments of the cardiac cycle (Figure 2-b). Instantaneous strain histograms of the vascular wall (and plaque) were plotted at these two time periods. The primary strain was estimated as the peak of the histogram (Figure 2-d and f), and this value was used for quantitative analysis.

2.3 Statistical analyses

Quantitative variables are reported as mean \pm standard deviation. Statistical analyses were made with the SigmaStat software (version 3.1, Systat Software, San Jose, CA, USA). Analyses of variance were performed to detect any significant relation between primary strains (at peak systole and end diastole) and plaque components, patient vulnerability and status of inflammation. Spearman correlations were also calculated between primary strains, mean correlations of the RF sequence and systemic pressures.

3 Results

3.1 Global rotation compensation

The importance of the motion artifact was very different for each patient. The range of rotation within the cardiac cycle varied from 1.4° to 16.8° , see Table 2. For most patients, the rotation was not negligible, indeed IVUS scans of nine patients had a rotation superior to 5° . Moreover, for eight patients a cyclic rotation was clearly observed along the sequence, as depicted in Figure 1-a. The cyclic pattern was not obvious for four other patients because there was either an incomplete cardiac cycle available (scans of 1 s only) or a lack of correlation between consecutive images.

After rotation compensation, the three quality criteria defined earlier showed improvements, as presented in Figure 1-b. The improvement of each criterion in

percent was assessed as: $\left| \frac{C_{after\ compensation} - C_{before\ compensation}}{C_{before\ compensation}} \right| \times 100$, where C is one of the three criteria.

3.2 Elastogram analysis

One patient (0707SM) was excluded because of the lack of correlation between consecutive images of the sequence, and because the B-mode data clearly showed a longitudinal motion of the probe. Otherwise, for all other sequences, at least one elastogram at peak systole and another at end diastole could be estimated. Primary

strains at these two instants are given in Table 2. The statistical analysis showed that patient's vulnerability could be detected by the end-diastolic primary strain (0.08 ± 0.04 % when not vulnerable, 0.27 ± 0.15 % for patients at risk and 0.05 ± 0.05 % for patients at high risk, $p < 0.05$). Moreover, the inflammation status was linked with the peak-systolic primary strain (0.005 ± 0.08 % for no inflammation, -0.33 ± 0.07 % for medium level of inflammation and -0.03 ± 0.07 % for high level of inflammation, $p < 0.005$). Deformations were not linked with the systemic pressure, neither to a better correlation of the data ($p > 0.1$ for all cases). On the other hand, systolic and diastolic strains could not give information on the presence of any of the plaque components. Figure 2 presents examples of data processed to obtain results of Table 2.

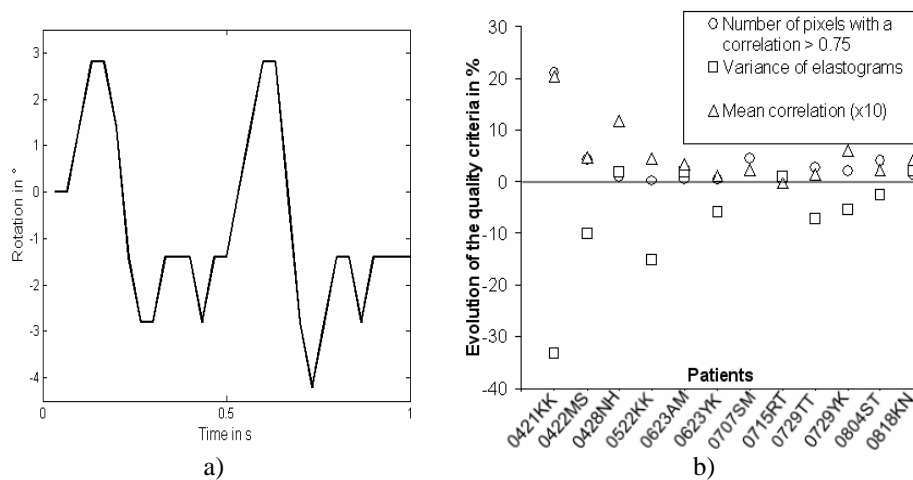


Figure 1: a) Estimation of the catheter rotation with respect to the first frame (patient 0422MS). A cyclic pattern of rotation in synchronicity with the cardiac beat is identified. b) Evolution of the three quality criteria after rotation compensation. A value close to zero indicates no improvement due either to the failure of the registration algorithm or absence of motion artifacts. The number of pixels with a high correlation and the mean correlation increased following registration, whereas the mean variance of elastograms decreased. The best improvement was observed for the first patient (0421KK) where the number of pixels with a high correlation increased by 21%, the mean correlation of the sequence increased by 2% and variances of elastograms decreased by 33%. Note that the mean correlation was multiplied by 10 to enhance visualization.

4 Discussion

The global rotation compensation improved significantly the quality of several sequences. Visually the arterial wall appeared more stable over time, and quantitatively the three quality criteria were improved. Typically, the efficacy of the rotation compensation could be predicted by the mean correlation between consecutive RF frames before compensation. Indeed, when the mean correlation was high, the rotation motion was small and the compensation did not improve appreciably elastograms. At the opposite, for cases with a small mean correlation

before compensation, the motion artifact was important and not due to a single rotation but also to out of plane motion. In such circumstances, the rotation compensation was not very efficient. Best results were obtained for intermediate levels of correlation before compensation.

Table 2: Summary of the different parameters measured for each patient.

| Patient | Rotation [min, max] | Cyclic behavior | Mean correlation of the sequence after compensation | End-diastolic primary strain in % | Peak-systolic primary strain in % |
|---------|------------------------|--------------------|---|---|---|
| 0421KK | [-15.4°, 1.4°] | Uncertain | 0.80 | 0.0840 | -0.0120 |
| 0422MS | [-4.2°, 2.8°] | Yes | 0.81 | 0.0960 | -0.2800 |
| 0428NH | [-1.4°, 2.8°] | Uncertain | 0.78 | 0.1400 | 0.0960 |
| 0522KK | [-1.4°, 7°] | Yes | 0.84 | 0.1200 | -0.0600 |
| 0623AM | [-9.8°, 0°] | Uncertain | 0.88 | 0.2200 | 0.0360 |
| 0623YK | [-4.2°, 2.8°] | Yes | 0.88 | 0.0240 | 0.0000 |
| 0707SM | [0°, 8.4°] | No | 0.40 | X | X |
| 0715RT | [-1.4°, 0°] | Yes | 0.84 | 0.1300 | -0.0480 |
| 0729TT | [-2.8°, 1.4°] | Yes | 0.78 | 0.0240 | 0.0720 |
| 0729YK | [-7°, 0°] | Yes | 0.83 | 0.4400 | -0.3800 |
| 0804ST | [0°, 11.2°] | Yes | 0.80 | 0.0120 | -0.1200 |
| 0818KN | [-5.6°, 2.8°] | Yes | 0.82 | 0.0360 | -0.0720 |

RF data in this study were of good quality, with the catheter often located near the center of the lumen, and with the principal motion artifact being a centered rotation. Nevertheless, a more complex motion compensation algorithm could be required for complex motion artifacts. For example, Leung *et al.* combined a global rotation with a local block matching as a pre-processing of their strain estimation [11]. In the present study, the rotation compensation algorithm did not try to reach a subpixel resolution by performing interpolation to optimize detection of maximum correlation. Indeed, a 2D local block matching was performed on segmented plaques as a first step before applying the LSME to refine afterward the motion compensation on every MW.

For most patients (11/12), strain images could be calculated on the whole vessel wall, with coherent and reproducible elastograms. Numerical analyses showed that primary strains estimated at different instants of the cardiac cycle were significantly linked with the vulnerability of the patient and to the inflammation status. De Korte *et al* [12] also found a similar relation between the presence of macrophages and high strain peaks on their palpograms. According to them, it could refer to the presence of active macrophages, causing plaque weakening. Our observations revealed that primary peak-systolic strains were statistically higher in plaques with a medium level of inflammation (grade 1). Similarly, higher primary end-diastolic strains were measured for patients with moderate vulnerability (grade 1). As these deformations were not linked with the plaque components, we still need to elucidate which clinical factor explains these results. On strain images, regions with different elasticity were detected, as in Fig. 2, but a careful attention at strain heterogeneity and location within the plaque were not yet addressed.

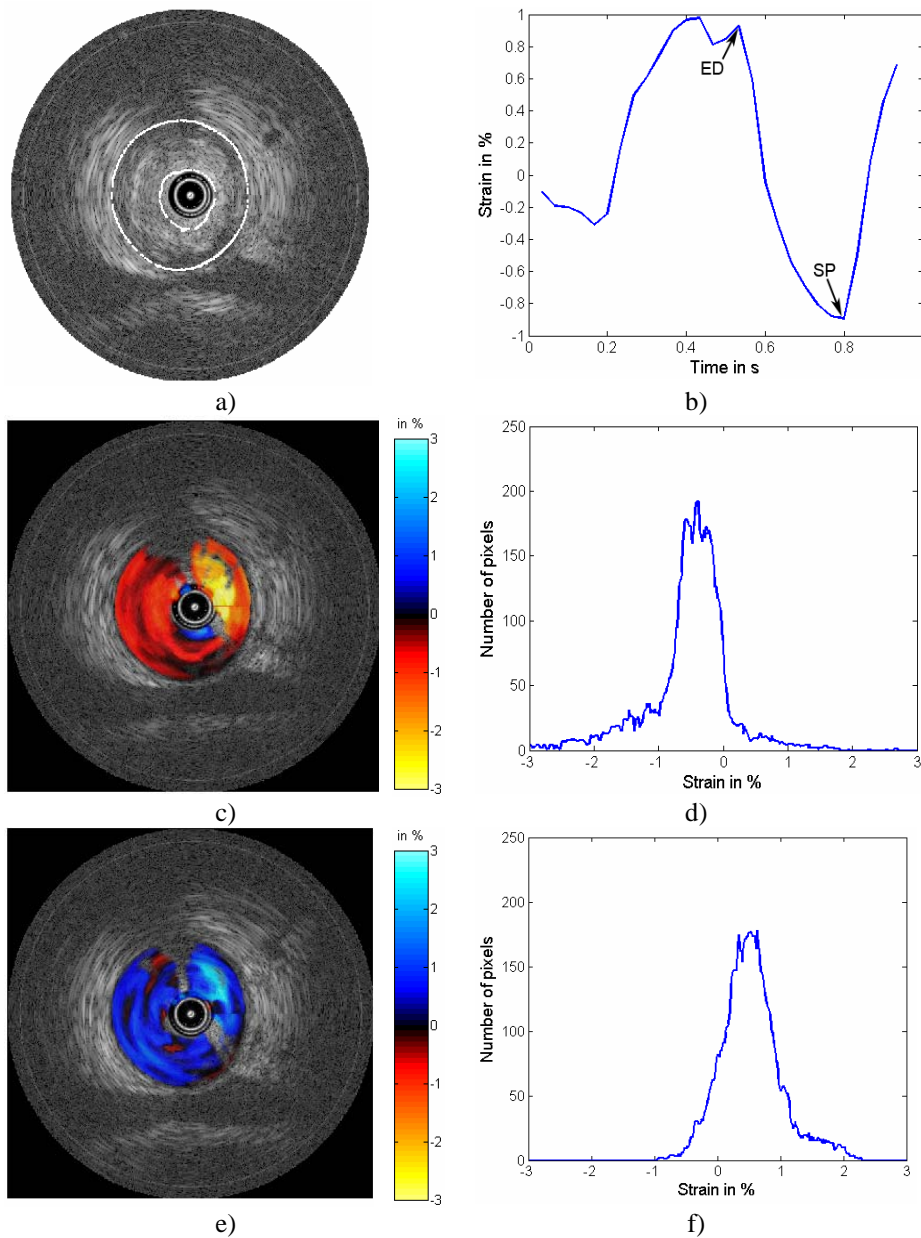


Figure 2: Example of analysis for patient 0729YK. a) B-mode image with contour detection highlighting the ROI. b) Cumulated mean strain within the segmented plaque as a function of time. The cardiac cycle can be detected (ED is end diastole and SP is systolic peak). c) Peak-systolic elastogram and d) corresponding histogram. The peak-systolic primary strain was defined as the peak of this histogram. e) End-diastolic elastogram and corresponding histogram. The end-diastolic primary strain was defined as the peak of this histogram. Note that an area with large deformations

($\approx \pm 3\%$) is identified on these elastograms close to the vessel lumen, which may be indicative of a necrotic core (lipid pool) of a vulnerable plaque.

5 Conclusion

In this study, we performed for the first time *in vivo* vascular elastography corroborated with histology. A global image rotation compensation and rigid registration of measurement windows were performed to increase the quality of IVUS sequences and that of elastograms. The study showed that peak-systolic and end-diastolic primary strains were significantly linked with the status of inflammation and patient's vulnerability, respectively.

Acknowledgments. This work was supported by the Natural Sciences and Engineering Research Council of Canada (#138570-6). Dr Cloutier is recipient of the National Scientist award of the Fonds de la Recherche en Santé du Québec (2004-2009).

References

1. World Health Organization: Measurement and health information, causes of death. <http://www.who.int/entity/healthinfo/statistics/bodgbdeathdalyestimates.xls> (2004).
2. Fuster V. *et al.*, Atherothrombosis and high-risk plaque: Part I: evolving concepts. *J. Am. Coll. Cardiol.* 46, pp. 937-954 (2005).
3. Maurice R. L. *et al.*, On the potential of the Lagrangian speckle model estimator to characterize atherosclerotic plaques in endovascular elastography: in vitro experiments using an excised human carotid artery. *Ultrasound Med. Biol.* 31, pp. 85-91 (2005).
4. Schaar J. A. *et al.*, Incidence of high-strain patterns in human coronary arteries: Assessment with three-dimensional intravascular palpography and correlation with clinical presentation. *Circulation.* 109, pp. 2716-2719 (2004).
5. Danilouchkine M. G. *et al.*, Accuracy in prediction of catheter rotation in IVUS with feature-based optical flow - A phantom study. *IEEE Trans. Inform. Tech. Biomed.* 12, pp. 356-365 (2008).
6. Hernández A. *et al.*, Vessel structures alignment by spectral analysis of IVUS sequences. *MICCAI 2006 Workshop Comp. Vis. Intravasc. Intracard. Imag.* pp. 30-37 (2006).
7. Maurice R. L. *et al.*, Adapting the Lagrangian speckle model estimator for endovascular elastography: Theory and validation with simulated radio-frequency data. *J. Acoust. Soc. Am.* 116, pp. 1276-1286 (2004).
8. Naghavi M. *et al.*, From vulnerable plaque to vulnerable patient: A call for new definitions and risk assessment strategies: Part I. *Circulation.* 108, pp. 1664-1672 (2003).
9. Roy Cardinal M.-H. *et al.*, Intracoronary 3D ultrasound image segmentation: application to pre- and post-intervention data. *MICCAI 2006 Workshop Comp. Vis. Intravasc. Intracard. Imag.* pp. 179-186 (2006).
10. Maurice R. L. *et al.*, Non-invasive high-frequency vascular ultrasound elastography. *Physics Med. Biol.* 50, pp. 1611-1628 (2005).
11. Leung K. Y. *et al.*, Motion compensation for intravascular ultrasound palpography. *IEEE Trans. Ultrason. Ferro. Freq. Control.* 53, pp. 1269-1280 (2006).
12. de Korte C. L. *et al.*, Identification of atherosclerotic plaque components with intravascular ultrasound elastography in vivo: a Yucatan pig study. *Circulation.* 105, pp. 1627-1630 (2002).

Multiscale Optimization for the Fast-Marching Segmentation of Three-Dimensional Intravascular Ultrasound Images

Marie-Hélène Roy Cardinal^{1,2}, Gilles Soulez^{3,4}, Jean-Claude Tardif^{5,6},
Jean Meunier^{2,7}, and Guy Cloutier^{1,2,4}

¹ Laboratory of Biorheology and Medical Ultrasonics (LBUM), University of Montreal Hospital Research Center, Canada, roycarmh@iro.umontreal.ca, guy.cloutier@umontreal.ca, ² Institute of Biomedical Engineering, University of Montreal, ³ Department of Radiology, University of Montreal Hospital, ⁴ Department of Radiology, Radio-Oncology and Nuclear Medicine, University of Montreal, ⁵ Department of Medicine, University of Montreal, ⁶ Montreal Heart Institute, Canada, ⁷ Department of Computer Science, University of Montreal.

Abstract. Intravascular ultrasound is a medical imaging technique that produces cross-sectional images of the vascular wall as a catheter is pulled-back inside blood vessels. A multiscale 3D fast-marching method with minimal user interaction is presented for the detection of the lumen and external vessel wall boundaries. The proposed segmentation framework is based on a combination of local and global image features. The method was applied to 5 in-vivo pullback datasets of 678 images on average acquired on diseased femoral arteries. No difference was found between the contour area measurements of the lumen and external vessel wall from the segmentation results and manually drawn contours by experts. Area differences between segmentation and validation contours of $-1.9 \pm 8.7 \%$ and $-1.8 \pm 2.5 \%$ were respectively found for the lumen and the external vessel border. The multiscale optimization of fast-marching provides accurate results with 40 % less computation.

1 Introduction

Intravascular ultrasound imaging (IVUS) provides high-resolution axial images of the lumen and vessel wall as a catheter is pulled-back inside blood vessels. IVUS imaging has been used in several studies that evaluated the effect of therapies on atherosclerosis [1]. IVUS datasets provide information on the lumen cross section area, the wall thickness and on the length, volume and position (concentricity or eccentricity) of the lesion. Moreover, IVUS is becoming a tool of choice in the treatment of peripheral disease [2]. IVUS acquisitions often contain several hundreds of images that are subject to artifacts such as ultrasonic speckle, catheter ring-down or calcification shadows. Automated segmentation of the IVUS series is thus desirable for the analysis of the voluminous datasets acquired in clinical trials evaluating the progression and regression of the atherosclerotic disease.

Recent works in IVUS image segmentation include models that are based on edge information. Active contour models were considered with implementations based on gray level gradient with automatic initialization [3] and gradient vector flow of canny edge maps [4]. A graph search algorithm implemented using gray level properties and first- and second-derivative gradient filters was also described [5]. Another edge based segmentation model relies on a multi-agent method [6].

A fast-marching method for the segmentation of IVUS images based on the intensity gradient and probability density functions (PDFs) of the vessel wall components was proposed in [7]. An interactive initialization procedure was used for the segmentation. The aim of the current work was thus to identify the luminal and outer vessel (or external elastic membrane, EEM) borders on IVUS sequences of diseased femoral arteries with an optimized segmentation method where the initialization and segmentation computation load is reduced with the multiscale optimization of the fast-marching method.

2 Fast-Marching Segmentation and Multiscale Optimization

The fast-marching method, a particular case of the level-set model, was developed to follow the evolution of an interface propagating under a unidirectional speed function F [8]. In the segmentation framework, the detected boundary is defined as the propagating interface final position [9]. The speed function is defined in terms of image or shape features. When the propagating front meets the boundaries of the image objects, the velocity should tend toward zero to stop the segmentation. The evolution of the contour is expressed as a function of the arrival time T of the front at a point in the image. The T function satisfies Eq. (1), stating that the arrival time difference between two adjacent points increases as the velocity of the contour decreases.

$$|\nabla T| F = 1 \quad . \quad (1)$$

For the segmentation of IVUS images, the luminal and EEM borders must be identified. Both contours were detected in parallel using a multiple interface extension of the fast-marching algorithm [10]. For this particular case, a boundary is defined as the meeting position of two fronts propagating in opposite directions. Each of the multiple interfaces was propagated according to a speed function defined in terms of the image gradient and the PDF of the corresponding wall component [7, 11]. The propagation speed F_m of interface m is given by :

$$F_m(i, j, k) = \alpha F_{m,pdf}(i, j, k) + \beta F_{m,grad}(i, j, k). \quad (2)$$

where $F_{m,pdf}(i, j, k)$ and $F_{m,grad}(i, j, k)$ are the speed function components, at position (i, j, k) in the IVUS image volume I . They are respectively defined in terms of the PDF and intensity gradient components; α and β are the weights of the velocity components.

A multiscale optimization of the fast-marching method was used to provide large exploration regions to the propagating fronts with less computation. The segmentation results of a lower resolution representation of the data were mapped into the next level of resolution. These mapped results were used to initialize the front propagation at this higher resolution level. At a resolution level l , a pixel represents a $2^l \times 2^l$ block of pixels from the original image. To overcome this lost of information, a PDF-based energy function calculated using the whole data at each resolution was proposed in [12] for a multiscale deformable template. The fast-marching speed function was adapted using this approach. The PDFs and image gradient computed on the original dataset were thus used at each scale.

To obtain a multiscale fast-marching method without information loss, the velocity function of Eq. (2) was thus redefined as :

$$F_m^l(i, j, k) = \alpha F_{m, pdf}^l(i, j, k) + \beta F_{m, grad}^l(i, j, k), \quad (3)$$

where $F_{m, pdf}^l(i, j, k)$ and $F_{m, grad}^l(i, j, k)$ are the speed function components of the pixel positioned at (i, j, k) in the IVUS image volume I_l at resolution level l . The multiscale velocity function components were defined as :

$$F_{m, pdf}^l(i, j, k) = \frac{1}{N_\nu} \sum_{q \in \nu} \sum_{s \in b_q^l} p_m(y_s). \quad (4)$$

$$F_{m, grad}^l(i, j, k) = \frac{1}{1 + \sum_{s \in b_q^l} |g_\sigma(y_s)|}. \quad (5)$$

where ν is the set of the N_ν 3D neighbors of the pixel positioned at (i, j, k) ; b_q^l is the $2^l \times 2^l$ block of pixels of the highest resolution dataset corresponding to the point q ; y_s is the gray level value of the pixel positioned at s in the original dataset; and $g_\sigma(y_s)$ is the gaussian filtered (with standard deviation σ) gradient g at pixel y_s .

With these speed functions, the occurring probability of the point q in the image volume I_l , when the propagation is done at level l , was replaced with the average of the occurring probabilities of the $2^l \times 2^l$ block of pixels from the original dataset. Similarly, the gradient at q was replaced with the average value of the pixel block gradient. The initial resolution level was set to $l = 2$.

Pre-processing. The IVUS images were converted in the polar format and all processing was performed in this format. The pre-processing calculations involved the catheter artifact detection and removal, the estimation of the PDF parameters and the intensity gradient computation.

The pixels near the catheter with gray level values that correlated highly (with $r > 0.9$) through frames across the whole pullback were labeled as being part of the ring-down artifact and subtracted from the 2D IVUS frames. This catheter related artifact was detected for each dataset because it is specific to the catheter used to scan a given patient.

The speed function of Eq. (4) uses the occurring probability of the gray level values in the different vessel component distributions calculated with $p_m(y_s)$.

The gray level PDF of the whole IVUS pullback was modeled as a mixture of Rayleigh PDFs [13] where each distribution corresponds to a vessel structure (lumen, vessel wall, surrounding tissues). The PDF mixture $p_{Y|\Theta}$ that contains M Rayleigh distributions with parameter $\Theta = \{(\omega_m, a_m^2)\}_{m=1}^M$, was defined by:

$$p_{Y|\Theta}(y_s | \Theta) = \sum_{m=1}^M \omega_m p_m(y_s | a_m^2) \quad (6)$$

where ω_m is the proportion of the m^{th} component of the mixture so that $\sum_{m=1}^M \omega_m = 1$; a_m is the parameter of the Rayleigh distribution p_m . The Rayleigh distribution is defined by:

$$p_Y(y_s; a^2) = \frac{y_s}{a^2} \exp\left(-\frac{y_s^2}{2a^2}\right) \quad (7)$$

with $y_s > 0$ and the variance $\sigma^2 = a^2(4 - \pi)/2$. The mixture parameter Θ was estimated with the expectation-maximization algorithm (EM) [14]. A detailed description of the estimation of a Rayleigh PDF mixture is provided in [11].

The speed function of Eq. (5) uses the gradient that was computed along the radial lines using a radial difference operator.

Initialization. The initialization procedure was divided in two steps: automatic lumen initialization and interactive EEM initialization. All initial contour computations were performed on longitudinal views (LViews) of the IVUS volume. The initialization procedure was based on the method described in [7]. With the multiscale fast-marching, only LViews need to be initialized whereas cross-sectional images were also necessary in [7].

Four LViews were selected at regularly spaced angles over 360 degrees. The lumen longitudinal contours were automatically detected: they were positioned outside the catheter and grown to maximize the lumen likelihood computed according to the lumen PDF p_{Lum} :

$$L_{Lum}(i, j, k) = \frac{1}{N_{\nu 1}} \sum_{s \in \nu 1} \log p_{Lum}(y_s) \quad (8)$$

where $\nu 1$ is the set of the $N_{\nu 1}$ pixels inside the contour. The longitudinal EEM contours were then interactively detected. Smooth contours surrounding the previously found lumen were grown radially to maximize the EEM log-likelihood :

$$L_{EEM}(i, j, k) = \frac{1}{N_{\nu 1}} \sum_{s \in \nu 1} \log p_{inEEM}(y_s) + \frac{1}{N_{\nu 2}} \sum_{s \in \nu 2} \log p_{outEEM}(y_s) + \frac{1}{N_{\nu 3}} \sum_{s \in \nu 3} g_{\sigma}(y_s) . \quad (9)$$

where $\nu 1$ and $\nu 2$ are sets of $N_{\nu 1}$ and $N_{\nu 2}$ pixels in regions of interest respectively inside and outside the vessel boundary ; $\nu 3$ is the set of $N_{\nu 3}$ pixels on the boundary; $p_{inEEM}(y_s)$ and $p_{outEEM}(y_s)$ are the estimated occurring probabilities of

y_s in the tissue regions inside and outside the EEM, respectively; and $g_\sigma(y_s)$ is the value of the filtered gray level gradient at y_s .

These automatically detected EEM contours were then proposed to the user and corrected if necessary. The initial longitudinal contours were directly converted into propagation regions for the fast-marching segmentation [11].

3 In-Vivo IVUS Data

A total of 5 in-vivo IVUS pullbacks of 600 to 989 frames from diseased superficial femoral arteries were acquired with a Volcano Therapeutics IVUS imaging system (In-vision gold, California, USA) using a 20 MHz transducer. Images of size 10 x 10 mm were digitized on 384 x 384 pixel matrices and stored using the DICOM standard. The acquisition was done at a 10 images / sec frame rate and the catheter pullback velocity was set to 1 mm / sec.

The multiscale segmentation method was applied to the in-vivo IVUS datasets. For validation purpose, the segmentation results were compared with manually traced contours from two experts on 1 every 10 frames. Results were also compared with an implementation of the fast-marching without the multiscale optimization. The average and maximum (or Hausdorff) point to point contour distances, area and percentage of area difference were calculated for the lumen and EEM boundaries.

A two way analysis of variance was carried out for the average and Hausdorff distances, and for the area measurements; multiple pairwise comparisons with Tukey tests were performed. The accuracy of the segmentation was compared to the inter-user variability. All statistical analyses were performed with SigmaStat, version 3.11, Systat Software Inc., San Jose, California, USA.

4 Results

Typical segmentation results for the multiscale 3D fast-marching method combining PDFs and gradient are shown in Fig. 1. The lumen and EEM boundaries are presented for cross-sectional IVUS images from pullbacks acquired on 4 different patients. The segmentation, including the interactive initialization, was performed in 1.1 sec / image instead of 1.7 sec / image for the implementation of the algorithm without the multiscale optimization corresponding to a 40 % improvement of the processing time.

Table 1 shows the average and Hausdorff distances between the detected contours and the validation boundaries. The area measurements and percentage of area difference are also shown in Table 1. No difference was found between the area measurements computed from the detected contours and the experts' validation boundaries; small area differences lower than -1.9% were obtained. However, statistically significant differences for the average and Hausdorff distances were found ($p < 0.01$) for the lumen and EEM.

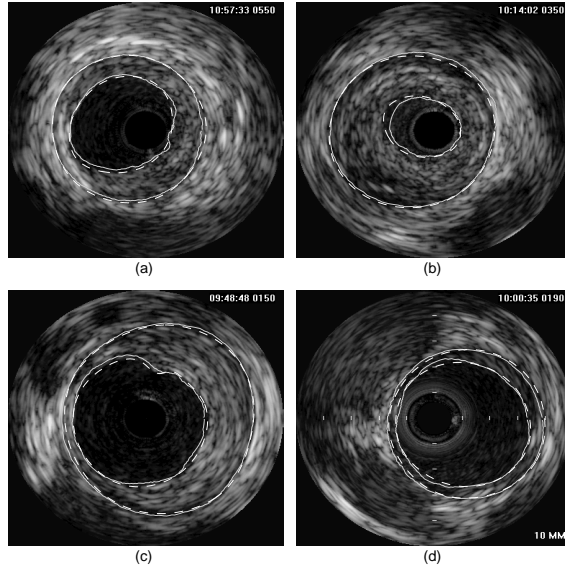


Fig. 1. Typical intravascular ultrasound cross-sectional images, corresponding segmentation results (solid contours) and manually traced contours by one of the experts (dashed contours). The lumen and EEM detected boundaries are drawn.

Table 1. Segmentation accuracy: average and Hausdorff distances; and area measurements of manual segmentation and detected boundaries.

| | Man-Man | AutoMulti-Man | Auto-Man |
|-------------------------------|-----------|---------------|-----------|
| Lumen AD (mm) | 0.08±0.03 | 0.12±0.06 | 0.10±0.05 |
| EEM AD (mm) | 0.05±0.03 | 0.09±0.03 | 0.07±0.03 |
| Lumen HD (mm) | 0.20±0.10 | 0.37±0.20 | 0.34±0.18 |
| EEM HD (mm) | 0.14±0.08 | 0.23±0.09 | 0.22±0.12 |
| Lumen Area Difference (%) | -5.1±4.2 | -1.9±8.9 | 0.7±8.0 |
| EEM Area Difference (%) | -0.4±2.5 | -1.8±2.5 | -0.07±2.7 |
| | Manual | AutoMulti | Auto |
| Lumen Area (mm ²) | 17.9±5.6 | 17.4±5.2 | 17.9±5.4 |
| EEM Area (mm ²) | 29.4±5.1 | 28.9±5.2 | 29.4±5.1 |

Man-Man shows the difference metrics between the manually traced contours of the two experts, AutoMulti-Man and Auto-Man shows the difference between the manual boundaries and the segmentation results respectively with and without the multiscale optimization. AD is the average distance; HD is the Hausdorff distance. Lumen and EEM areas show the average areas of the experts and segmentation contours with (AutoMulti) and without (Auto) the multiscale optimization. The pixel size is $26 \times 26 \mu\text{m}^2$. Statistically significant differences ($p < 0.01$) were found for the lumen and EEM between the Man-Man and AutoMulti-Man, between the Man-Man and Auto-Man and between the AutoMulti-Man and Auto-Man columns for the AD and HD.

5 Discussion

A multiscale optimization of the fast-marching method based on the vessel component PDFs and gradient was presented for the segmentation of IVUS images. A qualitative examination of the typical results of Fig. 1 reveals that the lumen and EEM boundary were close to the manually drawn contours. Accurate segmentation results were found for different types of plaque: a plaque with a brighter section (Fig.1 (a)), a large plaque (Fig.1 (b)), an irregular eccentric plaque (Fig.1 (c)); or for a thin hypoechogenic wall (Fig.1 (d)).

A quantitative evaluation of the segmentation accuracy was performed in Table I. It shows that the average and maximum point to point distances between the detected and manually traced boundaries were higher than the inter-user variability. However, these differences correspond to variations close to the boundaries since no difference was found between the area measurements and small percentages of area differences of -1.9 % and -1.8 % were obtained for the lumen and EEM, respectively. These values are in the range of the experts' variability of -5.1 % and -0.4 % for the lumen and EEM, respectively. The area measurements are important since they are used in the computation of the stenosis percentage, lumen and wall volumes, wall thickness, and plaque burden to evaluate the atherosclerotic disease. In [4], percentages of area differences, for the lumen and EEM respectively, of 11.09% and 4.98% for the interactive version of their active contours and of 10.95% and 7.27% for their automatic segmentation that are higher than those achieved with the multiscale fast-marching presented here were obtained. Absolute area differences were presented in [3, 5, 6], but it is difficult to compare with these methods since the measurements were made on coronary vessels that are smaller than femoral arteries.

The multiscale optimization provided accurate results on areas with less initialization computation. An improvement of 40 % of the computation time was feasible without sacrificing the accuracy since average and Hausdorff distances in a close range to those obtained without the multiscale optimization were computed and no difference was found for the area measurements (see Table 1). This was possible due to the fast coarse exploration of a wide area that was performed with the low resolution dataset to correct the rough initialization contours. At the higher resolution, a fine segmentation was performed in smaller propagation areas. The initialization was thus performed with LViews only. Without the multiscale scheme, a more precise initialization procedure must be performed on the cross-sectional frames and the segmentation must be done over a larger area of the highest resolution dataset hence the larger computation time.

These segmentation results on a small database of femoral artery IVUS images showed that the vessel wall boundaries were accurately detected with less computation. The usage of local and global image features such as the gray level gradient and PDFs in a fast-marching model provided a robust segmentation that was optimized in a multiscale framework. Further investigations on a larger IVUS database will provide a more precise evaluation of the multiscale optimization performances.

Acknowledgments. This work was supported by grants from the NSERC and the FRSQ. The salaries of G.C., G.S. and M.H.R.C. were partially supported by awards from the FRSQ.

References

1. Guédès, A., Tardif, J.C.: Intravascular ultrasound assessment of atherosclerosis. *Curr. Atheroscler. Rep.* **6**(3) (2004) 219–224
2. Lee, J.T., Fang, T.D., White, R.A.: Applications of intravascular ultrasound in the treatment of peripheral occlusive disease. *Semin. Vasc. Surg.* **19** (2006) 139–144
3. Giannoglou, G.D., Chatzizisis, Y.S., Koutkias, V., Kompatsiaris, I., Papadogiorgaki, M., Mezaris, V., Parissi, E., Diamantopoulos, P., Strintzis, M.G., Maglaveras, N., Parcharidis, G.E., Louridas, G.E.: A novel active contour model for fully automated segmentation of intravascular ultrasound images: In vivo validation in human coronary arteries. *Comput. Biol. Med.* **37** (2007) 1292–1302
4. Sanz-Requena, R., Moratal, D., García-Sánchez, D.R., Bodí, V., Rieta, J.J., Sanchis, J.M.: Automatic segmentation and 3d reconstruction of intravascular ultrasound images for a fast preliminar evaluation of vessel pathologies. *Comput. Med. Imag. Graph.* **31** (2007) 71–80
5. Koning, G., Dijkstra, J., von Birgelen, C., Tuinenburg, J.C., Brunette, J., Tardif, J.C., Oemrawsingh, P.W., Sieling, C., Melsa, S., Reiber, J.H.C.: Advanced contour detection for three-dimensional intracoronary ultrasound: A validation - in vitro and in vivo. *Int. J. Cardiac Imag.* **18** (2002) 235–248
6. Bovenkamp, E.G.P., Dijkstra, J., Bosch, J.G., Reiber, J.H.C.: Multiagent IVUS image interpretation. In: *SPIE Proceedings: Medical Imaging 2003: Image Processing*. Volume 5032., San-Diego, USA (2003) 619–630
7. Roy-Cardinal, M.H., Soulez, G., Tardif, J.C., Meunier, J., Cloutier, G.: Fast-marching segmentation of three-dimensional intravascular ultrasound images using region and contour information. Submitted (2008)
8. Sethian, J.A.: A fast marching level set method for monotonically advancing fronts. *Proceedings of the National Academy of Sciences of the United States of America* **93** (1996) 1591–1595
9. Malladi, R., Sethian, J.A., Vemuri, B.C.: Shape modeling with front propagation: A level set approach. *IEEE Trans. Pattern Anal. Machine Intell.* **17**(2) (1995) 158–175
10. Sifakis, E., Garcia, C., Tziritas, G.: Bayesian level sets for image segmentation. *J. Vis. Commun. Image R.* **13** (2002) 44–64
11. Roy-Cardinal, M.H., Meunier, J., Soulez, G., Maurice, R.L., Éric Therasse, Cloutier, G.: Intravascular ultrasound image segmentation: A three-dimensional fast-marching method based on gray level distributions. *IEEE Trans. Med. Imag.* **25**(5) (2006) 590–601
12. Mignotte, M., Meunier, J.: A multiscale optimization approach for the dynamic contour-based boundary detection issue. *Comput. Med. Imag. Graph.* **25**(3) (2001) 265–275
13. Wagner, R.F., Smith, S.W., Sandrik, J.M., Lopez, H.: Statistics of speckle in ultrasound B-scans. *IEEE Trans. Son. Ultrason.* **30**(3) (1983) 156–163
14. Dempster, A.P., Laird, N.M., Rubin, D.B.: Maximum likelihood from incomplete data via the EM algorithm. *J. Roy. Stat. Soc. B* **39**(1) (1977) 1–38

One-Class Acoustic Characterization Applied to Contrast Agent Detection in IVUS

E. Gerardo Mendizabal-Ruiz and Ioannis A. Kakadiaris

Computational Biomedicine Lab, Departments of Computer Science, Electrical & Computer Engineering, and Biomedical Engineering, University of Houston, Houston, TX

egmendiz@cs.uh.edu, ikakadia@central.uh.edu

<http://www.cbl.uh.edu>

Abstract. Intravascular ultrasound (IVUS) is currently the gold-standard for assessing the morphology of blood vessels and atherosclerotic plaques *in vivo*. IVUS combined with contrast agents in form of microbubbles is used for the detection of neovessels in plaques, which are markers of inflammation and plaque vulnerability. Recently, differential imaging techniques have been developed for the detection of microbubbles in stationary sequences. However, these methods work with the gray scale B-mode IVUS images and involve several preprocessing steps as gating and registration. In this work, we investigate the feasibility (using two approaches) of detecting microbubbles in IVUS data by acoustic characterization using one-class cost-sensitive learning. In the first approach, we build a model for the microbubbles from samples taken from the lumen during the contrast agent injection. In the second approach, we detect the microbubbles as a change from the baseline IVUS data model (learned using random samples from different tissues within frames before injection). Using the first approach, we obtained an average accuracy of 99.17% for the detection of microbubbles and 91.67% for the classification of pre-injection frames as not containing microbubbles. Using the second approach, the average accuracy on the detection of baseline IVUS data was 89.65% and 96.78% on the classification of microbubbles as change. Our results indicate that it is possible to identify microbubbles in IVUS data using one-class cost-sensitive learning.

1 Introduction

Intravascular ultrasound is currently the gold-standard modality for intravascular imaging. IVUS is a catheter-based imaging technique used to provide high-resolution, cross-sectional images of the interior of blood vessels *in vivo*. Contrast agents in the form of microbubbles are commonly used as a tracer of blood and can be used for the detection of neovessels in plaques, which are markers of inflammation [1]. Recently, differential imaging techniques that allow detection of microbubbles in stationary sequences have been developed [2]. However, the disadvantage of these methods is related to the necessity of using gated sequences and a registration step. These tasks are difficult due to the nature of the IVUS

images. In addition, these methods work with the cartesian B-mode representation of the IVUS signal. This is a disadvantage because the transformation to this representation results in loss of potentially valuable information.

In this work, we investigate the feasibility of detecting microbubbles in IVUS data by acoustic characterization of the raw IVUS data using two approaches based on one-class cost-sensitive learning. In the first approach, we build a model for the microbubbles from samples of microbubbles present in the lumen during the contrast agent injection. In the second approach, we detect the microbubbles as a change from baseline IVUS data. For this, we build a model using random samples from different tissues of the vessel extracted from frames before the injection.

The primary advantage of these approaches is that we make use of the raw IVUS data, thus we do not lose information contained in the frequency of the radio frequency IVUS (RF) signal. The second advantage is that by using one-class learning, we do not need to provide “background” samples for building the models. In our case this is important because, although samples for microbubbles in lumen can be easily acquired by manual annotations from an expert, the background can consist of a wide variety of other imaged tissues. Thus, obtaining samples for the other tissues may be difficult and labor-intensive to obtain.

Our contribution is a method for the identification of contrast agent in ungated IVUS data based on one-class cost-sensitive learning using the raw RF IVUS signal. The advantages of our method are: 1) we do not need to compute pixel correspondence between frames; and 2) we can process ungated sequences.

The rest of this paper is organized as follows: In Section 2, we provide background on the problems surrounding our task. In Section 3, we present the details of our method. In Section 4, we present our results. Finally, Sections 5 and 6 present a discussion and our conclusions, respectively.

2 Background

Intravascular ultrasound: The IVUS catheter consists of either a solid-state or a mechanically-rotated transducer which transmits a pulse and receives an acoustic signal at a discrete set of angles over each radial scan. Commonly, 240 to 360 such one-dimensional signals are obtained per rotation (digital or mechanical). The envelopes of these signals are computed, log-compressed, and then geometrically transformed to obtain the familiar disc-shaped IVUS image (Fig. 1). In this paper, we define the received acoustic signal as I , the positive-envelope of this signal as I_e and the log-compressed envelope of this signal by I_l . The signal I has a large dynamic range and retains far more information than I_e and I_l , including the frequency-domain information lost during envelope calculation. This “raw” signal is the basis for more recent radiofrequency-domain IVUS studies [3, 4].

Contrast agents: Most modern ultrasound contrast agents consist of solutions of echogenic microbubbles. These gas-filled spheres are surrounded by a shell designed to aid their longevity in the bloodstream. The scale of these bubbles

(diameter: 1-10 μm) is similar to the scale of red blood cells (diameter: $\sim 8 \mu m$), and hence they may be used as tracers of blood flow. While these agents are used routinely for non-invasive ultrasound applications (e.g., echocardiography), in IVUS, these agents have proven useful for imaging plaque perfusion in the coronary arteries [5]. Fundamental [2] and harmonic [6, 7] imaging have been used for detecting microbubble contrast agents in IVUS.

One-class learning: The one-class support vector machine (SVM) method is a widely-studied learner or “recognizer”. The strategy of one-class SVM is to map the data into an infinite feature space and then use a hyper-sphere to describe the data in that feature space. We want the hyper-sphere to be as small as possible, while at the same time including most of the training data. The trade-off between the radius of the hyper-sphere and the number of training samples that it can hold is set by the parameter $\nu \in [0, 1]$. Small values of ν will attempt to put more data into the hyper-sphere while larger values of ν will try to squeeze the size of the hyper-sphere. The second parameter of interest is the width, γ , of the SVM radial basis function (i.e., $k(\mathbf{x}, \mathbf{x}') = \exp(-\gamma \|\mathbf{x} - \mathbf{x}'\|^2)$) for a pair of feature vectors \mathbf{x} and \mathbf{x}'). Properties of a good SVM solution include an acceptable classification rate as well as a low number of resulting support vectors relative to the number of training examples.

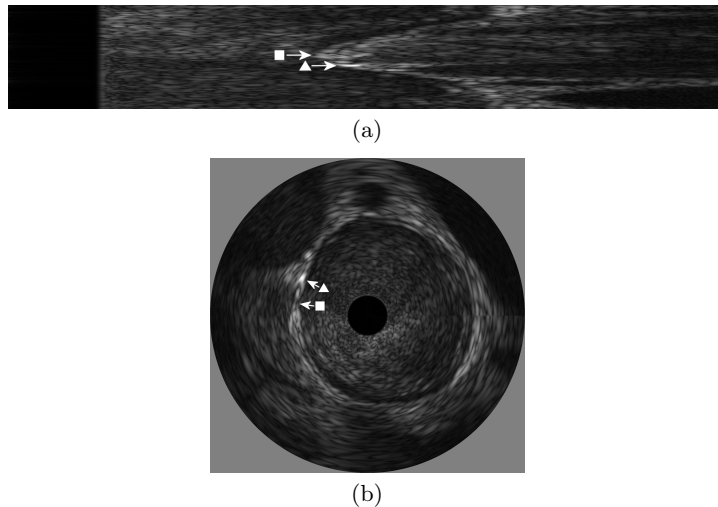


Fig. 1. (a) The log-compressed envelope of the IVUS signal in polar format. The r axis is horizontal (the origin being at the left, at the catheter) and the θ axis, vertical (of arbitrary origin). (b) The same signal after Cartesian transformation. The arrows marked \triangle and \square (provided for orientation only) are positioned similarly in the polar and Cartesian spaces.

3 Materials & Methods

3.1 Data Acquisition

In vivo ungated IVUS sequences were acquired in swine using a 40 MHz catheter, from which the raw backscatter data was sampled at 400 MHz. Recordings were made over a matter of minutes, during which time the catheter was held steady. Approximately half-way through recording, a bolus injection of microbubbles (SonoVue[®]) took place proximally to the imaging catheter. This resulted in a brief (1 to 3 s) period of luminal echo-opacity followed by a gradual diminution of contrast in the lumen (5 to 10 s).

By stacking the 1-D raw signals we obtain a 2-D frame in polar coordinates. Stacking consecutive frames over time, we obtain a 3-D volume $i(r, \theta, t)$ where r indicates radial distance from the transducer, θ is the angle with respect to an arbitrary origin, and t is the time since the start of the recording (i.e., frame number).

3.2 Features

For our models, we use those features based on frequency-domain spectral characterization that represent measures of high-frequency signal proposed by O'Malley *et. al* [8] since spectral analysis have shown to be reliable to analyze the backscattered signals in IVUS [4]. Specifically, these features are defined for a 3-D signal window of dimensions $r_0 \times \theta_0 \times t_0$ as follows:

$$F_\zeta = \sum_{i=1}^{\lceil r_0/2 \rceil} \sum_{j=1}^{\lceil \theta_0/2 \rceil} \sum_{k=1}^{\lceil t_0/2 \rceil} ijk \hat{W}(i, j, k) \quad (1)$$

$$F_\eta = \frac{F_\zeta}{\sum_{i=1}^{\lceil r_0/2 \rceil} \sum_{j=1}^{\lceil \theta_0/2 \rceil} \sum_{k=1}^{\lceil t_0/2 \rceil} \hat{W}(i, j, k)}, \quad (2)$$

where \hat{W} indicates the magnitude of the Fourier spectrum of the windowed signal W . Each feature F_ζ and F_η , is computed on I_e and I_l in addition to I . Hence, each feature is a vector of three values. The samples are extracted by placing a 3-D fixed size window (r_0, θ_0, t_0) around each sample in the volume. The features F_ζ and F_η are computed for this window and are associated with the class contained by it. To improve the scaling of the feature space, each feature of the samples used for training is normalized to zero mean and unit variance. The normalization values are retained for use in testing and deployment.

The microbubble samples were obtained from a manual segmentation of the lumen by a human expert on those frames that encompass the period from when the lumen was no longer echo-opaque following injection to when contrast was no longer visible in the lumen. It is important to mention that we only obtained samples from the volume regions where the label corresponded to lumen on all the frames along t .

For obtaining the baseline IVUS samples, we use data from the pre-injection period that corresponds to those frames that encompass the period from the

start of the recording to one frame before the contrast agent was first visible in the lumen.

For the first approach, microbubble samples are used as examples for the positive class S_+ in training and testing. In addition, baseline IVUS samples are used as negative examples S_- for testing, since we know that there are no microbubbles. Similarly, for the second approach, samples from the baseline IVUS are used as the positive examples S_+ for training and testing, and samples of microbubbles are used as negative examples S_- for testing the detection of the change.

3.3 Training & Testing Scheme

In each case, given a set of positive S_+ and negative S_- examples, a grid search for the one-class SVM parameters γ and ν is performed over a subset of the positive and negative samples to optimize the models. Optimization in this case aims to obtain an acceptable true positive rate on S_+ , true negative rate on S_- , and low number of support vectors. The one-class SVM models for each approach are computed using only the positive examples of the subset corresponding to each case. Next, the rest of the positive and negative examples are used for testing. Thus, we will have two accuracy results: accuracy on the samples of the class of interest (microbubbles for the first approach and baseline IVUS for the second) correctly classified as positive, and accuracy on the other samples correctly classified as negative. The parameters γ and ν must be selected in such a way that high accuracy on the classification of the class of importance and in the classification of the negative samples is obtained. However, since it is possible to have higher accuracy on the classification of negative samples than in the class of interest, we will constrain the selection of parameters to provide an accuracy on the class of interest as close to 100% as possible. Therefore, the criteria for the selection of the best parameters is given by a weighted linear combination of the accuracy on the classification of both classes:

$$A = w_1 A_P + w_2 A_N, \quad (3)$$

where A stands for total accuracy, A_P and A_N are the accuracies on the class of interest and on the negative samples respectively, and w_1 and $w_2 \in [0, 1]$ are the weights associated with the class of interest and negative sample accuracy respectively. This can be considered cost-sensitive learning for one-class classifiers.

4 Results

We evaluated our method in two different IVUS sequences using LibSVM [9] to train the one-class SVMs with the Gaussian radial basis kernel function. We use as features F_ζ , F_η , as well as the concatenation of both features over a window of size $(r_0, \theta_0, t_0) = (255, 13, 13)$ that is equal to a radial resolution of $\sim 600 \mu m$,

Table 1. Number of examples used for training and testing.

| | Case 1 | | Case 2 | |
|----------|--------------|---------------|--------------|---------------|
| | Microbubbles | Baseline IVUS | Microbubbles | Baseline IVUS |
| Training | 28,386 | 25,800 | 4,692 | 25,784 |
| Testing | 177,940 | 101,248 | 28,661 | 101,208 |

angular resolution of $\sim 18^\circ$, and temporal resolution of ~ 0.4 s. These values will vary by IVUS system but, in general, larger windows provide better classification at the expense of resolution (note that a temporal window of $t_0 = 13$ may be excessively long for an IVUS system whose framerate is below 30 frames/s). The weights used for the cost-sensitive learning were $w_1 = 0.8$ and $w_2 = 0.2$ for both approaches.

The number of microbubbles and baseline IVUS samples used for training and testing in each sequence are shown in Table 1. These samples were used for both approaches just by changing the class of importance (microbubbles for the first approach and baseline IVUS for the second). For both approaches the accuracy on the class of interest was below 60% when the features were used individually. We found that the best results are obtained by using the concatenation of the two features.

For the first approach, we obtained an average accuracy of 99.17% on the detection of microbubbles and 91.67% on the classification of pre-injection frames as having no microbubbles, with an average percentage of support vectors less than 1% of the total training examples. Most of the misclassifications on the pre-injection frames were in the lumen. This is due to the fact that the microbubble samples were acquired from the lumen on the frames corresponding to the microbubble injection where some blood can be still present. However, this does not pose a problem at all since the long term goal of microbubble detection is the revealing of angiogenesis in the plaque. Then, we can exclude the lumen from the analysis. Figure 2 depicts the classification results on frames during the injection and pre-injection.

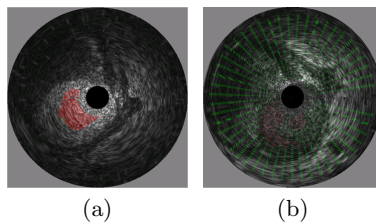


Fig. 2. Classification results in (a) frame with microbubbles in the lumen and (b) IVUS frame before injection. In both images, the red color indicates the pixels classified as microbubbles and the green color those classified as non-microbubbles.

For our second approach, we obtained an average accuracy of 89.65% on the detection of baseline IVUS data and 96.78% on the classification of microbubbles as change, with an average percentage of support vectors less than 10% of the total number of samples used for training. This low accuracy on the classification of baseline IVUS is due to insufficient samples from the baseline IVUS data. In order to obtain a higher accuracy on the classification of baseline IVUS it will be necessary to have a set of samples representative of the IVUS tissues. However, despite this low accuracy, our results indicate that it is possible to detect microbubbles as change. Figure 3 depicts the classification results on frames before the injection and during the injection.

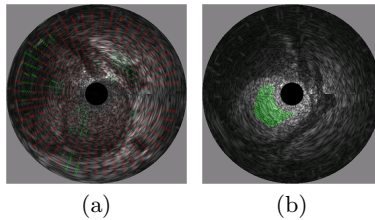


Fig. 3. Classification results in (a) IVUS frame before injection and (b) frame with microbubbles in lumen. In both images, the red color indicates the pixels classified as baseline IVUS and the green color those classified as an anomaly.

5 Discussion

The results obtained in our experiments indicate that it is possible to identify microbubbles in IVUS data using one-class learning techniques. In general, microbubbles will have larger energy compared with other tissues within the vessel. In this case F_{ζ} would be enough to discriminate between microbubbles and other tissues. However, in some cases the energy of the microbubbles' spectra is comparable with the energy of other tissues (e.g., calcified plaque, soft tissue). The normalized F_{ζ} (i.e., F_{η}) provides complementary information to differentiate between regions with similar spectral energy. Thus, concatenation of these two features is necessary for better classification.

Even though we employ samples of two classes for finding the best parameters for the classifier, this approach is better compared with traditional two-class or multi-class learning because one-class is robust to unbalanced samples since the trainer is exposed to only one class.

Since the radius of the hyper-sphere is controlled by the parameter ν , cost sensitive learning is possible with one-class using the approach presented in the methods section. In this paper, we proposed estimating the parameters for the one-class SVM based on a weighted sum of the accuracy on the classification of the class of interest and the negative class.

Our method provides good results without the necessity of gating or a registration step, the inclusion of such preprocessing could increase accuracy and would let us use a smaller window to achieve higher resolution.

6 Conclusion

We have presented a method for the identification of microbubbles in IVUS data based on one-class cost-sensitive learning using with two approaches: 1) identification by a microbubbles' model, and 2) by detecting change from baseline IVUS data. Both approaches have demonstrated the feasibility of detecting microbubbles using the raw IVUS signal without the necessity of a reference image or registration.

Acknowledgements: This work was supported in part by an award from The Methodist Research Institute-UH-Cornell Institute of Biomedical Imaging Sciences, the Eckhard Pfeiffer Endowed Chair Fund, and by NSF grants IIS-0431144 and CNS-0521527. Any opinions, findings, conclusions or recommendations expressed in this material are the authors' and may not reflect the views of the sponsors.

References

1. Gössl, M., Malyar, N.M., Rosol, M., Beighley, P.E., Ritman, E.L.: Impact of coronary vasa vasorum functional structure on coronary vessel wall perfusion distribution. *Am J Physiol Heart Circ Physiol* **285** (2003) H2019–H2026
2. O'Malley, S.M., Naghavi, M., Naghavi, M., Kakadiaris, I.A.: Intravascular Ultrasound-based detection and quantification of Vasa Vasorum. Proc. 8th International Conference on Medical Image Computing and Computer Assisted Intervention, Palm Springs, CA (2005) 343–351
3. Nair, A., Kuban, B.D., Tuzcu, E.M., Schoenhagen, P., Nissen, S.E., Vince, D.G.: Coronary plaque classification with intravascular ultrasound radiofrequency data analysis. *Circulation* **106** (2002) 2200–2206
4. Nair, A., Kuban, B.D., Obuchowski, N., Vince, D.G.: Assessing spectral algorithms to predict atherosclerotic plaque composition with normalized and raw intravascular ultrasound data. *Ultrasound Med Biol* **27** (2001) 1319–31
5. Carlier, S., Kakadiaris, I.A., Dib, N., Vavuranakis, M., O'Malley, S.M., Gul, K., Hartley, C.J., Metcalfe, R.W., Mehran, R., Stefanadis, C., Falk, E., Stone, G., Leon, M., Naghavi, M.: Vasa vasorum imaging: A new window to the clinical detection of vulnerable atherosclerotic plaques. *Curr Atheroscler Rep* **7** (2005) 164–169
6. Goertz, D.E., Frijlink, M.E., Tempel, D., van Damme, L.C.A., Krams, R., Schaar, J.A., ten Cate, F.J., Serruys, P.W., de Jong, N., van der Steen, A.F.W.: Contrast harmonic intravascular ultrasound: A feasibility study for vasa vasorum imaging. *Invest Radiol* **41** (2006) 631–638
7. Goertz, D.E., Frijlink, M.E., Tempel, D., Bhagwandas, V., Gisolf, A., Krams, R., de Jong, N., van der Steen, A.F.W.: Subharmonic contrast intravascular ultrasound for vasa vasorum imaging. *Ultrasound in Medicine and Biology* **33** (2007) 1859–1872
8. O'Malley, S.M., Naghavi, M., Kakadiaris, I.A.: One-class acoustic characterization applied to blood detection in IVUS. Proc. Medical Image Computing and Computer Assisted Intervention, Brisbane, Australia, Oct 29 - Nov 2 (2007) 202–209
9. Chang, C., Lin, C.: LIBSVM: a library for support vector machines. (2001) Software available at <http://www.csie.ntu.edu.tw/~cjlin/libsvm>.

A Heart-Centered Coordinate System for the Detection of Coronary Artery Zones in Non-Contrast Computed Tomography Data

G. Brunner, D.R. Chittajallu, U. Kurkure, and I.A. Kakadiaris

Computational Biomedicine Lab, Depts. of Computer Science, Elec. & Comp. Engineering, and Biomedical Engineering, Univ. of Houston, Houston, TX, USA
{gbrunner, drchittajallu, ukurkure, ioannisk}@uh.edu

Abstract. In this paper we introduce coronary artery zones and present a novel heart-centered coordinate system (HCCS) which is based on anatomical landmarks. The HCCS is used to align non-contrast CT heart volumes for the purpose of developing a supervised classification schema which discriminates between coronary artery zones and their surrounding tissue. The proposed method has been deployed to 30 non-contrast CT data sets. The results show an accuracy of approximately 85% for the correct detection of the coronary artery zones.

1 Introduction

Cardiovascular disease is the leading cause of death in the United States and around the globe. Recent studies have shown that coronary artery calcification is a significant and independent predictor of atherosclerotic disease and is associated with future coronary events [1][2]. Currently, the total coronary calcium burden is semi-automatically quantified using information from computed tomography (CT) heart scans by applying several scoring algorithms. Various attempts have been undertaken to improve current coronary calcium quantification techniques. For example, Brown *et al.* [3] proposed the calcium coverage score, which represents the percentage of coronary arteries affected by calcified plaque. The new calcium score was evaluated on manually annotated data from 3552 participants of the Multi-Ethnic Study of Atherosclerosis (MESA). However, for an efficient deployment of coronary calcium quantification techniques, the automatic detection of the coronary artery regions is necessary.

Automated calcium scoring requires detection of the lesions and labeling of the artery they belongs to. However, these arteries are not clearly visible in non-contrast CT data. Thus, we introduce the concept of zones that can help with labeling the *regions* of the coronary arteries. To the best of our knowledge no other group has tackled the problem of identifying coronary artery zones in non-contrast CT data. However, several authors have developed coronary artery segmentation methodologies for contrast-enhanced CT scans. It has to be noted that it is significantly easier to identify the coronaries in contrast CT scans than in non-contrast CT data, as the specific intensity values of the contrast

agent constitute a strong feature. For example, Yang *et al.* [4] proposed a hybrid approach to automatically segment the coronary arteries using a multi-scale vessel filtering and a Bayesian probabilistic method in a level set image segmentation framework. Banh *et al.* [5] followed a different approach based on a rule-based threshold framework to segment the coronary arteries from contrast-enhanced computed tomography angiography (CTA) data. Both authors used CTA datasets for their evaluations.

In this paper, we introduce coronary artery zones, and present a novel heart-centered coordinate system (HCCS) that is used for the automatic detection of coronary artery zones in non-contrast CT data. The HCCS is based on anatomical landmarks reflecting the hearts' symmetry, and it provides a framework to align heart volumes. Based on the scaled and aligned heart volumes, we introduce a supervised classification schema for the detection of coronary artery zones.

Our contributions are: 1) the introduction of coronary artery zones, 2) design of a novel heart-centered coordinate system, and 3) a supervised classification schema for the automatic detection of coronary artery zones.

The rest of the paper is organized as follows. Section 2 presents the coronary artery zone detection algorithm. Section 2.1 describes the landmarks used to construct the HCCS (Sec. 2.2). The coronary artery zones are discussed in Section 2.3. The results of the coronary artery zone detection method are presented in Section 3. Conclusions are drawn in Section 4.

2 Method

The steps for the creation of the HCCS and for the detection of coronary artery zones are outlined in the algorithm below.

Algorithm *Artery zone learning*

1. **Detect of the heart landmarks**
 - Detect the origin of the aorta and the apex of the heart
2. **Create the heart-centered coordinate system**
 - Express the voxel coordinates using a spherical coordinate system
 - Align each heart volume w.r.t. two axes: A^a and A^v (Sec. 2.2)
3. **Learn the coronary artery zones detection model**
 - Extract random points from within and outside of the coronary artery zones
 - Normalize both sets of points w.r.t. to spherical coordinates
 - Learn the coronary artery zones using SVM

2.1 Anatomical Landmarks of the Heart

We introduce a heart-centered coordinate system that is based on two anatomical landmarks: 1) the origin of the aorta, and 2) the apex of the heart. These two landmarks are currently obtained manually by an expert. Plans for an automatic detection of the landmarks are underway. The origin of the aorta is located inside the heart and forms the center of the proposed HCCS. We chose this point as origin for three reasons. First, the origin of the aorta is a robust landmark. The

robustness is to be understood with respect to ease of identification for a trained observer and small variations in its location. Second, the origin of the aorta is located at or very close to the coronary artery ostia. Third, the origin of the aorta is inside the heart, which makes this landmark very suitable as a center location. In terms of error minimization, a location inside the heart is more favorable than, for example, selecting the apex as origin. In fact, coordinate systems in other organs such as of the brain have shown superior accuracy when the origin was placed inside the organ [6].

The landmarks are located as follows. The origin of the aorta is identified from the axial view of non-contrast CT scans. The trained observer can identify the origin of the aorta as the location where the aortic valve appears in the axial view. The exact point of origin is marked at the location of the left posterior sinus, where the left coronary artery originates. The second landmark is the apex of the heart being the tip of the left ventricle located at the level of the fifth intercostal space and approximately 8 cm left of the mid-sternal line.

2.2 Heart-Centered Coordinate System

In this section, we describe the strategy to define the HCCS using the landmarks described above. In order to account for the geometry of the heart we opt for a spherical coordinate system. The center of the coordinate system is located at the origin of the aorta. The coordinate system can be described using variables $\{r, \theta, \phi\}$, within the ranges of $r \geq 0$, $0 \leq \theta \leq \pi$ and, $0 \leq \phi \leq 2\pi$, respectively.

The proposed spherical coordinate system is used for the detection of coronary artery zones and has two clear advantages over a cartesian coordinate system: 1) the origin of the frame of reference is located inside the heart and 2) it is adjusted to the organs' symmetry. We form the HCCS as follows. First, we transform the voxel coordinates of the axial CT scans to the spherical space. There is a simple way to convert a voxels' coordinate from cartesian to the spherical coordinate system and vice versa using the following set of transformations:

$$r = \sqrt{x^2 + y^2 + z^2}; \quad \phi = \arctan\left(\frac{y}{x}\right); \quad \theta = \arctan\left(\frac{\sqrt{x^2 + y^2}}{z}\right); \quad (1)$$

$$x = r \sin(\theta) \cos(\phi); \quad y = r \sin(\theta) \sin(\phi); \quad z = r \cos(\theta). \quad (2)$$

Next, we translate the center of the coordinate system to the origin of the aorta by using a simple rigid transformation. We accomplish the translation of the coordinate system, \mathbf{X}_o , to the origin of the aorta \mathbf{X}_A , by a vector \mathbf{t} , as: $\mathbf{X}_A = \mathbf{X}_o + \mathbf{t}$, where $\mathbf{t} = (t_x, t_y, t_z)^T$, with $t_x, t_y, t_z \in \mathbb{R}$. In order to finalize the HCCS we scale and align each heart scan. The scaling is performed by setting the radius equal to one, which corresponds to the distance from the center of the coordinate system (origin of aorta) to the apex of the heart. Since the coronary arteries are usually located in the same respective *regions* of a heart, we align the heart using two axes that reflect anatomical symmetry. The first axis A^a , traverses from the origin of the aorta (center of HCCS) along the left and right ventricles toward the apex. Note that this direction coincides with the anatomical trajectory of the



Fig. 1. The HCCS including the three axis, embedded in one of the cardiac scans.

left anterior descending artery (LAD). In order to perform an accurate alignment according to the two axes we need to ensure orthogonality of both axes. Therefore, the second axis A^v is based on the heart's available segmentation. Specifically, we construct a plane \mathbf{P} perpendicular to A^a (origin of the aorta to the apex). Next, we compute the maximum intensity projection (MIP) of the binarized heart volume along the first axis A^a onto the plane \mathbf{P} . Then, we obtain the axis A^v from the principal component analysis of the MIP. The axis A^v extends roughly across the left and right ventricles, reflecting a near symmetry axis of the heart. Anatomically, the axis A^v corresponds roughly to the trajectories of the right coronary artery (RCA) and the left circumflex artery (LCX), which follow the atrio-ventricular groove. Subsequently, each heart dataset is aligned by A^a and A^v , using Euler rotations. The alignment is performed such that the point $\{r = 1; \theta = \frac{\pi}{2}; \phi = 0\}$, corresponds to the apex of the heart, and that the axis A^v is aligned at $\theta = 0$ and is orthogonal to A^a . In detail, we perform three consecutive Euler rotations. First by rotating about the x-axis by an angle θ , followed by a rotation about the z-axis by an angle ϕ , and finally about the y-axis by an angle ψ :

$$\mathbf{X}'_A = \mathbf{R}_\psi \mathbf{R}_\phi \mathbf{R}_\theta \mathbf{X}_A. \quad (3)$$

The rotations are performed in \mathbb{R}^3 , where the rotation matrices are defined as:

$$R_\theta = \begin{bmatrix} 1 & 0 & 0 \\ 0 & \cos(\theta) & \sin(\theta) \\ 0 & -\sin(\theta) & \cos(\theta) \end{bmatrix}, R_\phi = \begin{bmatrix} \cos(\phi) & \sin(\phi) & 0 \\ -\sin(\phi) & \cos(\phi) & 0 \\ 0 & 0 & 1 \end{bmatrix}, R_\psi = \begin{bmatrix} \cos(\psi) & 0 & -\sin(\psi) \\ 0 & 1 & 0 \\ \sin(\psi) & 0 & \cos(\psi) \end{bmatrix}. \quad (4)$$

The HCCS is finalized once the three Euler rotations are complete. Specifically, the HCCS is scaled and aligned with respect to two anatomical symmetry axes

of the heart ensuring a high degree of robustness. The construction of the coordinate system is based on robust anatomical landmarks, such that it should be fairly easy to apply the proposed frame of reference to any cardiac CT/MRI dataset. Next, we describe a strategy to uniquely depict 3D locations of heart scan data. To that end, we incorporate the heart segmentations into the HCCS. Specifically, we create binary masks from each axial heart segmentation, such that points P_i on the interior of the heart boundary are labeled as 1, and all other points are labeled as 0. The labels p_i are determined by:

$$\{p_i\}_{i=1}^N = \begin{cases} 1 & \text{if } P_i \text{ is on/inside heart contour} \\ 0 & \text{otherwise.} \end{cases} \quad (5)$$

The distances from the center of the coordinate system to the heart boundary are recorded. Specifically, we measure the distances to the heart boundary for discrete θ and ϕ values. In our experiments we typically use a 5° resolution for every θ and ϕ , respectively. However, more details on parameter settings/variations are provided in Sections 2.3 and 3. In other words, we could describe the heart boundary encoding as a radius vector: $\mathbf{r} = \mathbf{r}(\theta, \phi)$. Figure 2 shows the coronaries for one subject, as represented in the HCCS. Note that, anatomically, the coronary arteries traverse on, or very close to, the *surface* of the heart. Now that the HCCS is outlined and the heart contours are represented appropriately, we describe the strategy for the second contribution of this paper: *how to detect the coronary artery zones based on the HCCS*.

2.3 Coronary Artery Zones

The HCCS serves as the frame of reference for defining the coronary artery zones. In general, the zones are defined using the location of the main arteries: RCA, LCX, left main coronary artery (LM) and the LAD. However, we combine the zones of the LM and LAD. Hence, the heart is divided into three artery zones corresponding to LAD, LCX, and RCA. Each zone will be defined as a tubular *region* around manually supplied coronary artery trajectory points. We will conduct experiments using three different radii of 3 mm, 5 mm, and 7 mm for every zone. A radius of 8 mm was proposed by Carr *et al.* [2] for the manual identification of coronary calcifications.

As the distances from the center of the HCCS to the heart boundaries are readily available, we can commence with the learning step (see Algo. *Artery zone learning* Step 3). To that end, we incorporate a support vector machine (SVM) [7] as supervised classifier. The objective of the learning step is to discriminate between the coronary artery zones (positive class) and surrounding tissue (negative class). Thus, we supply the SVM with the radial distances from the center of the HCCS to the coronary artery trajectory points (labeled by an expert), and to the points from the non-artery locations, as well as their respective angles θ and ϕ . The labeled points are converted and represented in the HCCS, such that the actual distance, with respect to the center of the coordinate system,

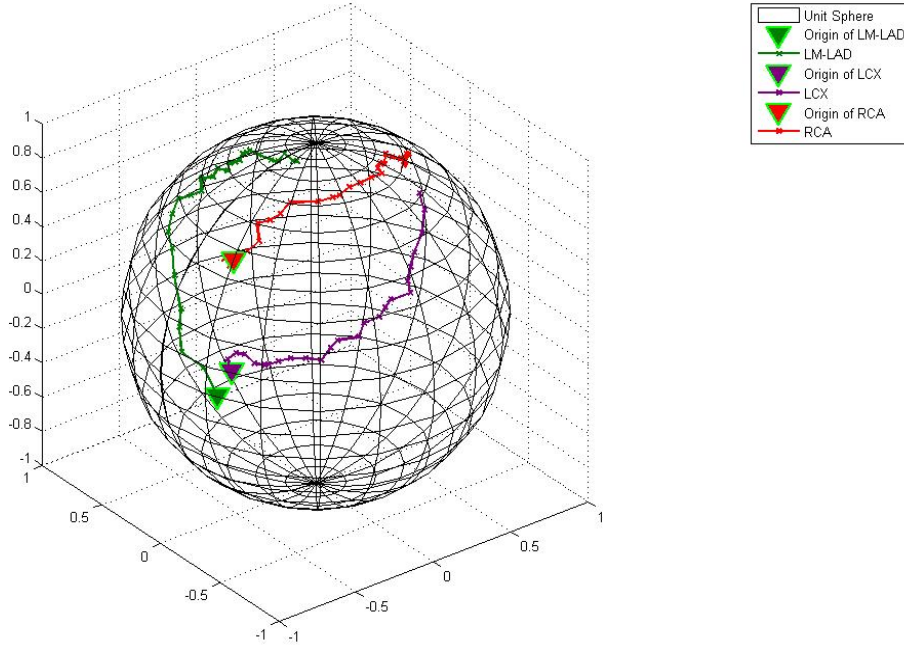


Fig. 2. Coordinates of the coronary artery trajectory points for one subject, as represented in the HCCS. The colors green, purple and red correspond to the LM-LAD, LCX, and RCA, respectively.

of the coronary trajectory points d_t is normalized by the actual heart boundary distance d_h :

$$d_t^n = \frac{d_t}{d_h}, \quad (6)$$

where d_t^n , denotes the normalized distance of a point from the center of the HCCS for a specific θ and ϕ . In detail, we deploy a two-class SVM using a Gaussian radial basis kernel function (RBF). This type of SVM requires to set two parameters: γ , the width of the gaussian, and C the penalty cost parameter. The trained SVM model will be deployed to the test data in order to classify points as being inside or outside of a coronary artery zone. The test data points are converted in a similar fashion as the training data points. More details on the experimental setup can be found in Section 3.

3 Results and Discussion

The proposed coronary artery zones detection method is tested on single electron beam CT (EBCT) datasets from 30 patients.

Data: The non-contrast cardiac scans were acquired at an EBCT (GE Imatron eSpeed) scanning facility (HealthWISE Wellness Diagnostic Center, Dublin, Ohio). Each participant provided written informed consent. For each scan, a stack of 20-36 contiguous slices with slice thickness of 3 mm each, covering the heart, were acquired. The pixel sizes ranged from 0.508 mm to 0.586 mm.

The heart segmentations used in this paper have been obtained manually by an expert who delineated the contour of the parietal pericardium in the axial view. The segmentations extend from the *start* of the heart to the apex of the heart. The *start* of the heart is identified as the center point of the ascending aorta at the z-location near the aortic arch. Specifically, it is the z-location - in scanner space - where the aorta, superior vena cava and pulmonary trunk propagate into the heart.

Experiments: The SVM is trained using only location information of the points belonging to the coronary artery zones (positive class) and the background class (negative class). In detail, each point is represented by the normalized radial distances d_i^n (see Eq. 6), and their respective angles (θ and ϕ), as obtained from their HCCS representations. The positive class points are obtained by an expert who visually identifies the location of the coronary arteries and marks points along the arteries. Note that the number of annotated points changes across patients and that the points are not equidistant. We obtain a larger number of coronary artery trajectory points by sampling the regions of the zones. As the labeled artery points are always to be found inside one of the coronaries, we can assume a radius around each point. On average, coronary artery vessels exhibit diameters of 3.06 ± 0.93 mm in EBCT data [8]. Therefore, we investigate three different coronary artery zone radii 3 mm, 5 mm, and 7 mm around each and every artery trajectory point in order to provide training data for the positive class. We sample additional artery points around each trajectory point inside the zones at angles of 45° . Hence, we obtain a set whose size is 8-fold the size of the set of the initially labeled trajectory points. This setup allows us to study the classification performance with respect to different zone radii and it provides us with a densely sampled point set. In order to train an accurate model of coronary artery zones we also need a sufficiently large number of background class points. To that end, we densely sample points for the background class from outside the zones. The normalized distances from the center of the HCCS to the background class points are defined in the same manner as for the positive class points (see Eq. 6).

The SVM model is trained using 30% of the datasets for each of the three zone radii, and tested on the remaining data. The training and testing was conducted three times in order to ensure a stable performance. We have performed 3-fold cross validation as well as conducted a grid search in order to identify the *best* γ (2.82) and C (1448) parameters (using the training data only). For the cross-validation of the training data we can report an average accuracy of 84.52%. We have computed the averaged accuracy, as well as the standard deviation of the accuracy, for the three different artery zone radii. Our proposed coronary

artery detection achieved an average accuracy of $83.82 \pm 0.06\%$, $84.49 \pm 1.12\%$, and $85.56 \pm 0.38\%$ for coronary artery zones of radii 3 mm , 5 mm , and 7 mm , respectively.

4 Conclusion

We have introduced coronary artery zones and presented a novel heart-centered coordinate system that is based on anatomical landmarks. The proposed HCCS was used to align non-contrast CT heart volumes of 30 patients. The aligned datasets have been used for the development of a supervised classification schema for the detection of coronary artery zones. Our coronary artery zone detection method achieved an accuracy of approximately 85%. The results indicate that location information is a significant feature for the detection of the coronaries, provided an aligned coordinate system is used. We plan to further investigate the HCCS and the coronary artery zone detection in a larger cohort.

Acknowledgments: This work was supported in part by the Biomedical Discovery Training Program of the W.M. Keck Center for Interdisciplinary Bioscience Training of the Gulf Coast Consortia (NIH Grant No. 1 T90 DA022885 and 1 R90 DA023418), and in part by NSF Grants IIS-0431144, and CNS-0521527.

References

1. Agatston, A., Janowitz, W., Hildner, F., Zusmer, N., Viamonte, M.J., Detrano, R.: Quantification of coronary artery calcium using ultrafast computed tomography. *J Am Coll Cardiol.* **15**(4) (1990) 827–32
2. Carr, J.J., Nelson, J.C., Wong, N.D., McNitt-Gray, M., Arad, Y., Jacobs, D. R., J., Sidney, S., Bild, D.E., Williams, O.D., Detrano, R.C.: Calcified coronary artery plaque measurement with cardiac ct in population-based studies: standardized protocol of multi-ethnic study of atherosclerosis (mesa) and coronary artery risk development in young adults (cardia) study. *Radiology* **234**(1) (2005) 35–43
3. Brown, E.R., Kronmal, R.A., Bluemke, D.A., Guerci, A.D., Carr, J.J., Goldin, J., Detrano, R.: Coronary calcium coverage score: Determination, correlates, and predictive accuracy in the multi-ethnic study of atherosclerosis. *Radiology* **247**(3) (June 2008) 669–75
4. Yang, Y., Tannenbaum, A., Giddens, D., Stillman, A.: Automatic segmentation of coronary arteries using bayesian driven implicit surfaces. In: *Biomedical Imaging: From Nano to Macro, ISBI, held in Metro Washington DC, USA.* (2007) 189–192
5. Banh, D.T., Kyprianou, I.S., Paquerault, S., Myers, K.J.: Morphology-based three-dimensional segmentation of coronary artery tree from CTA scans. In: *Medical Imaging 2007: Image Processing.* Volume 6512. (2007)
6. Xiao, J.: A new coordinate system for rodent brain and variability in the brain weights and dimensions of different ages in the naked mole-rat. *J Neurosci Methods* **162**(1-2) (2007) 162–70
7. Vapnik, V.: *The Nature of Statistical Learning Theory.* Springer, N.Y. (1995)
8. Achenbach, S., Moshage, W., Ropers, D., Bachmann, K.: Comparison of vessel diameters in electron beam tomography and quantitative coronary angiography. *Journal of Cardiac Imaging* **14**:1 (1998) 1–7

Removal of bone information in dual energy CT

Lei Zheng, Dmitry Maksimov, Tobias Stutzmann, Susanne Jochum, Carolin Brockmann, Steffen Diehl and Jürgen Hesser

Dept. of Radiology, University of Heidelberg, Mannheim, Germany
lei.zheng@medma.uni-heidelberg.de

Abstract. Computer tomography angiography (CTA) allows to assess the degree of stenosis in vascular systems, but requires the separation of vessels against bone and calcifications. In this paper, a new technique of converting dual energy data into a virtual native and contrast agent scan pair allows to use a graph based method of bone removal for CTA [1]. For evaluation purposes, patients with a high degree of calcification, i.e. complicated cases, are considered.

Our automatic bone-removal technique requires 28-30 minutes on a Intel Core 2 Quad 2.66 GHz with 4 GByte RAM for a 1.2 GByte data set and is applied in the clinic for evaluation purposes. For 10 evaluated patients, sensitivity, specificity, and accuracy are 90%. A further improvement of the differentiation quality is limited by the noise of the CT images.

1 Introduction

Arterial occlusive diseases are a major issue especially for the aging population. For example, intermittent claudication in lower extremities is found in 3-7% of the population of age 60 or more worldwide [2]. One non-invasive imaging strategy for diagnosis is computed tomography angiography (CTA). Standard techniques for bone removal in CTA are not addressed here. Corresponding details can be found in [3-5]. Recently, with upcoming dual energy computed tomography devices (DECT) new diagnostic options appear.

A DECT is equipped with two X-ray tubes and two corresponding detectors. Both X-ray sources are operated at different energy levels. While material decomposition on DECT has been studied for the determination of vertebral bone mineral content [6], for the evaluation of calcium in pulmonary nodules [7, 8], and for the quantification of abdominal fat tissue [9], the most recent method for material differentiation on DECT is presented in [10]. This method is based on the fact that iodine, which is commonly used in CT as contrast material, shows a much larger increase of the CT value with decreasing X-ray tube voltage than hydroxyapatite [11]. By locally denoising the volumes¹, the algorithm determines the iodine content based on a three-material decomposition to simulate the virtual unenhanced image, and then extract the object edges with their

¹ By this denoising the resolution of the data set is reduced and thus small vessel structures cannot be handled, which is a systematic limitation of this approach.

neighbor information. The related phantom studies and clinical evaluations can be found in [12–15].

After overcoming initial problems [16], the recently developed DECT system SOMATOM Definition (Siemens Medical Systems, Forchheim, Germany) can provide both image data sets, acquired at low kV (e.g. 80 kV) and at high kV (e.g. 140 kV), with similar image noise [17]. This scanner offers a limited field of view where the volume is reconstructed for both energies, which is a systematic problem when the patient body does not fit within this volume. Further, within that field, differentiation between calcification and vessel in current methods is based on different absorption characteristics. In this paper, we show that due to artifacts and noise, a reliable segmentation of calcified structures and contrast agent is not feasible using the Hounsfield units alone. Therefore, a problem-specific post processing is necessary to overcome the limitation and to include structural knowledge in order to achieve high separation quality. The goal of this paper is an automatic and fast alternative for bone removal for CTAs, which can partially be applied for calcifications as well.

2 Method

The workflow of our method is shown in Fig. 1. First, a pair of DECT images is used to classify bone (BC), vessels (VC) by using a three-material decomposition technique. In parallel, the thresholding routine selects all bright structures out of the background (BVC) from the high energy image. Next, the binary volume BVC is post-processed with a priori information about the structures to be the segmentation of all bones, vessels, and calcifications (BVS). With the same procedure, the classified bone volume BC is interpreted as the segmentation of a native scan (BS) and used to markup bone areas in the segmentation image BVS . It allows, finally, detecting and accurately separating bones and nearby vessels to obtain the final bone-removed volume using a graph technique.

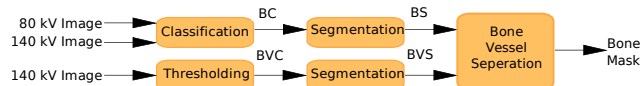


Fig. 1: Workflow of the method.

2.1 Dual energy classification

Dual energy image pairs are analyzed to determine the material content of each bright voxel based on a three-material decomposition. Each voxel is assumed to be a tissue-iodine combination or a tissue-calcium combination. Considering noise, the confidence region around the decomposition line is used for classification. Formally, two hypotheses are tested:

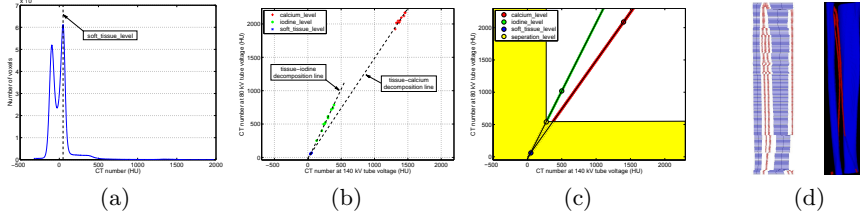


Fig. 2: (a) Soft tissue peak in the histogram; (b) Different material levels in 10 real cases and the decomposition lines approximated in one case; (c) Material classification in the dual energy graph; (d) Graph matching: Left: Colored graph; Right: Corresponding colored volume.

$$\begin{aligned}
 H_I : & \begin{cases} \text{gray_value} = \alpha_1 \times \text{soft_tissue_level} + \alpha_2 \times \text{iodine_level} + \eta_I \\ \eta_I \sim N(0, \sigma_I) \end{cases}, \\
 H_C : & \begin{cases} \text{gray_value} = \beta_1 \times \text{soft_tissue_level} + \beta_2 \times \text{calcium_level} + \eta_C \\ \eta_C \sim N(0, \sigma_C) \end{cases},
 \end{aligned}$$

where $N(x, y)$ represents a normal distribution with mean x and spread y . If H_I is accepted, i.e. the gray value is a linear combination of the typical values of soft tissue and iodine with a Gaussian noise, the voxel is considered as a tissue-iodine combination. Similar relationships are expected for H_C and the tissue-calcium combination. The higher iodine concentration increases α_2 and decreases α_1 , which makes the vessel voxels more separable against the others.

A typical value of the *soft_tissue_level* is represented by the soft tissue peak in the histogram (Fig. 2a), which is robust against noise in the data due to the summation procedure. This level is 47.7 ± 6.2 HU (Hounsfield units) in the 140 kV data and 60.3 ± 6.6 HU in the 80 kV data for our 10 cases.

As an initial evaluation, for each patient, we assign typical voxel regions of different material separately in the original gray value image with the normal region growing approach. The typical voxels of vessels are selected from the highly enhanced arteries in the thigh, while the region of bone is assigned to the compact and homogeneous part of the femur. The *iodine_level* and *calcium_level* are the mean value of the corresponding sample set, which contains at least 10^4 voxels. Fig. 2b shows the gray value pairs of the case study of our 10 datasets. The tissue-iodine decomposition line and the tissue-calcium decomposition line are defined by connecting the *soft_tissue_level* and the respective material level. The lines do not overlap, similarly as the observation before [11]. The contrast enhanced vessels and bone/calcifications are separable in practice based on the three-material decomposition strategy.

The confidence regions around the decomposition lines are estimated based on the typical voxels assigned by the user. The gray value of each voxel is taken as a 2-element random vector \mathbf{X} , corresponding to two energy levels. For each kind of material, the assigned voxel samples are used to calculate the 2-by-2 covariance matrix $\Sigma = E[(\mathbf{X} - E[\mathbf{X}])(\mathbf{X} - E[\mathbf{X}])^T]$, where $E[\mathbf{X}]$ is the expected

value of the random vector. The square root of the small Eigenvalue of Σ represents the standard deviation of noise in the dual energy graph.² According to the underlying reconstruction process, we can assume the noise being normally distributed. Thus, the region within two standard deviations of the decomposition line contains about 95% of the values.³

Hence, in order to classify different materials, the following rules⁴ are used.

- The threshold $separation_level = (soft_tissue_level + iodine_level)/2$ differentiates the background and the bright structures. Any voxel with gray value less than this threshold in one energy image is classified as background, i.e. the yellow region in Fig. 2c.
- Testing H_I on the remaining voxels, those within the confidence region around the tissue-iodine decomposition line are classified as vessels (VC), i.e. the green part in Fig. 2c.
- Testing H_C on the remaining voxels, those within the confidence region around the tissue-calcium decomposition line are classified as bone and calcifications (BC), i.e. the red part in Fig. 2c.
- The Other voxels are left as undecided, i.e. the white region in Fig. 2c.

2.2 Post-Processing

From the high energy (140 kV) image with a larger scan field-of-view than that of the low energy (80 kV) image, all bright structures are separated from background by thresholding with the threshold $separation_level$, considered as a pre-segmentation of the interlaced bone and vessel structures (BVC). In parallel, the bone voxels BC that are classified according to the rules above are considered as an initial set of markers for bone.

Binary volumes BC and BVC are denoised using opening and closing operators in order to overcome small reconstruction artifacts, which limits the spatial resolution to 3 voxels (transversely 2.4 mm in our case). In addition, the body of the patient is extracted as the region of interest. Furthermore, for both BC and BVC , 2D level-sets are used in all slices to find proper boundaries of the bone and to unify all inner structures to one bone node. Starting from the bounding-box of each object, the propagation of the level-set curve Φ follows the equation:

$$\frac{\partial \Phi}{\partial t} + (1 - I(x, y)) \|\nabla \Phi\| - 2(1 - I(x, y)) \|\nabla \Phi\| \nabla \cdot \frac{\nabla \Phi}{\|\nabla \Phi\|} = 0,$$

where $I(x, y)$ is the binary 2D section of the volume. Here, the second item represents the propagation force, which shrinks the contour, and the third item corresponds to the curvature force, which keeps the contour smooth.

The result of the level set processing of BC yields the segmented bone BS (see Fig. 3), which indicates the bone structure in the image. The result on the BVC data set yields the BVS , i.e. the segmented bone and vessels. BS and

² By choosing homogeneous materials for the estimation of the bone and contrast agent curve, we minimized the deviations and thus the spread is only related to noise.

³ Hereby, we ignore reconstruction artifacts which are corrected later.

⁴ The rules are designed for point to point measurement, without considering the non-linear behavior for the partial volume effect.

BVS are the basic structures that correspond to native and contrast enhanced CT and thus our CTA bone removal program can be applied [1]. In order to understand the following processing, a short summary of this approach follows.

Both segmentation results BS and BVS are represented as graphs in form $G = (\mathcal{E}, \mathcal{V})$. The node $n \in \mathcal{E}$ presents an 8-connected area of one particular slice. n is enriched with two attributes: a_1 , the position of the slice for the area, and a_2 , the boundary of this area. The edge $e = (n_1, n_2) \in \mathcal{V}$ is generated for each pair of nodes n_1, n_2 , if their areas a_2 are 26-connected in the volume. From now on, let us call BG and BVG the graphs generated from BS and BVS respectively.

Both graphs BG and BVG are matched by graph-coloring which generates a sub-graph SGB as follows:

```

 $SGB = \{\}$ 
for each node  $n_{bg} \in BG$ 
   $N_{BVG} = \{n \in BVG \mid a_1(n) = a_1(n_{bg})\}$ 
  for each node  $n_{bvg} \in N_{BVG}$ 
    if  $size\_of(a_2(n_{bvg}) \cap a_2(n_{bg})) / size\_of(a_1(n_{bvg})) > 0.2$ 
       $SGB = SGB \cup \{n_{bvg}\}$ 
    end_if
  end_for
end_for

```

Here, $size_of(\cdot)$ denotes the function that counts the number of pixels inside a region. After this process, two sub-graphs from BVG are generated. The sub-graph SGB contains only nodes assigned to bone whereas the disjoint sub-graph $SGV = BVG \setminus SGB$ represents the vessel system.

Subsequent graph analysis detects neighboring vessel and bone structures (see Fig. 2d). By assigning a different "color" property to the structures, we state: A conflict situation is given, if an edge of BVG joins two nodes with different colors:

$$(n_1, n_2) \in BVG \text{ is a conflict edge} \Leftrightarrow ((n_1 \in SGB) \text{ AND } (n_2 \in SGV)) \text{ OR } ((n_1 \in SGV) \text{ AND } (n_2 \in SGB))$$

Such conflict situations in the graph appear where the vessel touches the bone. In the coloring step, these nodes are marked as bone.

The separation of bone and vessels in these conflict situations is done by controlled region-growing. For each conflict situation, the algorithm starts at a conflict edge and proceeds slice-wise (in the direction established by this edge) growing a correct vessel segmentation in the way described by SGB nodes, until some possible exit back to the vessel system SGV is found. After all conflict edges are processed one after the other, the corrected SGV and SGB describe vessels and bones disconnected from each other.

Masking out of the bone expressed by SGB from the initial gray-scale volume yields the separated vessel structures. Remaining calcifications are then separated from the vessel structures by plot-profile techniques assuming that the calcifications are compact, a property fulfilled throughout our data sets.

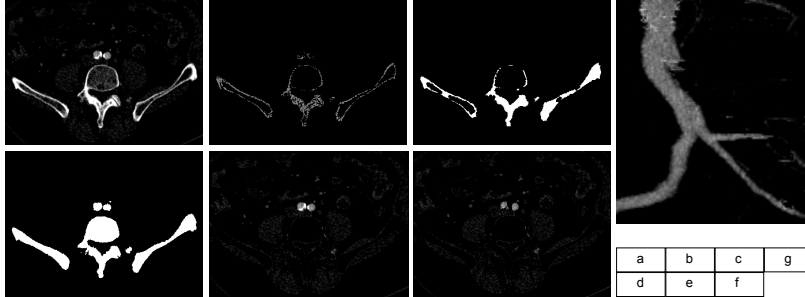


Fig. 3: (a) Original high energy image; (b) *BC* image; (c) *BS* image; (d) *BVS* image; (e) Bone-removed image; (f) Output image without bone and calcifications; (g) MIP visualization of the result.

3 Results

We investigated 10 patients (2 female and 8 male) with a mean age of 63.4 years. All of them have signs of lower extremity occlusive disease. For the acquisition, the contrast agent with Iodine content 300 mg/mL is used. The data are acquired by a SOMATOM Definition in dual energy mode with the resolution as $0.80 \times 0.80 \times 1.5$ mm in cranio-caudal direction. The final size of the data sets is between $512 \times 512 \times 1034$ and $512 \times 512 \times 1242$ voxels.

Processing the data with our approach consumes 28-30 minutes on a Intel Core 2 Quad 2.66 GHz with 4 GByte RAM for a 1.2 GByte data set. As shown in Fig. 3, our method works fine in general.

During evaluation, MIP (Maximum Intensity Projection) visualizations of the bone-removed volumes are compared against DSA (Digital Subtraction Angiography), though a pure visual inspection of the stenosis could be inaccurate in case of highly acentric stenosis. CTA and DSA are separated

| | Stenoses $\geq 50\%$ | | |
|---------------|----------------------|-------------|----------|
| | Sensitivity | Specificity | Accuracy |
| All segments | 89.8% | 90.7% | 90.4% |
| Pelvic region | 69.2% | 100% | 91.5% |
| Thigh | 91.7% | 93.9% | 93.3% |
| Calf | 100% | 83.9% | 88.4% |

Table 1: Evaluation result

by at least 24 hours, to minimize the contrast medium charge for the individual patients. The degree of stenosis is visually sorted in 5 classes, i.e. absent, mildly stenotic ($< 50\%$ lumen reduction), moderately stenotic (50-74% lumen reduction), severely stenotic (75-99% lumen reduction), and occluded. Meanwhile, the arterial system is subdivided into 13 segments: A. iliaca com (P), A. iliaca externa (P), A. iliaca interna prox (P), A. femoralis com (T), A. femoralis superficialis (T), A. femoralis profund (T), A. poplitea P1 (C), A. poplitea P2 (C), A. poplitea P3 (C), A. tibio-fibularis (C), A. fibularis (C), A. tibialis post (C), and A. tibialis ant (C). In order to evaluate the different regions, they are classified

in 3 groups: Pelvic region (P), Thigh (T), and Calf (C), with the corresponding letter in the bracket.

Overall, 260 vascular segments are investigated, whereas 82 segments cannot be directly compared because of the limitation of data acquisition for legal reasons concerning a part of the patients. By considering only segments with stenosis $> 50\%$ occlusion (which is a reasonable limit), of the 178 segments assessable on both modalities, the sensitivity, specificity and accuracy of CTA are 89.8 %, 90.7% and 90.4 % respectively. The test values are also calculated for different parts of the leg. The complete results are presented in Table 1.

4 Discussion

The developed method is fully automatic and processes the data sets of 1.2 GByte in less than 30 minutes. Further optimization and parallelization of this code could then yield processing times of a few minutes. As an initial evaluation, we need to assign the typical voxels of vessels and bone. After accumulating enough patients, the empirical value of *iodine_level* and *calcium_level* can be used for particular system parameters, such as the current of the source and the dose of the contrast agent.

Comparing to the normal CTA, our results contain more of artifacts where the gray value of the bone is too small and is not correctly classified. Some calcifications in the small vessels are not accurately removed, leading to a larger grade of stenosis. A severe limitation of this approach is that it does not consider reconstruction artifacts, a problem that has to be addressed in future in more detail.

Meanwhile, the system parameters are set by default. One possibility to make the two decomposition lines more separable in the dual energy graph is to increase the concentration of the contrast agent, which allows pushing the points in Fig. 2b to larger values. Further, an increase of the applied dose to the patient or a pre-processing using dedicated denoising filter could improve the classification results as well. It should be balanced on behalf of the health of the patients.

References

1. Maksimov, D., Hesser, J., Dietz, T., Schnitzer, A., Düber, C., Schönberg, S., Diehl, S.: Graph-matching based cta. IEEE Transactions on Medical Imaging in review.
2. Norgren, L., Hiatt, W., Dormandy, J., Nehler, M., Harris, K., Fowkes, F.: Inter-society consensus for the management of peripheral arterial disease (tasc ii). Journal of Vascular Surgery **45** (2007) S5–S67
3. Straka, M., Cruz, A.L., Köchl, A., Šrámek, M., Fleischmann, D., Gröller, E.: 3d watershed transform combined with a probabilistic atlas for medical image segmentation. (2003) 1–8
4. Knapp, M., Kanitsar, A., Gröller, M.E.: Semi-automatic topology independent contour-based 2 1/2 d segmentation using live-wire. In: WSCG2004. Volume 12. (2004)

5. Maksimov, D., Finkel, F., Dietz, T., Diehl, S., Diiber, C., Rebholz, P., Hesser, J., Manner, R.: An interactive application for removal of bone information in ct-angiography. In: *Computer-Based Medical Systems*, 2004. (2004) 396–401
6. Vetter, J.R., Perman, W.H., Kalender, W.A., Mazess, R.B., Holden, J.E.: Evaluation of a prototype dual-energy computed tomographic apparatus. ii. determination of vertebral bone mineral content. *Medical Physics* **13** (May 1986) 340–343
7. Cann, C.E., Gamsu, G., Birnberg, F.A., Webb, W.R.: Quantification of calcium in solitary pulmonary nodules using single- and dual-energy ct. *Radiology* **145** (November 1982) 493–6 PMID: 7134457.
8. Fraser, R., Barnes, G., Hickey, N., Luna, R., Katzenstein, A., Alexander, B., McElvein, R., Zorn, G., Sabbagh, E., Robinson, C.: Potential value of digital radiography. preliminary observations on the use of dual-energy subtraction in the evaluation of pulmonary nodules. *Chest* **89** (April 1986) 249S–252
9. Svendsen, O.L., Hassager, C., Bergmann, I., Christiansen, C.: Measurement of abdominal and intra-abdominal fat in postmenopausal women by dual energy x-ray absorptiometry and anthropometry: comparison with computerized tomography. *International Journal of Obesity and Related Metabolic Disorders: Journal of the International Association for the Study of Obesity* **17** (1993) 45–51 PMID: 8383641.
10. Johnson, T.R.C., Krauß, B., Sedlmair, M., Graser, M., Bruder, H., Morhard, D., Fink, C., Weckbach, S., Lenhard, M., Schmidt, B., Flohr, T., Reiser, M.F., Becker, C.R.: Material differentiation by dual energy ct: initial experience. *European Radiology* **17** (June 2007) 1510–1517
11. Nakayama, Y., Awai, K., Funama, Y., Hatemura, M., Imuta, M., Nakaura, T., Ryu, D., Morishita, S., Sultana, S., Sato, N., Yamashita, Y.: Abdominal ct with low tube voltage: Preliminary observations about radiation dose, contrast enhancement, image quality, and noise. *Radiology* **237** (December 2005) 945–951
12. Takahashi, N., Hartman, R.P., Vrtiska, T.J., Kawashima, A., Primak, A.N., Dzyubak, O.P., Mandrekar, J.N., Fletcher, J.G., McCollough, C.H.: Dual-energy ct iodine-subtraction virtual unenhanced technique to detect urinary stones in an iodine-filled collecting system: A phantom study. *Am. J. Roentgenol.* **190** (May 2008) 1169–1173
13. Graser, A., Johnson, T.R.C., Bader, M., Staehler, M., Haseke, N., Nikolaou, K., Reiser, M.F., Stief, C.G., Becker, C.R.: Dual energy ct characterization of urinary calculi: initial in vitro and clinical experience. *Investigative Radiology* **43** (February 2008) 112–9 PMID: 18197063.
14. Primak, A.N., Fletcher, J.G., Vrtiska, T.J., Dzyubak, O.P., Lieske, J.C., Jackson, M.E., Williams, J.C., McCollough, C.H.: Noninvasive differentiation of uric acid versus non-uric acid kidney stones using dual-energy ct. *Academic Radiology* **14** (December 2007) 1441–7 PMID: 18035274.
15. Scheffel, H., Stolzmann, P., Frauenfelder, T., Schertler, T., Desbiolles, L., Leschka, S., Marincek, B., Alkadhi, H.: Dual-energy contrast-enhanced computed tomography for the detection of urinary stone disease. *Investigative Radiology* **42** (December 2007) 823–9 PMID: 18007154.
16. Kelcz, F., Joseph, P.M., Hilal, S.K.: Noise considerations in dual energy ct scanning. *Medical Physics* **6** (1979) 418–425
17. Flohr, T., McCollough, C., Bruder, H., Petersilka, M., Gruber, K., Süß, C., Graser, M., Stierstorfer, K., Krauss, B., Raupach, R., Primak, A., Küttner, A., Achenbach, S., Becker, C., Kopp, A., Ohnesorge, B.: First performance evaluation of a dual-source ct (dsct) system. *European Radiology* **16** (February 2006) 256–268

Improved Rigid Registration of Vessel Structures using the Fast Radial Symmetry Transform

Carlo Gatta¹, Oriol Pujol¹, Oriol Rodriguez Leor², Josepa Mauri Ferre² and
Petia Radeva¹

¹Computer Vision Center, Campus UAB, Edifici O, 08193, Bellaterra, Barcelona,
Spain. cgatta@cvc.uab.es

²Unitat d'hemodinàmica cardíaca hospital universitari "Germans Trias i Pujol"
Badalona, Spain

Abstract. Intravascular UltraSound (IVUS) imaging is unique in the possibility to explore internal vessel structures of the coronary wall, being a powerful tool for diagnosis. The coronary vessel is moving due to the periodical contraction and expansion of heart muscles, thus the acquired images present different artifacts. This instability, among other problems, makes harder the analysis of data in the longitudinal cut, especially for the visual evaluation of length and size of vessel structures, like e.g. calcium plaques. In this paper, we propose important improvements to an algorithm for rigid vessel structures alignment. We improve the estimate of vessel's center using the Fast Radial Symmetry Transform; then we perform the rotation estimation focusing only on the vessel boundary thus improving the alignment of vessel structures. A quantitative and qualitative comparison on 9 pullback is presented.

1 Introduction and previous work

The Intracoronary UltraSound imaging is a powerful technique for diagnosis of coronary diseases [1]. Unfortunately, the catheter and heart motion artifacts affect its usability in different ways. The induced longitudinal movement affects the interpretation of longitudinal cuts and the computation of reliable volumetric measurement; research is ongoing to devise efficacious and efficient proper gating algorithms. Moreover, the apparent roto-translation that affects the short axis view also makes harder the visual inspection of longitudinal cuts and affects the performance of automatic or semi-automatic methods for area and volume measurement. This paper focuses on the reduction of short axis roto-translation of a non-gated pullback by rigid registration of subsequent pullback frames.

Two excellent reviews on medical imaging registration can be found in [2] and [3]. However, despite a total amount of about four hundred cited papers, in these two reviews no paper has been found regarding IVUS images alignment. There is an evident need for ad-hoc solutions designed to adapt to the nature of IVUS images (heavy textured and with multiplicative noise), to estimate strong and fast apparent movement and rotation between subsequent frames while tackling

the large amount of data in a pullback (thousand frames each). In [4] the authors present a sophisticated method for non-rigid alignment of IVUS image. It is based on the use of rich local and global (contextual) descriptors and, at the same time, using cooperative-iterative strategy in order to get a good set of correspondences as well as a good final transformation. In [5] the authors present a method to suppress the IVUS image rotation based on a kinematic approach. The method is based on the assumption that the vessel wall can be described as a discrete structure which kinematics temporal evolution can be followed by a trained Neural Network, during at least one heart cycle. In [6] authors present an alignment algorithm that estimates the vessel center based on center of mass computation, followed by the estimation of rigid rotation with center in the previously obtained center of mass. The most important lack of this method is that the estimation of rigid rotation (second step of the algorithm) heavily depends on the correct estimation of translation (first step of the algorithm). To compute the rigid roto-translation between subsequent frames the authors use the center of mass as a method to estimate the center of the rotation; then computing the translation just by coordinate subtraction. While this is robust with respect to noise and changes in image texture, it performs poorly if the vessel structure is changing due to e.g. a bifurcation or a calcium plaque. Moreover, an unbalanced position of the catheter with respect to the real center of the vessel produces a heavily unbalanced spatial distribution of gray scale values in the image due to the effect of image reconstruction from radio frequency data; i.e. vessel structures far from the catheter appear darker than the ones close to the catheter. In this case, even without important changes in the vessel structure, the estimation of translation using the center of mass can be very poor. In [7] the authors present a method based on the scale-space optical flow algorithm with a feature-based weighting scheme. The algorithm has been demonstrated on a tissue-mimicking phantom, subjected to controlled amount of angular deviation.

2 Rigid registration using the Fast Radial Symmetry Transform

The proposed method is an extension of the method presented in [6]. We estimate the rotation, that was demonstrated to be effective and sufficiently robust, as in [6], but we propose to change the estimation of vessel center. We start with the assumption that the vessel boundary on the short axis can be approximated as a circle. This assumption is quite simplistic since usually a better, and well accepted, approximation is to describe it as an ellipse [5]. To support this decision, we have two main reasons. (1) Our assumption is necessary because an elliptic model can be easily “cheated” by the deformation of vessel boundary caused by a bifurcation. In these cases, an elliptic model will estimate the center of the vessel with an important error in the direction of the bifurcation. (2) The algorithm we are going to use for detecting the center of the vessel, highlights any possible radial symmetry in the image, thus it is not easy to identify an elliptic shape.

Using this vessel model, we adapted the Fast Radial Symmetry Transform [8] (FRST) to be able to estimate the center of the vessel. IVUS images are far more complex than real world images, so we designed a pre-processing step and modified the FRST according to our needs. Moreover, we force the rotation estimation to work only on the part of the image that represents the vessel boundaries. The following subsections explain the method in detail.

2.1 Pre-processing for optimal FRST performance

Since the detection of a circle performed in [8] is done computing the image gradient, we need to highlight the vessel boundaries by preprocessing the IVUS image reducing, at the same time, both the noise and the texture. Identifying a circle that fits well with the vessel is difficult since gradients that represent the vessel boundary are not well defined and bright areas far from the vessel center generate important gradients not correlated to the vessel shape. We compute the cumulative probability density function (cpdf) of gray scale values with the goal to identify a good threshold to remove lower values (no signal or blood) and keep high values (vessel tissues). Thus we suppose that vessel tissues are represented by the pixels that contribute to the cumulative cpdf between 0.75 and 1 (see figure 1 (b)). These parameters have been set empirically but the fact that they act on the cpdf, and not on the pdf directly, makes the method less sensitive to variations of contrast and image average value. The next step is to remove the

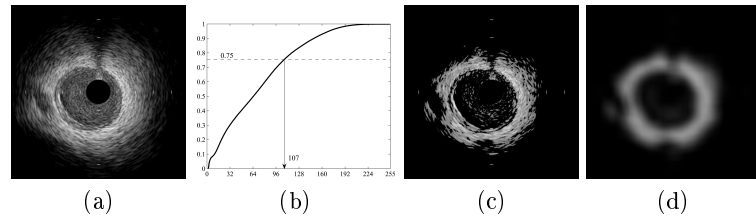


Fig. 1. From left to right: (a) the input image; (b) the cumulative probability function of gray scale values, note that the 0.75 percentile, in this case, give a threshold of 107; (c) the image after thresholding and (d) after gaussian smoothing.

texture and noise. The anisotropic diffusion can be an excellent filtering method, but it is extremely computationally expensive even using recent fast approach. Thus, we apply a strong Gaussian filter ($\sigma = 0.4mm$). This procedure smooths the texture and removes the noise (see figure 1 (d)); nevertheless, a remaining problem is that the outer boundary of the pre-processed image can be interpreted as a circle by the FRST. This has been tackled by modifying some part of the FRST as discussed in the next section.

2.2 Fast Radial Symmetry Transform

The Fast Radial Symmetry Transform has been developed to detect points of interest in an image that correspond to center of radially distributed image features (in our case to detect the center and the radius that approximate the vessel). Let us assume that we examine the detection of a radial symmetry generated by a circle of radius r . Given an input image $I(\mathbf{p})$, we can easily compute the gradient $\mathbf{G}(\mathbf{p})$, thus for each point \mathbf{p} we can compute the unit vector of the gradient as $\mathbf{D}(\mathbf{p}) = \frac{\mathbf{G}(\mathbf{p})}{\|\mathbf{G}(\mathbf{p})\|}$. Now, for each pixel \mathbf{p} , we can define the center of the symmetry (as a pixel \mathbf{q}) that potentially generated its gradient $\mathbf{G}(\mathbf{p})$ (e.g. a circle). The coordinates of this pixel are computed as $\mathbf{q}_r(\mathbf{p}) = \mathbf{p} - r\mathbf{D}(\mathbf{p})$. To obtain the transform, a set of r matrices, O_r and M_r are instantiated with the same size of I and zero values and, while exploring every point \mathbf{p} and radius r , are updated following the equations:

$$O_r(\mathbf{q}_r(\mathbf{p})) = O_r(\mathbf{q}_r(\mathbf{p})) + 1 \quad (1)$$

$$M_r(\mathbf{q}_r(\mathbf{p})) = M_r(\mathbf{q}_r(\mathbf{p})) + \|\mathbf{G}(\mathbf{p})\| \quad (2)$$

Intuitively, if in the image I there exists a circle with radius \tilde{r} and center $\tilde{\mathbf{p}}$, the edges representing the circle will have gradients that point opposite to the center of the circle. This means that $O_{\tilde{r}}(\tilde{\mathbf{p}})$ will have a value conspicuously greater than in other pixel positions. For a similar reason, if the edges were strong, the $M_{\tilde{r}}(\tilde{\mathbf{p}})$ will be very high, because it collects a lot of important gradient magnitudes. Finally, since the transformation can span over different radii, a possible synthetic bi-dimensional result can be expressed as follows:

$$S(\mathbf{p}) = \sum_{r \in \Omega} L_r(\mathbf{p}) = \sum_{r \in \Omega} \left(\frac{O_r(\mathbf{p})}{\max_p O_r(\mathbf{p})} \right)^\alpha \cdot \frac{M_r(\mathbf{p})}{\max_p M_r(\mathbf{p})} \quad (3)$$

where Ω represents the set of radii spanned by the transform and α can define how strictly the radial symmetry property has to be computed. As an example, $\alpha = 3$ will produce less relevant points with respect to $\alpha = 1$. This is easily understandable since α is the parameter of a power function with base in the range $[0, 1]$. Essentially, once computed $S(\mathbf{p})$, positions with high values represent highly probable centers of radial symmetries, thus searching for the maxima in $S(\mathbf{p})$ means searching for the more prominent symmetry in the image.

2.3 Modified Fast Radial Symmetry Transform

We modified the FRST to force the algorithm to find only the inner circle that fits into the pre-processed image. This ensures that a bad (non circular) outer boundary of vessel does not affect the algorithm performance. Moreover, to improve the performance, almost without increasing the computational cost, we implemented sub-pixel precision both in the detection of the center and radius.

Imposing inner circle detection constraint The vessel boundary cannot cross the center of the image, since it represents the catheter and thus it is physically impossible that the boundary can cross it. Taking advantage of this, we can know if the gradient $\mathbf{G}(\mathbf{p})$ at position \mathbf{p} is produced by the inner or outer edges of vessel. Being \mathbf{c} the center of the image, $\mathbf{d} = \mathbf{p} - \mathbf{c}$ represents the vector starting from \mathbf{c} , pointing to \mathbf{p} . We can compare the vector $\mathbf{D}(\mathbf{p})$ (gradient direction at point \mathbf{p}) and \mathbf{d} simply by taking the dot product. If $\mathbf{D}(\mathbf{p}) \cdot \mathbf{d} < 0$, it means that the gradient $\mathbf{D}(\mathbf{p})$ is pointing in a direction that forms an angle with \mathbf{d} that is minor than $\pi/2$. We call this the *directional constraint*. It is easy to understand that the gradients forming the outer boundary of the vessel can not respect this constraint. Using the update equations (1) and (2) only if \mathbf{p} respects the *directional constraint* improves the detection of the vessel center and radius avoiding “false symmetries” introduced by the outer vessel boundary.

Implementing sub-pixel precision Instead of searching for the maxima in $S(\mathbf{p})$, we compute the center of mass of the values in $S(\mathbf{p})$. This gives sub-pixel precision in the detection of the center. To obtain sub-pixel precision for the radius, we perform a weighted average between different “layers” $L_r(\mathbf{p})$. Being \mathbf{k} the estimated center of the vessel, then the sub-pixel precision radius is obtained by the following formula:

$$R(\mathbf{k}) = \frac{1}{\sum_{r \in \Omega} L_r(\mathbf{k})} \sum_{r \in \Omega} r L_r(\mathbf{k}) \quad (4)$$

This averaging process is more prone to outliers, however we heavily reduced the outliers numbers using the *directional constraint* and the outliers strength using an $\alpha > 1$ parameter in equation (3). Applying the Modified FRST over all the T frames of the pullback, we obtain a sequence of estimated center and radius of vessel. We denote these quantities as following: $\{(x_1, y_1, r_1), \dots, (x_T, y_T, r_T)\}$.

2.4 Rotation estimation focused on vessel boundary

As discussed before, to estimate the rotation between subsequent frames we use the algorithm proposed in [6]. The authors estimate the rotation between two subsequent images (represented in polar coordinates with the origin that lies in the previously estimated center) by spectral correlation analysis [10] but improving the algorithm’s robustness (see [6] for details). In our implementation we take advantage of the estimation of the vessel’s radius and thus we perform the rotation estimation only on a portion of the image that represents the vessel boundary. Stabilizing the vessel boundary directly implies that the plaque and calcium structures, linked to it, will be stabilized too. This is a very important aspect of the proposed method. Actually, if r_i and r_{i+1} are the estimated radii of two subsequent frames, we sample the first image in the range of radii $r_i \pm \Delta R$ and the second one in the range $r_{i+1} \pm \Delta R$, where ΔR is an algorithm parameter (see figure 2). In this way, the rotation estimation is focused on the vessel

boundaries and moreover, if a dilation or a contraction is present between subsequent frames, this procedure acts as a scale normalization procedure. Regarding robustness, if the parameter ΔR is not too small, the sampling catches the sufficient information to estimate the rotation. We empirically set $\Delta R = 0.64 \text{ mm}$ for all the results presented in the paper.

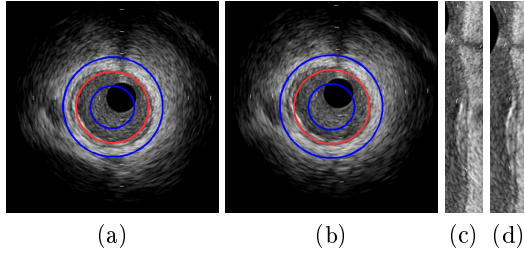


Fig. 2. (a) and (b) are two subsequent frames. The red circle is the detection of center and radius obtained with the modified FRST. The blue circles show the area that has been sampled to obtain the respective polar images (c) and (d). The rotation estimation is applied on the images (c) and (d), thus focusing mainly on vessel boundaries.

2.5 Computational issues

First, we estimate the vessel center and second, we estimate the relative rotation between vessel structures as in [6]. The first part has computational cost $\mathcal{O}(KN)$ where N is the image pixels and K is the number of radii involved in the computation of the fast radial symmetry (referring to formula (3), $K = |\Omega|$). The second part has a computational cost $\mathcal{O}(\tilde{N} \log \tilde{N})$ since it involves a convolution, where \tilde{N} is the number of pixels of the polar image. Since creating the polar image requires a re-sampling, in general $\tilde{N} \neq N$. However, once \tilde{N} is fixed, we can reduce the computational cost by transforming just a part of the polar image as discussed in the previous subsection. Summarizing, our method is K times slower than the one in [6] with regard to center estimation but it is much faster regarding the rotation estimation. Keeping K low is important to obtain a fast algorithm. To tackle this, we assume that the vessel radius changes slowly during the pullback. Thus, we perform the center estimation of first frame with a large K_{init} and, for next frames, we progressively reduce it until it reaches a smaller predefined value K_{min} . While doing this, the center of the set Ω at frame i , $r_{(\Omega,i)}$ is set to be the previously estimated radius r_{i-1} . In this way, we perform a tracking of useful radii for the FRST computation.

3 Results

We tested our algorithm on a set of 9 pullbacks from 7 patients, each containing 1000 frames. Pullbacks can present metallic stents, soft and hard plaque and one

or more bifurcations. Some pullbacks present a vessel shape that is seriously far from being circular. After a preliminary empirical evaluation we found that a good setting of parameters is: $K_{init} = 100$, $r_{(\Omega,1)} = 2mm$ and $K_{min} = 10$, such that the first FRST spans 100 radii from $1mm$ to $3mm$ and after some frames the minimum number of spanned radii is 10, covering $0.2mm$ thus implicitly assuming that the maximum radius change between two subsequent frames does not overcome $0.1mm$. Regarding the radial strictness parameter, we set $\alpha = 2$ as suggested in [8]. During preliminary testing we noticed that, while varying α does not influence heavily the algorithm performance, the setting of K_{min} needs further investigation.

Different quantitative evaluation methods for IVUS pullbacks rigid alignment have been proposed: among others, [6] proposes the use of normalized cross-correlation on plaque areas to measure the oscillation due to the heart beating, and thus an eventual decrease in the oscillation due to the alignment algorithm. In our opinion, even if this method could be reliable, it is restricted to the analysis on plaque areas and thus it is not general enough. In [11] authors propose the Cardiac Alignment Rate (CAR) as a measure of how much the motion artifacts have been suppressed by an alignment algorithm. The CAR is defined as:

$$CAR = 1 - \frac{|\mathcal{F}(q_{out}(t))(f_c)|}{|\mathcal{F}(q_{in}(t))(f_c)|} \quad (5)$$

where $q_{out}(t)$ and $q_{in}(t)$ are two quantitative measurements respective to the aligned sequence and input sequences, \mathcal{F} is the Fourier transform and f_c is the fundamental frequency of oscillation due to the heart beating. In [11] authors propose as a measure for computing $q(t)$ the image local density of mass (given by the local mean) in order to minimize the impact of texture variability and speckle. Even though this could be a practical solution, this can underestimate the oscillation, due to the averaging process and moreover it is not focused on the vessel boundaries. Starting from this approach, we add two important modifications. First, since the oscillation is rarely perfectly sinusoidal we restate the CAR measure involving the values of the first 4 main harmonics of the base frequency f_c , i.e:

$$hCAR = 1 - \frac{\sum_{n=1}^4 |\mathcal{F}(q_{out}(t))(nf_c)|}{\sum_{n=1}^4 |\mathcal{F}(q_{in}(t))(nf_c)|} \quad (6)$$

In the case of a triangular oscillation the Fourier series decreases as $1/n^2$, thus the fifth harmonic has an amplitude that is $1/25$ of the main harmonic ($n = 1$) and consequently, stopping the summation at $n = 4$ seems sufficient to our measurement. Secondly, we restrict the analysis to the area of vessel boundaries but without averaging on a local neighborhood, since we expect that texture variability and speckle noise will not influence the Fourier amplitudes involved in equation (6) but will be distributed almost randomly on other frequencies. Moreover, for visual inspection and automatic or manual segmentation in longitudinal cuts, the alignment of the vessel boundaries is far more important than the alignment of other structures of the short axis image. The Conservation of

Density Rate suggested in [11] cannot assure that the vessel structures are actually influencing the overall evaluation of the alignment algorithm. Following these guidelines, we compared the proposed algorithm to the one in [6], obtaining the table 1. The proposed algorithm outperform the one in [6] in all cases (200% better on average). Figure 3 shows different longitudinal cuts: row (a) shows the input sequence, row (b) shows the aligned sequence using the algorithm in [6] and row shows (c) our results. It can be noticed that our algorithm performs a registration that aligns important vessel's structures improving the visual inspection of e.g. the hard plaque length and the adventitia border. Moreover, in our results the lumen appears horizontal, thus showing that the algorithm removed great part of the catheter translation. It is worth to remind that different longitudinal cuts can show different features since the relative rotation between subsequent frames can be different for different algorithms.

| Seq. # | 1 | 2 | 3 | 4 | 5 | 6 | 7 | 8 | 9 |
|-----------|--------|--------|--------|--------|--------|--------|--------|--------|--------|
| Osc. Amp. | 216.14 | 322.64 | 224.02 | 186.94 | 203.42 | 336.36 | 194.75 | 263.90 | 264.93 |
| hCAR-[6] | 0.12 | 0.14 | -0.036 | 0.011 | 0.038 | 0.29 | 0.12 | 0.15 | 0.056 |
| hCAR-our | 0.18 | 0.33 | 0.096 | 0.072 | 0.19 | 0.4 | 0.2 | 0.21 | 0.084 |

Table 1. The table presents, for each sequence, the input oscillation (actually the denominator in equation (6)) and the hCAR for both algorithms. Higher values mean better performance in reducing oscillation artifacts.

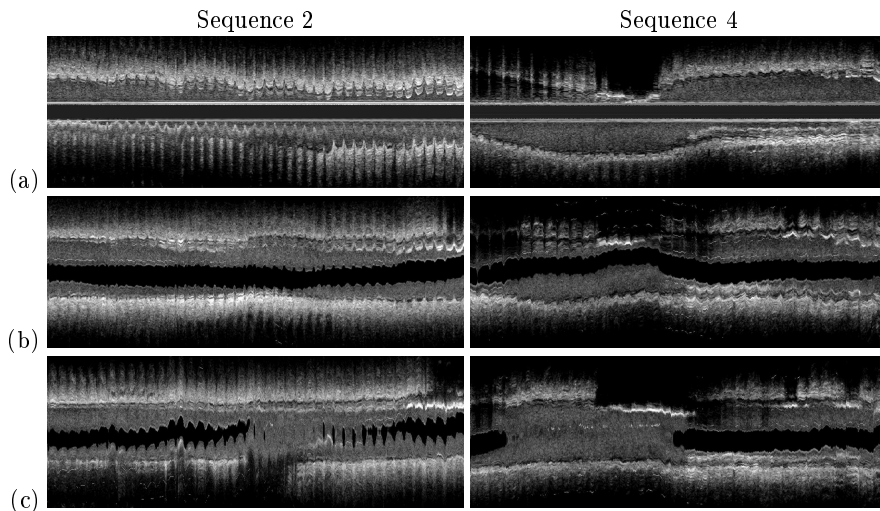


Fig. 3. Longitudinal cuts showing algorithms performance (see text for details).

4 Conclusion

The registration can be a precious tool for simplifying the visual inspection and manual measurements in longitudinal cuts. Moreover, it can be a pre-processing step for automatic segmentation of sequences and volumetric estimation. In this paper we presented a new algorithm for vessel's structures registration based on the Fast Radial Symmetry Transform. Experimental results show that the algorithm outperforms a previous approach with comparable computational cost. As a future direction, the method can be extended to fit a vessel elliptic model and also to fit different structures at a time thus detecting the lumen, the adventitia border and metallic stents.

5 Acknowledgments

This research is/was supported in part by the projects TIN2006-15308-C02, FIS PI061290.

References

1. Burke, A.P., Farb, A., hui Liang, G.T.M.Y., Smialek, J., Virmani, R.: Coronary risk factors and plaque morphology in men with coronary disease who died suddenly. *The New England Journal of Medicine* **336**(18) (May 1997) 1276–1281
2. Maintz, J.B.A., Viergever, M.A.: A survey of medical image registration. *Medical Image Analysis* **2**(1) (1998) 1–36
3. Pluim, J., Maintz, A., Viergever, M.: Mutual information based registration of medical imaging: a survey. *IEEE TMI* **20** (2003) 986–1004
4. Amores, J., Radeva, P. In: *Non-rigid Registration of Vessel Structures in IVUS Images*. Volume 2652. Springer-Verlag, Berlin Heidelberg (2003) 45–52
5. Rosales, M., Radeva, P., Rodriguez, O., Gil, D.: Suppression of ivus image rotation. a kinematic approach. In: *FIMH*. Volume 3504. (2005) 359–368
6. Hernandez, A., Radeva, P., Tovar, A., Gil, D.: Vessel structures alignment by spectral analysis of ivus sequences. In: *Proceedings of Computer Vision for Intravascular and Intracardiac Imaging (CVII)*, Copenhagen, Denmark (October 2006)
7. Danilouchkine, M.G., Mastik, F., van der Steen, A.F.W.: Interframe registration of IVUS images due to catheter rotation with feature-based optical flow. In: *Medical Imaging 2007: Ultrasonic Imaging and Signal Processing*. Edited by Emelianov, Stanislav Y.; McAleavey, Stephen A.. *Proceedings of the SPIE*, Volume 6513, pp. 65130V (2007). Volume 6513 of Presented at the Society of Photo-Optical Instrumentation Engineers (SPIE) Conference. (March 2007)
8. Loy, G., Zelinsky, A.: A fast radial symmetry transform for detecting points of interest. In: *ECCV '02: Proceedings of the 7th European Conference on Computer Vision-Part I*, London, UK, Springer-Verlag (2002) 358–368
9. Castro, E., Morandi, C.: Registration of translated and rotated images using finite fourier transforms. *IEEE Trans. on PAMI* **9** (1987)
10. Gil, D., Rodriguez-Leor, O., Radeva, P., Hernández, A. In: *Assessing Artery Motion Compensation in IVUS*. Volume 4673. Springer-Verlag, Berlin Heidelberg (2007) 213–220

Index

- Baseri, Babak, 53–62
Brockmann, Carolin, 120–127
Brodlie, K., 22–34
Brunner, G., 45–52, 112–119
Bulpitt, A.J., 22–34
- Carlier, Stéphane, 35–44
Chittajallu, D.R., 45–52, 112–119
Cloutier, Guy, 88–103
- Dam, Erik B., 63–70
Dandu, Naga P. K. R., 63–70
Danilouchkine, M.G., 6–13
Diehl, Steffen, 120–127
Downe, Richard W., 71–79
Duong, Luc, 80–87
- Fromageau, Jérémie, 88–95
- Ganz, Melanie, 63–70
Gatta, Carlo, 128–136
Gurmeric, Serhan, 35–44
- Hesser, Jürgen, 120–127
Horák, Jan, 71–79
- Jochum, Susanne, 120–127
Jou, Liang-Der, 14–21
- Kakadiaris, I.A., 45–52, 104–119
Katouzian, Amin, 53–62
Konofagou, Elisa E., 53–62
Kovárník, Tomáš, 71–79
Kurkure, U., 45–52, 112–119
- Laine, Andrew F., 53–62
Liao, Rui, 80–87
Lillemark Larsen, Lene, 63–70
Listz Maurice, Roch, 88–95
Lopez, John J., 71–79
- Maksimov, Dmitry, 120–127
Mastik, F., 6–13
Mauri Ferre, Josepa, 128–136
Mawad, Michel E., 14–21
Mendizabal-Ruiz, E. Gerardo, 104–111
Meunier, Jean, 96–103
Mohamed, Ashraf, 14–21
- Nielsen, Mads, 63–70
- Pujol, Oriol, 128–136
- Radeva, Petia, 128–136
Rodriguez Leor, Oriol, 128–136
Roy Cardinal, Marie-Hélène, 88–103
- Saijo, Yoshifumi, 88–95
Skalická, Hana, 71–79
Slabaugh, Greg, 35–44
Song, Y., 22–34
Sonka, Milan, 71–79
Soulez, Gilles, 96–103
Stutzmann, Tobias, 120–127
Sun, Yiyong, 80–87
- Tardif, Jean-Claude, 96–103
- Unal, Gozde, 35–44
- van der Steen, A.F.W., 6–13
- Wahle, Andreas, 71–79
- Xu, Chenyang, 14–21
- Yalamanchili, R.P., 45–52
Yang, Yan, 35–44
- Zheng, Lei, 120–127

The 2nd International Workshop on Computer Vision for Intravascular and Intracardiac Imaging

Technological advances in intravascular and intracardiac imaging offer increasingly useful information regarding vascular anatomy and function and are poised to have dramatic impact on the diagnosis, analysis, modeling, and treatment of vascular diseases. Computer vision techniques designed to analyze intravascular images for anatomic modeling, simulation, visualization, tissue classification, and the assessment of interventional procedures are therefore playing a role of increased clinical importance. This workshop presents the latest research in computational techniques for intravascular and intracardiac imaging. Topics of interest include atherosclerotic plaque image analysis and characterization, quantification of vascular morphology and function, tissue classification of intravascular images, computer-aided diagnosis of vascular disease, segmentation and anatomic modeling from IVUS, OCT, and so on, image-based biomechanical models of vascular anatomy and function, registration of intravascular and intracardiac images, image processing methods for intravascular/cardiac contrast agent applications, and percutaneous imaging/intervention.

<https://vpa.sabanciuniv.edu/sites/cvii2008/>

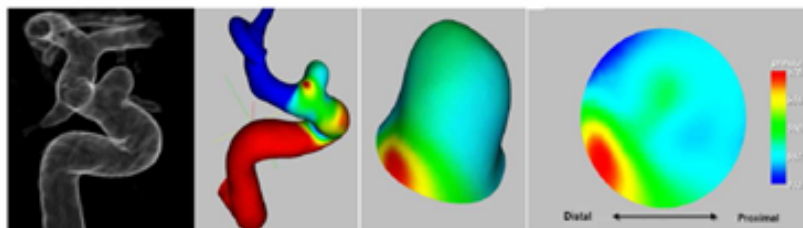
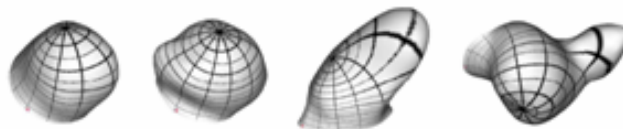
Sponsored by

SIEMENS

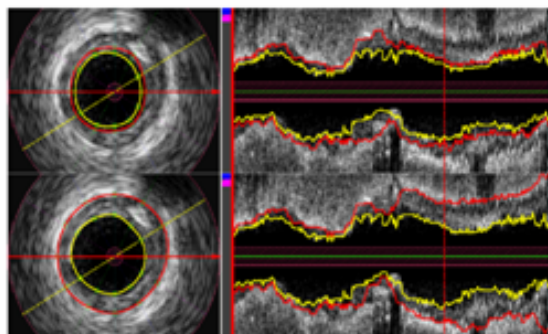
Credits



Brunner et al.: a heart centered coordinate system



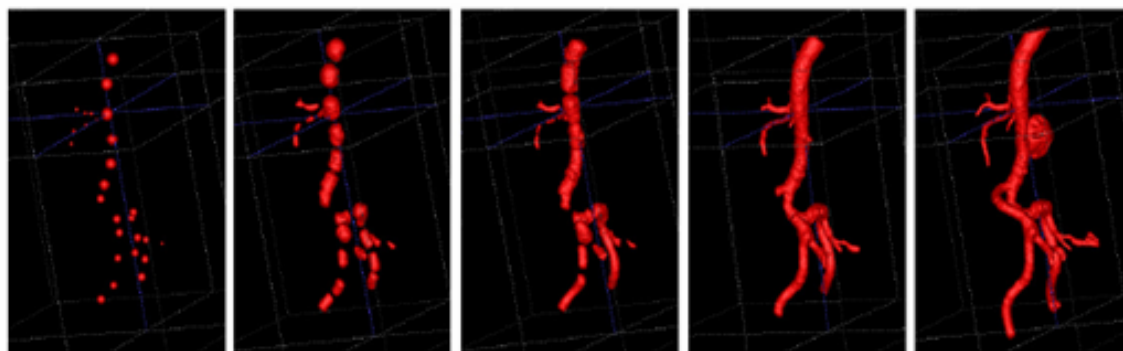
Mohammed et al.: volume rendered 3D DSA image of the artery and aneurysm; surface rendered image after CFD simulation showing wall pressure values; aneurysm surface with attached wall pressure after neck identification and mesh partitioning; wall pressure values mapped to the unit disc.



Downe et al.: Segmentation of IVUS images using graph search and a novel cost function



Liao et al.: Semi-automatic 2-D coronary artery segmentation and centerline extraction. First an original X-ray image, then multi-scale analysis and finally coherence enhanced multi-scale analysis



Song et al.: segmentation of the Aorta